Stochastic representation of material heterogeneity and its effects on flow: applications in soils of mixed wettabilities

Evan John Ricketts

School of Engineering

Cardiff University

Thesis submitted in candidature for the degree of Doctor of Philosophy

2023

Acknowledgments

The research presented in this thesis would not have been possible without the financial support of Cardiff University School of Engineering and LUSAS, and the contributions of Paul Lyons, this is gratefully acknowledged.

I would like to thank my supervisors Peter Cleall and Tony Jefferson. Your encouragement throughout these past few years has meant a lot to me, and is largely the reason I am where I am now. I'd particularly like to thank you both for supporting my excursions into other related research to satisfy my overly inquisitive mind, and the many opportunities you have given me. Similarly, I'd like to thank Pierre Kerfriden, not only for hosting me at the Centre des Matériaux de MINES Paris, but for your relentless enthusiasm in our work, at all hours.

I would also like to thank all of my friends and colleagues at Cardiff who have helped in more ways than I can count, and definitely in more ways than I realise. I'd particularly like to thank Bru for our ever interesting discussions, and for putting up with my incessant emails. They won't stop, so this is either thanks in advance or a warning depending on how you look at it.

Finally, I would like to thank my family and friends, my sister, my dad, and my mum. I would not be where I am today without your continual love and support, and I will forever be grateful for your indulgence in me and my ever changing obsessions and endeavours.

Published Papers

Journal Papers

Ricketts, E.J., Cleall, P.J., Jefferson, T., Kerfriden, P., Lyons, P. *Near-boundary error reduction with an optimized weighted Dirichlet–Neumann boundary condition for stochastic PDE-based Gaussian random field generators*. Engineering with Computers (2023). https://doi.org/10.1007/s00366-023-01819-6

Ricketts, E.J., Freeman, B.L., Cleall, P.J. Jefferson, A., Kerfriden, P. *A Statistical Finite Element Method Integrating a Plurigaussian Random Field Generator for Multi-scale Modelling of Solute Transport in Concrete*. Transport in Porous Media 148, 95–121 (2023). https://doi.org/10.1007/s11242-023-01930-8

Ricketts, E.J., Cleall, P.J., Jefferson, T., Kerfriden, P., Lyons, P. *Representation of three-dimensional unsaturated flow in heterogeneous soil through tractable Gaussian random fields*. Géotechnique, 1-34 (2023). https://doi.org/10.1680/jgeot.22.00316

Conference Papers

Ricketts, E.J., Cleall, P., Jefferson, A.D., Kerfriden, P., Lyons, P. *Modelling of unstable fingered flow in unsaturated soil with Gaussian random fields*. Proc. 10th European conference on numerical methods in geotechnical engineering (2023). https://doi.org/10.53243/NUMGE2023-304

Sayadi, S., Ricketts, E., Schlangen, E., Cleall, P., Mihai, I., Jefferson, A.. *Effect of microstructure heterogeneity shapes on constitutive behaviour of encapsulated self-healing cementitious materials*. MATEC Web Conf. 378 09004 (2023). https://doi.org/10.1051/matecconf/202337809004

Summary

This work presents an investigation into the modelling of the hydraulic behaviour of heterogeneous soils of mixed wettabilities. The model represents moisture transfer of a liquid phase, and can account for the highly non-uniform nature of unsaturated flow in soil due to the presence of strong heterogeneity. This is accounted for with Gaussian random fields to represent an arbitrary number of spatially varying material properties.

The theoretical formulations are presented to model this complex behaviour, as well as their numerical solutions which form the foundation of the developed model. The chosen method of random field generation is also investigated in terms of reducing the error in the correlated structures near the domain boundaries, as well as removing the need to solve over an extended domain. Methods to account for water repellency in soil are also given, such that the exaggerated flow behaviour it exhibits in relation to wettable unsaturated soil can be represented.

Validation of the model was conducted through representing field tracer experiments to assess the ability of the model to predict suitable vertical profiles of dye coverage. This was conducted for both wettable and water repellent soil, and quantified through confidence intervals such that a very low number of simulations was able to describe the overall model response to a high level of confidence.

The following conclusions can be drawn. The inclusion of material heterogeneity is crucial in representing complex unstable flow processes in soil of any wettability. The non-linear constitutive behaviour of the material that was predicted by the model simulations would be difficult to account for without spatial variability of material parameters. Similarly, the applied field generation method is a fast way to introduce this, and the proposed method of error reduction in the correlation structure is suitable for complex domains. The proposed methods to account for hydrophobicity based on the soil water retention curve are sufficient to allow unstable flow to develop. The similarity in finger characteristics of both the wettable and water repellent cases with the experimental observations suggest the model is more than sufficient in representing the complex flow behaviour that both can exhibit.

Contents

Nomenclature

$a(\cdot,\ \cdot)$	bilinear functional, see (3.31)
$b(\cdot,\ \cdot)$	bilinear functional, see (3.36)
A	saturation-capillary pressure relation parameter, Foroughi et al. (2022)
B	saturation-capillary pressure relation parameter, Foroughi et al. (2022)
$\mathrm{ACF}_{\mathbf{x}}$	Matérn autocorrelation function
C	saturation-capillary pressure relation parameter, Foroughi et al. (2022)
$C(h)$	covariance function
C_1	model parameter, see (7.2)
C_{ll}	coefficient of saturation derivative, see (3.13)
C_u	coefficient of uniformity
CI	confidence interval, see (6.5)
$\mathbf{C}$	mass matrix, see (4.9)
d	dimension
d_{10}	particle size for which 10% are finer
d_{60}	particle size for which 60% are finer
e	void ratio
E_{ss}	sink/source term
f_1, f_2	illustrative fields to be interpolated
f_I	interpolated field, see (7.4)
$\mathbf{F}$	flow vector in matrix governing equations, see (4.11)
h	lag distance
$H^1(\Omega)$	Sobolev space

$\mathbf{H}$	operator in (3.21)
J_l	right hand side of moisture transfer governing equations, see (3.15)
k	incremental variable
k_l	effective permeability
K_l	unsaturated hydraulic conductivity
K_{ll}	coefficient of pressure gradient, see (3.14)
K_r	relative coefficient of unsaturated hydraulic conductivity
K_ν	Bessel function of second kind of order ν
$\sum K_s$	total saturated conductivity of a considered collection of nodes
$\mathbf{K}$	stiffness matrix, see (4.10)
l	length-scale parameter
m_{vg}	van Genuchten parameter
$M_{i,j}$	mass matrix of discretised SPDE, indexed notation, see (3.33)
n	porosity
n_e	number of nodes per element
n_O	number of experimental observations (see Tale 7.1)
n_s	sample size
n_{vg}	van Genuchten parameter
$\mathbf{n}$	unit normal to the boundary
N	shape functions
$N(h)$	number of pairs of points in Ω of separation h
N	number of operations to denote algorithmic complexity
$\mathbf{N}$	shape functions
$N_{i,j}$	mass matrix integrated over the boundary, indexed notation, see (3.37)

q	scaled flux, see (6.1)
$\sum q$	total applied flux of a considered collection of nodes
s	suction
$S(\xi)$	spectral density, see (3.17)
S_l	degree of saturation of pore water
$S_{i,j}$	stiffness matrix of discretised SPDE, indexed notation, see (3.34)
SE	standard error
$\mathcal{S}(\mathbb{R}^d)$	space of rapidly decreasing smooth functions
$\mathbb{S}$	stochastic domain
t	current time-step
$\bar{t}$	t-score
t_1, t_2	upper and lower t-scores respectively
u_a	atmospheric pressure
u_l	liquid pressure
$\mathbf{u}$	location vector
$\mathbf{u_l}$	liquid pressure vector
$\delta\mathbf{u}_l$	incremental update of liquid pressure
$\boldsymbol{v_l}$	liquid velocity
$\widehat{\mathbf{v}}_l$	approximate liquid velocity normal to the boundary
x_{tmin}, x_{tmax}	maximum and minimum depths of the transition layer
$\bar{x}$	sample mean
$\bar{x}^P$	population mean
X_j	random variables
$\mathbf{X}$	Gaussian random field

W_i	right hand side of discretised SPDE, see (4.28)
$\mathbf{W}$	white noise on $\mathbb{R}^d$
z	elevation
$z(\mathbf{u})$	field value at $\mathbf{u}$
α	weighting parameter in Dirichlet-Neumann boundary condition
α_{vg}	van Genuchten parameter
$\gamma(h)$	semivariance
γ_l	unit weight of liquid
δ	distance for which correlations are near 0.1
$\epsilon(x)$	sigmoid function parameter, see (7.6)
Γ	Gamma function
ζ	domain boundary of Ω, i.e., $\partial\Omega$
ζ^e	element domain boundary
θ	volumetric water content
θ_l	volumetric liquid content
ϑ	sigmoid function, see (7.5)
λ	Robin coefficient
λ_1	weighted Dirichlet-Neumann coefficient, see (5.2)
λ_2	weighted Dirichlet-Neumann coefficient ,see (5.4)
μ_l	absolute viscosity of pore liquid
ν	smoothness parameter
ρ_l	liquid density
ϱ	constant in the right hand side of the SPDE, see (3.21)

σ	standard deviation
ψ_i	basis functions in $H^1(\Omega)$
ω	sigmoid smoothness parameter
Ω	problem domain in $\mathbb{R}^d$
Ω^e	element domain
Ω_{B}	near-boundary region
Ω_{EXT}	extended domain

Chapter 1

Introduction

Materials exhibit variability at different scales, where the heterogeneity that is present often plays a crucial role in influencing the response of the material due to external stimuli. Its presence can lead to exaggerated responses that may not occur if the material was homogeneous, making it difficult to understand and predict their behaviour under certain conditions. Such unpredictable behaviour can significantly affect the reliability and effectiveness of the material in its intended application. In engineering, environmental science, and even biomedical applications, understanding the variability within materials can be crucial. It determines the material's performance, durability, and interaction with surrounding media. Predicting outcomes without considering this variability can lead to significant errors or even catastrophic failures. As the complexity and intricacy of modern designs and applications grow, the need for accurate representation of material heterogeneity becomes even more pressing.

Porous materials encompass a wide range of materials critical to many sectors of industry and research. For example, soil exhibits strong levels of variability, and exemplifies the complexities that arise from material heterogeneity. Within a patch of soil, there can be vast differences in grain size, mineralogy, organic content, and wettability. Such diverse characteristics can have strong implications on its associated behaviour. Under homogeneous conditions, water might percolate uniformly, but real-world conditions often see the development of preferential paths or 'fingered flow'. This unstable flow response can be attributed to the presence of heterogeneity. It can also lead to an uneven moisture distribution, impacting plant growth, groundwater recharge, and even introduce such phenomena as subsurface erosion, posing risks to structures or ecosystems. Similarly, the distinct fingered-like pathways that arise can lead to regions of reduced cohesion, thereby reducing the strength of the surrounding soil. It is noted that this response becomes even more pronounced in soils of varied wettability, where the effects are typically exaggerated.

Traditional modelling approaches to capture this variable behaviour are deterministic and typically assume the simulated medium to be homogeneous. Whilst this

simplification makes the models tractable, they often fall short in capturing the true and varied responses that porous materials exhibit, especially when considering fluid flow dynamics. This difficulty becomes particularly pronounced in soils, where even minor flow irregularities due to heterogeneity can drastically alter the course of moisture, resulting in distinct infiltration patterns rather than a uniformly advancing wetting front. Recognising these limitations, the adoption of a probabilistic or stochastic approach becomes increasingly appealing. Such methodologies can still utilise simplified models but are better equipped to represent the intricate behaviour of heterogeneous materials. By embracing and incorporating randomness into the variability of the medium, stochastic models can generate a range of possible outcomes, enriching our understanding of the overall material response. Stochastic models, by their nature, resonate more with the inherent randomness found in real-world porous materials, providing a platform to address the very challenges posed by material heterogeneity and portray the intricate patterns of fluid flow within them.

The present work aims to develop and validate a stochastic numerical approach for modelling fluid flow in complex heterogeneous porous materials, utilizing soils - particularly those that exhibit fingered flow and mixed wettability- as a key application to elucidate the inherent challenges and intricacies of representing material heterogeneity. While soil serves as the principal application in this research, the challenges and concepts discussed hold relevance across many domains. Be it the medical field where porous bone structures impact drug delivery, or the realm of civil engineering where concrete porosity affects structural integrity, understanding and modelling heterogeneity is universally critical.

Initially, the model and its discretisation are presented for moisture flow, based on the conservation of mass and Darcian flow. Similarly, the governing equation is derived for a method of random field generation based on stochastic partial differential equations (SPDE). Random fields are a well-established choice for introducing soil heterogeneity, and their use will be detailed in the following chapters. Due to the complexity of the governing equations, numerical methods are necessary for their solution, and the finite element method is employed for their spatial discretisation. The presented model solves the equations in three dimensions, and accounts for both Dirichlet and Neumann boundary conditions. A novel method for applying Neumann boundary conditions is also presented based on spatial variation

in the saturated conductivity at the applied boundary. Details are also given on the constitutive components of the model that allow hydrophobicity of the soil to be represented. This is mainly done through a soil water retention curve that can account for the unique water entry pressures that are characteristic of water repellent soils. Similarly, the method of representing layered soils of mixed wettabilities is given, as well as a novel approach to deal with the transition region between the layers, based on an assumed level of mixing.

Validation of the developed model is a crucial step in providing confidence in the approach. This is done for both the unsaturated case, and the case where strong water repellency is present. Field tracer experiments are replicated to assess the ability of the model to represent the observed fingered flow characteristics, and the numerical results are quantified in terms of confidence limits.

1.1 Study objectives

The objectives of this study are as follows:

i. Develop a stochastic numerical approach for flow related problems to account for heterogeneity in porous materials
ii. Investigate the practicalities of implementing random fields to represent material heterogeneity and its associated challenges
iii. Develop a numerical approach to simulate fingered flow behaviour in soils, including water repellent materials
iv. Validate the model and quantify its ability to simulate preferential fingered flow in soil of mixed wettability

1.2 Scope and limitations

Mechanical processes, such as erosion in water repellent soils, are particularly relevant but have not been considered in the presented work. Such processes can lead to localised deformation or failure in extreme cases. Similarly, complex boundary conditions that can account for runoff are not developed. Here, the applied boundary condition is assumed to infiltrate fully into the soil surface, where in reality, water repellent soils can exhibit ponding and high rates of runoff. The developed model does not couple different complex phenomena, only representing the flow of a single moisture phase. Whilst the theory for coupled models is well developed, the focus was put on representing material heterogeneity and water repellent behaviour,

which is largely explored in relation to moisture transport. Finally, hysteresis is not considered, which is a predominant mechanism in drying and wetting, as well as the persistence of hydrophobicity.

1.3 Thesis overview

A brief overview of each chapter is given below.

In Chapter 2, a review of areas related to the modelling of water repellent soils is presented. Whilst the majority of the section is dedicated to reviewing techniques used in representing complex flow phenomena in water repellent soils, also explored are the effects of heterogeneity on soil hydraulic response, techniques for modelling flow in unsaturated soils, stochastic methods for soil modelling, random field generation methods, and an overview of soil hydrophobicity. The aim is to give a well-rounded overview of topics relating to the modelling of water repellent soils, in order to contextualise the chapters that follow.

Chapter 3 describes the theoretical formulation of the developed model. First, moisture transfer is considered, and the governing equations of flow are derived. Similarly, the generation of random fields through the SPDE method is described. These form the basis of the work described in subsequent chapters. The numerical solution of the given theoretical formulations is presented in Chapter 4. In both the moisture transfer and field generation, spatial discretisation is achieved through the finite element method, where a finite difference method is used for the time discretisation. Once more, these methods are used in the chapters that follow and form the foundations of the model.

Chapter 5 presents an investigation in error reduction in the near-boundary when generating random fields through the SPDE approach. Current mitigation strategies are presented, which are dependent on the applied boundary condition. Following this, a new boundary condition is suggested which is shown systematically to be more suitable in reducing the spurious values seen near the boundary of the generated fields. This is shown for simple and more complex domains.

In Chapter 6, the model is applied to simulate a field tracer experiment to validate the model. The application of the random fields is described in detail, as well as a novel approach for applying surface boundary conditions such that material heterogeneity

is accounted for. Finally, the uncertainty in the presented results is quantified with a confidence interval-based approach.

Chapter 7 presents the development of the model to account for soil of varying wettability, specifically hydrophobic soil. The additional numerical components are presented, such as the updated constitutive components and the layering of soil, as well as the transition region between soil layers that required careful consideration. The model is then applied to represent a different field tracer experiment to that considered in Chapter 6, where hydrophobicity is present in the soil mass. Similar quantification of the presented results is conducted, such that the characteristics of dye coverage can be used to show convergence in the model results.

Finally, Chapter 8 presents the conclusions from the study, and makes suggestions for the wider applicability of the developed model and how it can be extended.

Chapter 2

Literature review

2.1 Introduction

In the following chapter, the literature is reviewed considering subjects relating to the modelling of flow behaviour in unsaturated soil, as well as water repellent soils. As this study is largely concerned with the development of a model to represent soils of mixed wettability, the majority of this chapter will focus on previous works in modelling hydrophobic soil behaviour in relation to infiltration processes. The other sections act as building blocks to give context of the wider research relating to modelling flow behaviour in soil.

Section 2.2 considers the effects of heterogeneity on the hydraulic behaviour of soil; Section 2.3 provides an overview of soil hydrophobicity; Section 2.4 presents a review on modelling approaches to represent flow phenomena in unsaturated soil; Section 2.5 reviews the current literature on the stochastic modelling of soils; Section 2.6 presents a review on random field generation methods; Section 2.7 provides a review of the literature relating to flow processes of water repellent soil; and Section 2.8 concludes on the findings.

2.2 Effects of heterogeneity on hydraulic behaviour of soil

The key aspects relating to heterogeneous soil and its effects on flow behaviour are summarised here. Further details of methods to deal with soil heterogeneity in geotechnical engineering applications, as well as the implications of soil heterogeneity are discussed in Elkateb et al. (2003).

Heterogeneity is a known cause of unstable flow in unsaturated and hydrophobic soils, resulting in fingered flow patterns (Ritsema et al. 1998; Sililo and Tellam 2000; Sheng et al. 2014). The preferential flow paths, which form in the soil mass, transport water at an accelerated rate and can lead to increased rates of solute transport (Gjettermann et al. 1997; Reichenberger et al. 2002; Morris and Mooney 2004; Perkins et al. 2011), as well as localised erosion. The effect of using heterogeneous hydraulic parameters in numerical analyses on various aspects of soil behaviour has been investigated systematically over the past 20 years (Jiang et al. 2022). Their

effects have been studied in relation to water uptake by plant roots and the influence of non-uniform unsaturated flow (Kuhlmann et al. 2012). Zhu and Mohanty (2002) explored steady-state evaporation and infiltration using the well-known van Genuchten model (van Genuchten 1980). They investigated a number of averaging schemes, applied to van Genuchten parameters, and compared the results to measured effective parameters at field scale. Other researchers (Hammel et al. 1999) studied solute transport using spatially and temporally varying pore-water velocity fields at different spatial scales. The issue of transient flow in large-scale spatially variable soils was explored by averaging local governing flow equations in three-dimensional representations of local soil properties (Mantoglou and Gelhar 1989). The importance of hysteresis in numerical modelling of water flow, related to heterogeneous distributions of hydraulic conductivities, was studied by Nakagawa et al. (2012). An underlying assumption in these studies is that the inclusion of spatially varying parameters in numerical models, especially local variations in hydraulic properties, is necessary to achieve physically representative simulations. If the effects of heterogeneity in analyses are neglected, the predicted uniform wetting front will be, in general, inconsistent with experimental observations (Glass et al. 1989; Siemens et al. 2021).

2.3 Overview of soil hydrophobicity

Water repellency in soils is known to be generated by five dominant methods: fungal and microbial activity, growth of particular vegetation species, organic matter, heating of the soils by wildfires, and soil characteristics (Doerr et al. 2000). The fluctuation in levels of water repellency following a wildfire event can lead to significant changes in the hydrological response of the soil (Granged et al. 2011; Nyman et al. 2014; Chen et al. 2020), whether it be upon the surface such as enhancing runoff and erosion, or within the soil mass through the increased likelihood of unsteady infiltration. These body processes are where much of the modelling of hydrophobic soils is concerned, with relative sparsity of work surrounding the response on the surface.

Due to soil being highly variable, the exact cause of changing levels of water repellency is often unclear and can be best considered as an accumulation of various influencing factors. During a fire, super-heating of the soil occurs, leading to organic matter vaporising and moving downwards through the soil body. Lower temperatures at depth result in the vapour cooling and condensing on the fabric of

the soil, coating particles in the cooled organic substance (DeBano 2000b). Similarly, aliphatic hydrocarbons are released from organic matter when subject to extreme heat, generating hydrophobic compounds (Malkinson and Wittenberg 2011). Temperatures between 175°C and 280°C are necessary to cause an increase in hydrophobicity, whereas going beyond this range will revert the change in wettability (DeBano 2000b; Doerr et al. 2004), leading to the non-uniform spread of water repellency close to the surface often seen following a wildfire event (DeBano 2000b; Mataix-Solera and Doerr 2004; Chen et al. 2020). Whilst high levels of water repellency are seen initially, these do breakdown overtime due to the system being unstable. As Figure 2.1 suggests however, given a longer timescale, these levels do begin to rise, and this is thought to be due to organic matter recovery.

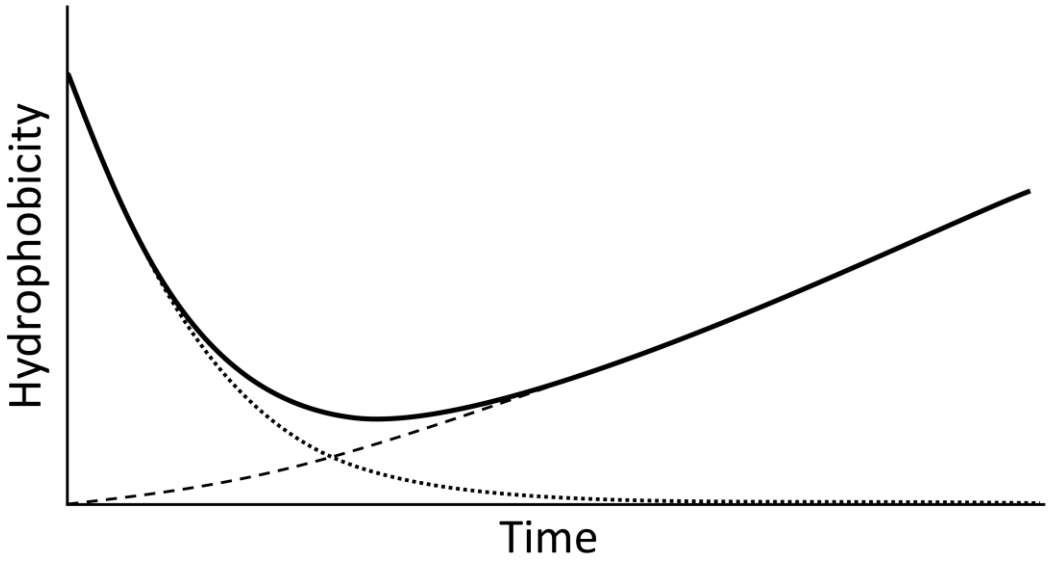

Figure 2.1: Hypothesised long-term changes of soil water repellency. Solid line: overall response, dotted line: short-term generated from fire, dashed line: long-term induced by increased biotic activity (reproduced from Malkinson & Wittenberg (2011)*)*

Increased biotic activity due to vegetation and microfauna populations, microbial, bacterial and fungal, can all lead to increased levels of water repellency (Wallach et al. 2005; Hallett 2008; Malkinson and Wittenberg 2011). Similarly, certain species of plant can induce stronger hydrophobicity in soils beneath them, such as evergreens and differing eucalyptus species (Doerr et al. 2000; Malkinson and Wittenberg 2011). Contrary to this, as stressed or killed trees drop foliage whilst ash settles on the surface, a wettable layer will form, and can reduce the effects of heating of the soil leading to reduced water repellency and less risk of surface runoff and erosion

(Cerdà 1998; Pannkuk and Robichaud 2003; Shakesby and Doerr 2006; Bodí et al. 2012). This deposited layer will eventually clear, highlighting its importance in the short-term analysis post-fire on water repellency levels (Cerdà and Doerr 2008). This process could be the cause of reduced levels of hydrophobicity being found when trying to replicate wild fire induced changes (Coelho et al. 2004; Ferreira et al. 2005), as replicating all contributing factors is challenging. As the ash cover deteriorates, the topsoil will be left with no vegetation, and has been seen to be the primary cause of increased run off and erosion rates (Prosser and Williams 1998; Johansen et al. 2001; Wohlgemuth et al. 2001). Similarly, as the short-term water repellency grows at the surface, the coatings upon the minerals will impede the formation of a soil crust, suggesting increased risk of splash erosion (Terry and Shakesby 1993). Rill erosion is also observed, due to the water repellent (WR) layer causing a build-up of pore water pressure and consequent reduction in shear strength in the overlying saturated soil (DeBano 2000a). Fingered flow can also result from this, as the distinct paths caused by rill erosion will offer less resistance to infiltration.

With increasing levels of hydrophobicity, the chances of preferential flow and fingering are greatly increased, often arising from changes in wettability (Bauters et al. 1998; Ritsema and Dekker 2000). Having many influencing factors means that modelling such processes due to increased variability is challenging; a single characteristic or parameter will not suffice (McKissock et al. 1998). With the risk of extreme weather events increasing, potentially leading to wildfire induced water repellency, the need to model and predict the behaviour of soil transport processes is ever more necessary.

2.4 Modelling of flow in unsaturated soil

Flow processes in unsaturated soil can exhibit signs of both stable and unstable behaviour, depending on the material being investigated. As will be seen in the later sections and chapters, the representation of unstable preferential flow requires careful numerical consideration. One approach is the use of a simple active region model (ARM) to allow for fractal flow in a continuum domain (Liu et al. 2005). The approach employs regions in the numerical domain that are either active or inactive, where flow is either mobile or immobile respectively. It is based on the assumption that preferential flow follows a fractal pattern, and showed consistent results between field observations and the model. Liu et al. (2005) suggested further evaluation of the

model to assess its capabilities. This has been further investigated in more recent years; for example Sheng et al. (2011) applied the approach to preferential flow and solute transport. The ARM approach was compared with the inherently similar mobile-immobile region model (MIM), and was used to analyse dye infiltration experiments and quantify soil water content and Cl^- concentration. The movement of soil water and solute was assumed in the vertical direction only, with averaged horizontal behaviour. Once more, the ARM approach was seen to give adequate results, especially when compared with the MIM. The main difficulty in the method is the estimation of the ARM parameter, a constant between 0 and 1 which increases with flow heterogeneity (Liu et al. 2005). To address this further, Sheng et al. (2012) developed three determination methods of the parameter based on distributions of soil water content and dye stained regions. Further experimental studies have also been carried out to determine the capabilities of the ARM approach (Sheng et al. 2014).

Lower dimensional modelling is also an area of interest due to its ability to approximate highly complex behaviour with low computational demands. Often the well-known Richards equation is employed in this setting (Richards 1931), as was the case in Zha et al. (2013). The general 1-D Richards equation was modified with a correction term expressed in terms of soil water content, being tested in gradational and layered soils. Several numerical algorithms were also posed for calculating the water content based on Darcian flux in layered soils. The water content based formulation was seen to perform better for initially dry soils than the usual mixed formulation of the Richards equation, whilst also performing well over coarse meshes. The authors highlighted that the model was restricted to unsaturated flow, and should be extended to account for both saturated and unsaturated flow. See Gandolfi et al. (2006) for a comparison of other 1-D models for flow in unsaturated soils. The Richards equation can also be extended to two and three dimensions, as was done in Cavalcante et al. (2019). The equation was extended to 3-D for unsaturated flow, illustrating flow behaviour under two conditions: (i) a domain with an initial higher volumetric water content in a given region, and (ii) a domain with a region of decreased volumetric water content to represent localised drying. For the first case, the water was seen to flow under unsaturated conditions to regions of lower water content, where the opposite was observed in case two. Highlighted was

the impact of the advective and diffusive components of the Richards equation when considering transient unsaturated flow.

Slope stability, as is shown in the next section, is a large area of research in soil modelling due to its associated risk in design and failure. Zhang et al. (2009) considered unsteady seepage of water and air in soil slopes due to under water level rise. The two-phase model was used to investigate the influence of capillary pressure on slope safety coefficients, finding that the safety of a slope is mostly sensitive to negative pore water pressure, where the air phase could be neglected. This is in contrast to Cho (2016), suggesting that the inclusion of the air-phase was dependent of the soil type being considered. The authors studied the interaction of air and water two-phase flow due to heavy rainfall, and their effects on slope stability of unsaturated soil. When under heavy rainfall, the pore air pressure was seen to increase, delaying the effects of water flow. This was more prominent in silty soils, showing deeper critical failure surfaces, where the inclusion of the air phase in sand was seen to given negligible effects. Coupled models have also been used to asses slope behaviour. Hu et al. (2016) coupled elastoplastic deformation with two-phase fluid flow for homogenised slope stability induced by rainfall. The model, based on their derived constitutive model, was validated with lab tests associated with isotropic loading and shearing, as well as the Liakopoulos drainage test. Numerical testing assessed the suitability of the constitutive model, and correlations with experimental data were found. Similarly, neglecting gas flow was seen to give overestimations in rainfall induced deformation. For a more exhaustive review on coupled heat and water models for transport in unsaturated soils, see Lekshmi and Arnepalli (2017).

2.5 Stochastic modelling of soil

As highlighted in Section 2.2, the inclusion of spatially varying material parameters is necessary in numerical models to achieve physically representative simulations. Although it is possible to generate a random distribution and assign this to a model parameter, this will not give an accurate representation of soil material properties because soil bodies have correlated micro-structures with intrinsic length scales (Lloret-Cabot et al. 2014). Various methods have been proposed in the literature for representing spatial variability within a soil body, with random fields being a well-established choice (Arregui-Mena et al. 2016). These fields are commonly defined by

the statistical properties of the variable that the field describes, such as the mean, standard deviation, and correlation structure.

The seminal work of Vanmarcke (1977) introduced random field theory as a means of representing the spatial variability of soil properties in geotechnical systems. Rubin & Or (1993) used random fields to represent saturated conductivity, the rate of change of hydraulic conductivity with suction, and characteristic root depth, investigating the effects of the spatially varying parameters on root water uptake. The numerical domain was split using parallel columns, and used to compute the expected value and second moments of the degree of saturation and pressure head through averaging over the domain. The water uptake by plants was seen to have a profound effect on the dependent variables, and the spatial moments compared well with traditional Monte Carlo simulations. A similar use of random permeability fields was conducted by Li et al. (2009), where a Karhunen-Loeve (KL) expansion based probabilistic collocation method (PCM) was developed to predict flow in the vadose zone. The PCM computes solutions at a set of collocation points, and was shown to capture the stochastic behaviour of the effective saturation and pressure fields with many fewer simulations than traditional Monte Carlo simulations. KL expansion-based fields have also been shown to be suitable in representing random permeability fields for single and multiphase flow models of heterogeneous porous media (Li & Zhang, 2007, 2009). An alternative approach is embedding equivalent random variables based on random field characteristics into the governing equations of the model (Mousavi Nezhad et al. 2011). The authors used a perturbation-spectral approach to include random material fluctuations into the Richards equation to simulate water flow in unsaturated soils. The model was shown to give better agreement with lysimeter testing results over a deterministic model, highlighting the importance of stochastic methods. More recently, a reduced order model for 1-D unsaturated flow in heterogeneous soil was developed, considering spatially varying hydraulic conductivities (Liu & Welfert, 2020). The model was also based on the Richards equation, and compared the results of direct numerical simulations, a homogenized model, and the proposed reduced order model, which consisted of a coupled system of moment equations for water content and soil hydraulic parameters. A single solution was needed to obtain the stochastic characteristics of

unsaturated flow, vastly reducing overall simulation times, and was shown not to underestimate the downward numerical flux as in the other considered approaches.

A number of investigators have also adopted random fields for simulating slope stability and related problems (Srivastava et al. 2010; Cho 2012; Li et al. 2015; Jiang et al. 2018). These studies showed that neglecting these spatial variations can lead to significant underestimates of slope failure probabilities (Le et al. 2012; Huang et al. 2017). This is because homogenous models do not account for localised water accumulation and the associated reductions in effective stress and shear strength. Much of the reported research involving spatially varying materials has been based on two-dimensional (2-D) simulations. This use of 2-D analysis, rather than 3-D, may be attributed to the relatively high computational demands of the latter (Ou-Yang et al. 2021). In more recent years, there has been an increase in 3-D random field simulations. Hicks et al. (2014) explored how the heterogeneity of undrained shear strength impacts the reliability and risk posed by a long slope cut in clay using a 3-D finite element program. The model allowed the identification of three possible failure modes that are significantly influenced by the scale of fluctuation relative to slope geometry. A similar investigation has been carried out to assess whether 3-D analyses are necessary for long slopes consisting of spatial random soils (Liu et al. 2018). Using a random finite element model, the authors concluded that 2-D plane strain analyses, based on the most pessimistic cross-section, generally give a more conservative result than the corresponding full 3-D analysis. Ng et al. (2022) investigated how spatial variability of saturated water permeability affects the stability of unsaturated soil slopes using 3-D random fields under rainfall conditions. Chi et al. (2022) investigated the effect of spatial variations in the soil properties of the Guanyinyan composite dam on the degree of settlement and the development of cracks. In their work, random fields were coupled with a 3-D FE analysis. They concluded that the consideration of spatial variability leads to a more accurate dam safety evaluation relative to traditional security indexes that ignore spatial variability. Conditional random fields have also been explored, where the field parameters are based on direct samples of measured data (Li et al. 2016). Whilst, in certain cases, 2-D analyses can lead to more conservative predictions, it is generally considered more accurate to simulate real systems with 3-D models, particularly when the nature of a problem is inherently three dimensional (Hungr 1987; Liu et al. 2018; Ng

et al. 2022). Relatively little work has been undertaken on using random fields to explicitly represent fingered unstable flow. A few notable exceptions to this include the work of Chen et al. (2000), who used Gómez-Hernández and Cassiraga's (1994) random field generation code GCOSIM3D to represent the distribution of saturated conductivities in a soil mass. More recently, Cueto-Felgueroso et al. (2020) employed Gelhar and Axness's (1983) stochastic algorithm to generate intrinsic permeability fields. Their work studied the relationship between fingering instabilities and heterogeneity, and quantified the influence of the degree of heterogeneity on the resulting infiltration pattern. This gap in the literature is further addressed by the work of this thesis. The modelling of unstable fingered flow due to the presence of a heterogeneous medium is given in Chapter 6. Similarly, the effects of heterogeneity on fingered flow in water repellent soil are seen in Chapter 7, a case for which the instability of flow is much more pronounced.

2.6 Random field generation

Uncertainty in physical systems, such as those seen above, can be introduced with random fields. This is a well-established practise in soil modelling, but can be applied much more widely to represent other complex phenomena. Existing methods of generating correlated random fields include Karhunen-Loève's expansion (Huang et al. 2017; Montoya-Noguera et al. 2019), local averaging subdivision methods (Fenton and Vanmarcke 1990), covariance matrix decomposition (Olsson and Sandberg 2002; Cheng et al. 2018; Jiang et al. 2018; Tang et al. 2020) and the solution of stochastic partial differential equations (PDEs) derived from Whittle-Matérn's autocorrelation function (ACF) (Lindgren et al. 2011; Roininen et al. 2014).

The latter of these methods is computationally efficient due to sparse matrix linear algebra, and is well suited to existing FEM codes due to the construction of the PDE components and their solution. Another key aspect is the strong theoretical basis in the desired domain properties of the fields that can be produced, being due to the clear distinction between the construction of the theoretical model and the numerical methods used in the solution process (Lindgren et al. 2022). This ensures that the correlated structure of the generated fields is as intended. The approach also allows for many generalisations of stationary Matérn fields such as non-stationary fields and those generated over less idealised domains (Lindgren et al. 2011; Fuglstad et al. 2015; Bolin and Kirchner 2020). For practical simulations, the domain must be

reduced to a bounded domain of interest, requiring boundary conditions that are not generally known (Khristenko et al. 2019). By applying a non-exact condition at the boundary, the approximation of the ACF that the stochastic PDE represents will breakdown, resulting in spurious values in the near-boundary region. Often, the homogenous Neumann or homogeneous Dirichlet condition is chosen due to the ease of implementation. To deal will this, the computational domain Ω is often extended, such that solving the stochastic PDE over the extended domain and extracting Ω will result in minimal effects from the applied the boundary condition. The reduction in error at the boundary is relative to the size of extension, and has been previously studied (Khristenko et al. 2019).

An alternative approach is to apply the Robin boundary condition through careful choice of the Robin coefficient λ, which can be thought of as a tuning parameter. The choice of λ can be problem dependent, but a choice of $\lambda = 1.42l$, where l is defined as the length-scale parameter, has been found to be an adequate approximation (Roininen et al. 2014). As such, the use of an extended computational domain is not strictly necessary when applying this condition. The computational expense of the method, considered here via the order (O) of the number of operations (Mala and Ali 2022), is dependent on the numerical method implemented to solve the PDE. These methods can have very low computational expense such as $O(\mathrm{N}\log\mathrm{N})$ (Lang and Potthoff 2011), and are significantly more efficient than other field generation methods such as LAS ($O(\mathrm{N})$) and CMD ($O(\mathrm{N}^3)$) (see Liu et al. (2019) for a summary of other common methods and their computational complexity). This is also true for alternative methods such as stepwise CMD, which is $O\left(\mathrm{N}_\mathrm{x}^3 + \mathrm{N}_\mathrm{y}^3 + \mathrm{N}_\mathrm{z}^3\right)$ (Li et al. 2019). In addition, the variation in efficiency is non-linear, with the degree of non-linearity becoming more pronounced with larger values of N. The method's ease of implementation in an existing FEM framework allows for efficient random field generation for domains where pre-existing methods would be intractable.

It is worth noting that this choice of $\lambda = 1.42l$ was not established in a rigorous way, as it was deemed out of the scope of the study (Roininen et al. 2014), and it was suggested that λ should vary as a function of the boundary. This was later considered by Daon and Stadler (2018), who utilised a spatially varying Robin coefficient to provide domain Green's functions that are close to the free-space

Green's functions of the Matérn covariance function. Through numerical experiments, the approach was seen to reduce the observed boundary effects, but the computation of the spatially dependent coefficient posed difficulties due to integral singularities and a required prior knowledge of pointwise variance over the domain which may not always be available. Other approaches have been taken, such as the use of a partial Dirichlet-to-Neumann operator on the extended boundary (Calvetti et al. 2015a). The mapping depends on the unknown correlation structure of the extended domain, and as such is an unknown itself that needs to be estimated. It was later shown to have suitable representation by a lower dimensional truncated Karhunen-Loève expansion based on information about the desired correlation structure (Calvetti et al. 2015b). The mapping was seen to result in reductions in computational complexity and matched well with simulated and real data. The reduction of error in the near-boundary is an open problem, and one which is addressed systematically in Chapter 5.

2.7 Modelling water repellent soils

In the following, modelling approaches are considered that look at representing the overall movement of water through the soil mass, termed here as body processes, and the influence that water repellency has upon them. This movement can be described in various ways, such as through capillaries of varied geometry (Czachor et al. 2010; Takeuchi et al. 2017; Wang and Wallach 2020), or by pore-scale analysis (Ustohal et al., 1998; Blunt et al., 2002; Raoof and Hassanizadeh, 2012). Similarly, a more distinct response can be seen by the presence of preferential and fingered flow in the soil mass. These are synonymous with hydrophobicity, and vary in response as the level of wettability changes. In cases where preferential flow occurs near the soil surface, accelerated rates of rill erosion can cause problems for stability, intensifying the specific flow paths the water takes. This also increases the rate at which solutes are transported, and could increase risk of pollution in areas of heavily treated soils such as agricultural land. The ability to simulate the movement of wetting fronts through the soil mass can provide vital insight, being able to assist with engineering problems such as agricultural design.

2.7.1 Capillary flow and infiltration

Early work on modelling infiltration within water repellent soil was presented by Yang et al. (1996) who used capillary pressure as a driving force to describe the

movement of water in furrow-sown water repellent sand. At the time, very few models existed for soil water repellency, especially those with an agricultural application. The aim was to optimise the design of the furrow to increase water conservation, taking into account evaporative resistance and soil surface conditions. Water repellency was included through appropriate hydraulic characteristics to the finite element method, showing that an initially dry furrow composed of water repellent sand had reduced rates of evaporation compared with wettable sand following infiltration. Whilst the finite element method is a widely adopted approach, alternative methods such as the use of machine learning and neural networks have also been employed in representing complex hydrodynamic behaviour. Xiong et al. (2011) evaluated the ability of such models in simulating the flow of water in soil of varied wettability, looking to predict the spatial development of plumes. Experimental and synthetic numerical data were used as the network's basis, with the main objective being the utilisation of the data to create self-organising maps (SOM) which could inform modular neural networks on how to simulate soil water dynamics. The 1-D SOM was able to represent the moisture content distribution in the transition zone of the wetting plumes, whilst also preserving the spatial structure of the soil moisture distribution. It is common to use experimentally gained soil characteristics to influence a model's development; however, evaluation of soil properties can be conducted through numerical analysis to reduce development time. Takeuchi et al. (2014) attempted to address this shortcoming, formulating a physically-based model to represent the hydrodynamic properties of porous media of mixed wettability. The model was validated against experimental results, preforming reasonably well, and finding that the number of grains considered was highly influential in infiltration due its relationship with the contact angle in the cell.

Plume dynamics have been further analysed through moment analysis; Xiong et al. (2012) successfully characterised plumes during wetting and redistribution for 2-D transient flow experiments in a transparent flow chamber. The spatial moments for a 2-D moisture plume have been previously defined as (Yeh et al., 2005; Lazarovitch et al., 2007)

$$M_{ij}(t) = \iint_{-\infty}^{+\infty} \theta_{\mathrm{diff}}(x,z,t) x^i z^j \mathrm{d}x\mathrm{d}z \quad (3)$$

where $\theta_{\mathrm{diff}}(x,z,t) = \theta(x,z,t) - \theta_{\mathrm{init}}(x,z,0)$ is the spatial distribution of water content increase with time, $\theta(x,z,t)$ and $\theta_{\mathrm{init}}(x,z,0)$ are spatial measures and initial soil moisture contents respectively, and both i and j are non-negative integers related to the directions x and z. The fitted model accounted for capillary and gravitational forces for porous media with dynamic wettability. Unlike the somewhat restricted representation provided by neural networks, it was observed that water repellency had significant impact on the patterns exhibited by water flow. The empirically developed model was validated, and enabled the authors to predict the plume shape geometry beyond periods for which measurements were taken. The moving-boundary approach -coupled with a finite element solution of the Richard's equation- has also been implemented to represent spatial changes in plume geometry. Brindt and Wallach, (2017) had previously used this approach for the modelling of stable and unstable flow, and later extended this for 2-D gravity-driven unstable flow for soil of varied wettability (Brindt and Wallach 2020). Similarly to Ganz et al. (2014) and Xiong et al. (2012), the plume perimeter was included in the model, allowing for relationships between the geometry of the plume and soil moisture content properties to be made. It was seen that the model was capable of accurately simulating unsaturated flow problems, whilst also being able to predict 2-D and 3-D preferential flow.

A similar approach in representing plume geometry used the well-known HYDRUS software, with the aim of validating the use of electrical resistivity tomography (ERT) in analysing wetting plume geometry (Ganz et al. 2014). The model included hysteretic effects, resulting in slowed wetting front arrival times, and matched well with experimentally gained dye patterns. In later years, a thorough assessment of the software was conducted by Wang et al. (2018), evaluating cumulative infiltration, wetting front and the volumetric water content for both vertical infiltration and horizontal imbibition for soils of varied wettability. An assessment into the capability of the software was necessary as an explanation for inaccuracies, such as those seen in Ganz et al. (2014), needed further exploration. The software was seen to accurately calibrate and validate said key hydraulic parameters, and was able to reproduce the previously mentioned hydraulic processes. The authors (Wang et al. 2018) however found that as the level of water repellency increased, the accuracy of

the model decreased, indicating that the model may not be so well suited when water repellency is a key attribute.

Levels of cumulative infiltration have also been used in evaluating the ability of certain functional models when hydrophobicity is present. Zhao et al. (2020) reported one dimensional infiltration experiments for wettable and hydrophobic soils. The aim was to evaluate the Kostiakov function, Gamma function and Beta function at replicating rates of infiltration over time. It was seen that having greater values of initial soil water content results in an earlier inflection point for increasing cumulative infiltration, and subsequently larger values of infiltration rate at the inflection point. All models considered were able to represent the dynamics of water repellent soils, with the Beta function showing the highest level of accuracy. A similar simplistic model based on physical principles was presented by Brown et al. (2018), predicting the soil water dynamics of structured soils for various wettabilities. Three soils were analysed, all having distinct soil textures, to show how preferential flow and hydrophobicity affect the soil water dynamics associated with infiltration. The model depicted the effects of water repellency accurately, ultimately showing that with a more repellent soil, the top layer of the structured soil remained at a lower soil-water content for longer. Both Brown et al. (2018) and Zhao et al. (2020) illustrated the strength of utilising simple functional models when representing well understood processes. An area where this simplistic approach may not be suitable is when the mechanical behaviour of the soil is under consideration. The discrete element method (DEM) and volume of fluid (VOF) have been used in combination by Davydzenka et al. (2020) to investigate the effects of wettability on deformation of the soil body. DEM-VOF combines DEM and computational fluid dynamics, with VOF being capable of dealing with dynamics at the pore-scale. Suitable boundary conditions allow for the contact angle to be accounted for, with the effects of wettability on deformation being seen through a series of examples. The patterns of fluid displacement observed shows that when wettability reaches high values, invasion of water is more prominent. The capabilities of the DEM-VOF couple are realised for the simulation of mechanistic problems, an area which is under explored in relation to water repellent soils.

There is a relatively limited amount of work reported considering the specific problem of modelling of capillary effects in relation to wettability; capillary bundle models are

often used, requiring simplifying assumptions to allow upscaling to bench and field scale domains (Mualem, 1976; Letey et al., 2000; Vervoort and Cattle, 2003). Modelling of soil pore-water contact angle for capillaries with non-cylindrical pores has been conducted, with the effects of changes in contact angle on water retention analysed by Czachor et al. (2010). A theoretical model was produced, illustrating that by inducing small changes in the wetting angle, the behaviour of a soil can switch between wettable and water repellent. The verified theoretical model demonstrated that water retention is sensitive to changes in the wetting angle for the wetting curve, but has little to no influence over the drying curve. Takeuchi et al. (2017) investigated triangular cross-sectional capillaries (see Figure 2.2) analysing how geometric changes affect the permeability of the system.

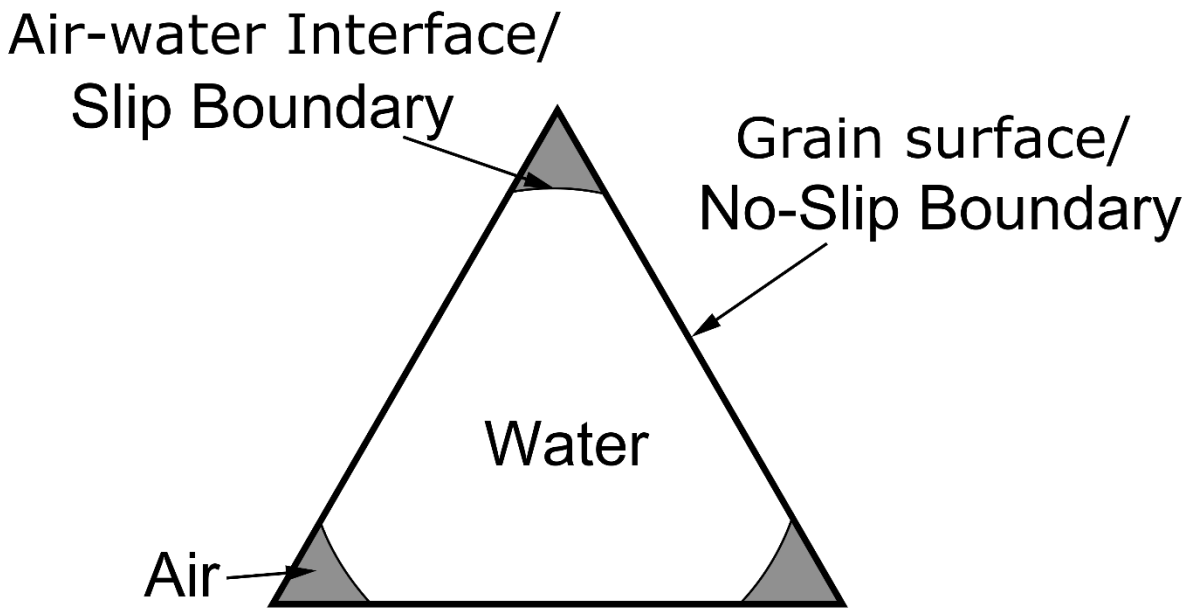

Figure 2.2: Schematic of fluid in triangular capillary tube. (reproduced from Takeuchi et al. 2017*)*

It was reported that permeability is strongly influenced by air-water interfaces in the capillary tubes, and that changes in tube size and the air-water interface were correlated with increases in permeability of the unsaturated hydrophobic porous media. Simulations also showed that flow resistance at the centre of the capillaries could be less than that of full flow under the appropriate pressure conditions, which leads to higher hydraulic conductivity of hydrophobic porous media. Wang and

Wallach, (2020) presented a slightly different approach using uniform and non-uniform capillaries to describe the reorientation process of amphiphilic molecules for water penetration. Amphiphilic molecules contain both hydrophilic and hydrophobic ends, where their orientation determines the soil wettability, allowing time dependent wettability to be exhibited by reorientation of the molecules over time. The approach was validated against measured data, demonstrating that pore geometry was very influential in terms of capillary rise dynamics for non-uniform capillaries.

The various reported capillary dynamics studies emphasise the importance of allowing for non-uniform capillaries, warranting further investigation into their relationships between water movement and wettability (Czachor et al. 2010; Takeuchi et al. 2017; Wang and Wallach 2020). Having a more detailed representation at the microscale could prompt its coupling in multi-scale models. A simple way to introduce the multilevel approach would be to evaluate soil characteristics by using a separate pore-scale model, for properties such as the hydraulic conductivity, which would then be used in a macrolevel model. This type of parameter estimation has been seen previously, where the developed model is often posed as a tool (Takeuchi et al. 2014), but would be well suited in the multi-level approach. Models of this nature are lacking when it comes to hydrophobic soils, leaving room for further work for cases where experimental determination of soil characteristics is challenging. The non-standard approach of neural networks also has more room for growth (Xiong et al. 2011). Due to the restriction in dimensions for the self-organised map, the expected high moisture content classes you would find for water repellent soils were not represented, suggesting further refinement is needed. Ultimately, the potential for use of machine learning should be recognised as it would allow complex conditions to be represented where physical intuition is not present. Similarly, there is potential for improvement in models where variable wettability is considered (Ganz et al. 2014; Wang et al. 2018). The authors found that as the level of water repellency increased, the accuracy of the model decreased, highlighting the need for caution when simulating hydrophobic soils in its current state.

2.7.2 Preferential flow and fingering

Variable flow in soils leads to the development of fingers, transporting water at an accelerated rate through distinct paths (Ritsema et al. 1993). These preferential

pathways are strongly coupled with hysteretic effects, making it challenging to model their behaviour (Glass et al., 1989; van Dam et al., 1996; DiCarlo et al., 1999; Schweizer, 2017). Once fingers are established, water will be preferentially transported through them, in contrast to steady flow where a wetting front will progressively make its way through the porous media in a uniform manner. Here, we will consider the modelling of both wettable and water repellent soils, preferential flow, and the fingers which are developed as a result.

An early attempt at describing finger growth was presented by Tamai et al. (1987). The work was relatively limited and the results did not represent the behaviour observed in laboratory experiments. This motivated the development of a model to describe the mechanisms for growth and persistence of a gravity driven finger (Nieber 1996). Hysteresis was represented in the water retention function, with the growth and persistence of a single finger being simulated, showing behaviour similar to that observed experimentally and theoretically by Parlange and Hill (1976) and Glass et al. (1989). It was seen that for subsequent wetting, the flow will follow the path of an already established finger, decreasing the water transport time to the wetting front. Nguyen et al. (1999) further extended these approaches to consider layered soils of mixed wettability, analysing how the structure would influence unstable flow patterns. Results from time domain reflectometry experiments were replicated for moisture distributions in a 2.2 m wide by 0.7 m deep trench, where it was observed that the soil's hydrophobic layer was the cause of unstable infiltration. A comparable study was carried out by Nieber et al. (2000), who captured the effects of water repellency on gravity-driven unstable flow and finger formation for a wettable and extremely water repellent sand. Detailed lab experiments (Bauters et al. 1998) were replicated, with the model being able to match the temporal changes in pressure, velocity of the wetting front, finger width and average velocity of propagation within fingers (see Figure 2.3).

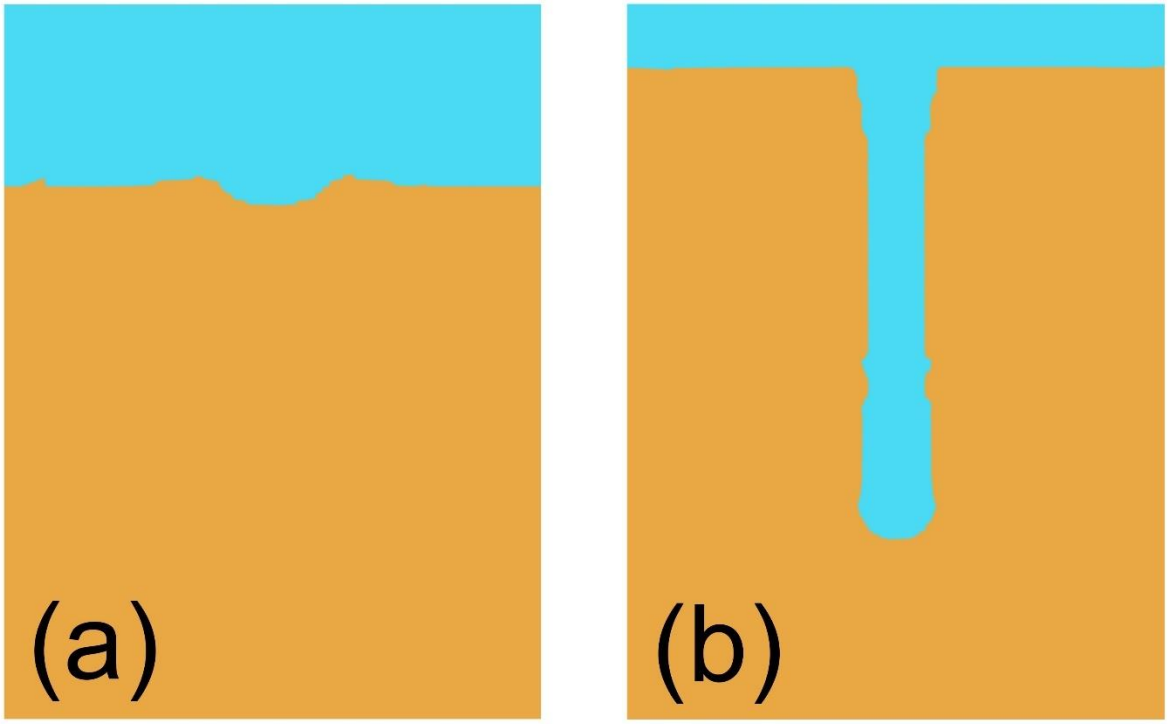

Figure 2.3: Simulated infiltration patters at similar times for (a) wettable sand, and (b) extremely water repellent sand. (reproduced from Nieber et al. 2000*)*

It was noted that to be able to evaluate the effects of varying degrees of water repellency on characteristics of unstable flow, further analysis was required resulting in the simulation of infiltrating flows being described by a non-equilibrium model (Nieber et al. 2003). The model that Nieber (1996) and Nieber et al. (2000) had developed was based on the Richards equation, which was found to be unconditionally stable (Egorov et al. 2003). As a result, the effects of the dynamic and static memory were brought into the solution for the mass balance equation in portraying finger dynamics. Hysteresis was seen to be the cause of persistence in fingers, with the degree of WR being sensitive to the saturation-pressure relationship and sufficient in causing unstable flow. This work highlighted that the presence of only low levels of WR were necessary for flow to become unstable.

Alternative approaches were used in the infancy of the field, where the formation and recurrence of fingers were simulated based on a numerical solution comprising coupled water and air flow in a 2-D domain (Ritsema et al. 1998). The heterogeneity of the soil was taken into account, with the authors claiming that the spatial variability of wettability that it infers will cause fingers to become permanent preferential

pathways. It was proposed that repeated drying and wetting of developed preferential pathways could result in leaching of hydrophobic substances from the pores of the fingers, thus changing the water retention functions and making the soil more wettable over time. Ritsema and Dekker (2000) would later consider the wider influences of transport in water repellent soils due to preferential flow, hypothesising the factors that need to be considered in the modelling process. Simulations found that preferential flow paths will only form for infiltration into a dry water repellent soil, whereas for an initially wet soil of similar wettability, stable flow patterns can be expected. Following this, a new approach was considered for representing transport and preferential flow by use of the pre-existing Soil Water Atmosphere Plant (SWAP) model (Ritsema et al. 2005). Modifications to the model were made, these being applied to an extensive field tracer experiment. Initial results showed early arrival times of bromide tracer in the subsoil, a significant change relative to that of uniform flow. Later, Kramers et al. (2005) use the modified model to analyse how crop growth and solute leaching were influenced by the addition of preferential flow . Three main flow configurations were considered within the model: (i) uniform flow, (ii) the classical mobile-immobile concept, and (iii) finger development from unstable infiltration. The use of clay amendments to the soil was simulated, whereby clay is deposited into the soil to reduce repellency levels. It was observed that without the consideration of preferential flow it was not possible to replicate experimental behaviour, implying that the physical characteristics of the soil alone are not sufficient in describing the effects of variable wettability. Parameter analysis also showed that the critical soil water content was the most influential factor in defining the presence and extremity of preferential flow.

As seen above, the applicability of HYDRUS was questioned when water repellent soils are considered. This is further reflected through its use in simulating water flow and solute transport in heterogeneous soil, showing that the expected preferential characteristics are not always observed (Buczko and Gerke 2006). The model was unable to account for hydrophobicity, where the authors suggested that hysteresis in the hydraulic functions could be the cause of the poor simulations, all pointing towards the presence of soil water repellency as the cause. The effects of heterogeneity on finger instability have been further considered by Cueto-Felgueroso et al. (2020), who used a model with a random field generation method to simulate

preferential flow during infiltration in a 2-D initially dry heterogeneous soil. Spatial heterogeneity was categorised by random spatially correlated fields of intrinsic permeability (left of Figure 2.4), allowing for isotropic and anisotropic configurations of permeability.

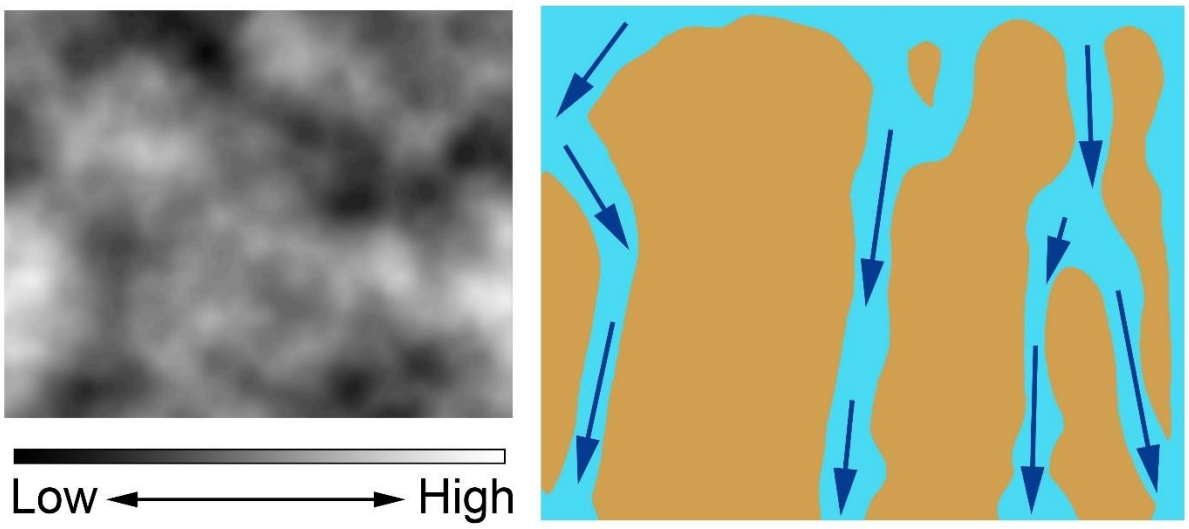

Figure 2.4: Permeability field (left) and the resulting infiltration path for gravity-driven flow. (reproduced from Cueto-Felgueroso et al. 2020*)*

The question of whether moderate or strong heterogeneity influences fingering instability was addressed, concluding that its inclusion enhanced the effects of preferential flow, leading to increased rates of finger development. For all spatial structures of intrinsic permeability considered, soil heterogeneity promoted fingering at low infiltration rates, whereas for larger infiltration rates, the finger widths were comparable to the size of the domain. It is also stated that the patterns of finger formation strongly depend on the soil structure, namely the correlation length and the form of the permeability field. It was concluded that soil heterogeneity should be considered in future modelling, being well justified due to its substantial influences on preferential flow. A similar view was shared by (Ritsema et al. 1998), suggesting that for models to have improved accuracy, unstable flow, consequent development of fingers, and heterogeneity of the porous media must be incorporated. The authors also noted that hysteresis is vital in modelling water repellent soils, especially when solute transport is considered.

2.7.3 Solute transport

In the previous section, we considered preferential flow as a result of hydrophobicity, observing that the finger like paths can accelerate water transport through porous media. This change in patterns of water movement will have a consequential impact on the advective transport of chemicals or other solutes present in the fluid phase (Gjettermann et al. 1997; Reichenberger et al. 2002; Morris and Mooney 2004). Chemicals, such as those used in agricultural processes, can make their way into reservoirs and pollute water sources, whilst also impacting water quality and water supply (Perkins et al. 2011). Understanding transport in this setting can inform waste management practises such as landfills, ensuring the long-term sustainability of their implementation. Solute transport is becoming increasingly important as the built environment continues to evolve; being able to understand, and in turn, control chemical movements will aid in environmental sustainability.

An early account of water repellency being included in a numerical model was presented by van Dam et al. (1990) and considered its effects on the transport of water and bromide tracer for a coarse textured soil. The experimental work of Hendrickx et al. (1988) was replicated using a simple numerical model based on the Richards equation and simple Fickian-based convection-dispersion relation for transport of the solute

$$\frac{\partial}{\partial \mathrm{t}}(\theta R c) = \frac{\partial}{\partial \mathrm{z}}\left(\theta D \frac{\partial c}{\partial \mathrm{z}} - q c\right) \tag{2.1}$$

where θ is the volumetric water content, R a retardation factor, c the solution concentration, D the dispersion coefficient and q is the soil water flux density such that

$$q = -K \frac{\partial h}{\partial \mathrm{z}} + K \tag{2.2}$$

where K is the unsaturated conductivity and h is the soil water pressure head. Macroscopic effects of preferential flow paths were incorporated, and the transport of water and bromide in the unsaturated soil could be predicted well using the simplistic model. Similar replication of bromide profiles has been conducted, in which the soil water content and infiltration profiles collected over a 474 day period were simulated (van den Bosch et al. 1999). The field scale model was adequate in water and bromide transport simulation, but due to its empirical nature, its applicability for other

soils of similar wettability conditions was not determined. Tracer experiments in 3-D have also been explored numerically, representing the distribution of water content, pH, bromide concentration and level of water repellency for a layered soil of varied wettability (Nguyen et al., 1999). An extension to the already established model of Nieber (1996) was conducted using random walk particle tracking, and was suitable in depicting unstable flow conditions. The model was most accurate when the solute was injected proportionally to the amount of rainfall over time, rather than as a full initial injection. It is claimed that this could imply the occurrence of partial solute mixing, and that rainfall events are necessary in mobilising all of the injected solute due to the gradual dispersion of the substance through the penetrating water. Further analysis on layered systems has been carried out, exploring the effects of a hydrophobic surface layer on solute transport in its wettable sublayer (de Rooij and de Vries 1996). The model was developed to describe the growth of a single finger, and explored the sensitivity of solute leaching to different hydraulic parameters, with the main outcome being that not accounting for a wettable layer exhibiting diverging flow below the fingers had detrimental effects upon the accuracy on the model, specifically how the fingers influence fluid flow.

More recently, the effects of wettability on the transport and retention of bacteria have been considered (Sepehrnia et al. 2018). Solute breakthrough experiments were reported considering bacterial transport through wettable and water repellent porous media of varied levels of saturation for Escherichia coli and Rhodococcus erythropolis as they are representative examples of hydrophilic and hydrophobic bacteria respectively. Figure 2.5 shows the various retention mechanisms observed in this setting.

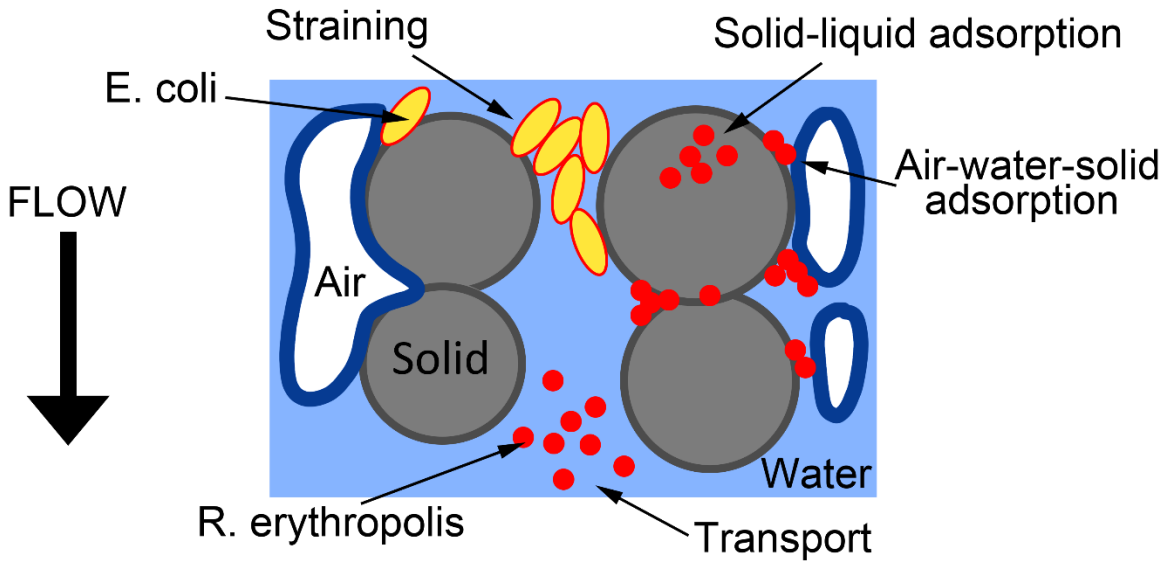

Figure 2.5: Schematic for the various retention mechanisms for Escherichia coli and Rhodococcus erythropolis in a granular 3 phase system. (reproduced from Sepehrnia et al. 2018*)*

Even though its discrepancies have been highlighted (Ganz et al. 2014; Wang et al. 2018), HYDRUS was used to build equilibrium and attachment/detachment models for transport of bromide and the given bacteria. Retention was seen to vary significantly with the type of bacteria due to their relative size and shape for all types of infiltration modes and soil wettability. The main outcomes of the study were that retention of bacteria in water repellent soils was much greater than in wettable soils, and that when dry, water repellent soil is able to not only retain, but filter bacteria. As is clear, there is considerable scope for further work in representation of bacterial dynamics in water repellent soils within numerical models. Similarly, more consideration is needed for mechanisms often neglected in the modelling process that are known to be important, such as hysteresis (Bachmann et al. 2007; Ganz et al. 2014). For the case of de Rooij and de Vries, (1996), hysteresis was neglected due to the assumption of steady state flow, on the basis that agreement between transient and steady state flow for a similar soil was observed by van Ommen et al. (1989). As hysteresis was not modelled, the size of the fingers were prescribed to account for its influence on fingered flow dynamics. This led to differing positions from which the fingers would infiltrate, and was justified due to the movement of water or solute through either a few large or many small fingers being not significant for correctly representing solute leaching. Similar revisions were suggested for the

model of van den Bosch et al. (1999), due to a lack of unsteady infiltration being observed which was thought to be due to either uniform vegetation cover, or a thicker topsoil than is usually present in water repellent sandy soils. Much of the limited amount of work in this area predates the second millennia and needs further investigation.

2.8 Discussion and Conclusions

This chapter presented research relating to the modelling of soils, largely on flow processes in unsaturated soils for different wettabilities and the effects of soil heterogeneity. Field generation methods were also considered as their use in soil modelling is well-established.

Through conducting this review, gaps in the literature have been identified. In many cases, a 2-D representation of a given problem can give conservative results, potentially underestimating the soil response. Many processes in soil are inherently 3-D, and should be modelled as such. Similarly, hysteresis is not accounted for when modelling soils of all wettabilities. This is a key mechanism that effects the wetting and drying behaviour of soils, and is particularly important when considering water repellent soils.

It was also noted that very few studies have been conducted in explicitly representing fingered flow, especially in a stochastic manner. Much of the work is concerned with field scale simulations of slope stability for heterogeneous soil. The use of random fields allows soil heterogeneity to be represented such that fingered flow can be induced. This stochastic approach enables the quantification of fingered flow characteristics in a non-deterministic manner. Similarly, the error associated with random field generation in the near-boundary region is not very well understood. Systematic approaches should be taken to find methods to mitigate this error and preserve the desired field correlation structure.

The most important conclusion that can be drawn from the presented studies, is that material heterogeneity strongly influences the behaviour of complex phenomena in soil, and should be accounted for when modelling. Most coupled models do not account for material heterogeneity also, and focus on the coupling of the material behaviour under certain conditions. The vast amount of literature on coupled models suggests the need for extension to account for material heterogeneity. Similarly, little

has been considered for heterogeneous water repellent soils. The presence of water repellency and its variability in the domain are known to be strong driving forces in the unstable flow response that is commonly observed. The combination of a non-uniform material -as well as its non-uniform wettability- will lead to a highly non-linear system, and should be further investigated.

2.9 References

Arregui-Mena, J.D., Margetts, L. and Mummery, P.M. 2016. Practical Application of the Stochastic Finite Element Method. Archives of Computational Methods in Engineering 23(1), pp. 171–190. doi: 10.1007/s11831-014-9139-3.

Bachmann, J., Deurer, M. and Arye, G. 2007. Modeling Water Movement in Heterogeneous Water-Repellent Soil: 1. Development of a Contact Angle-Dependent Water-Retention Model. Vadose Zone Journal 6(3), pp. 436–445. Available at: http://doi.wiley.com/10.2136/vzj2006.0060.

Bauters, T.W.J., Steenhuis, T.S., Parlange, J.-Y. and DiCarlo, D.A. 1998. Preferential Flow in Water-Repellent Sands. Soil Science Society of America Journal 62(5), pp. 1185–1190. Available at: http://doi.wiley.com/10.2136/sssaj1998.03615995006200050005x.

Blunt, M.J., Jackson, M.D., Piri, M. and Valvatne, P.H. 2002. Detailed physics, predictive capabilities and macroscopic consequences for pore-network models of multiphase flow. Advances in Water Resources 25(8–12), pp. 1069–1089. Available at: https://linkinghub.elsevier.com/retrieve/pii/S0309170802000490.

Bodí, M.B., Doerr, S.H., Cerdà, A. and Mataix-Solera, J. 2012. Hydrological effects of a layer of vegetation ash on underlying wettable and water repellent soil. Geoderma 191, pp. 14–23. Available at: https://linkinghub.elsevier.com/retrieve/pii/S0016706112000286.

Bolin, D. and Kirchner, K. 2020. The Rational SPDE Approach for Gaussian Random Fields With General Smoothness. Journal of Computational and Graphical Statistics 29(2), pp. 274–285. doi: 10.1080/10618600.2019.1665537.

van den Bosch, H., Ritsema, C.J., Boesten, J.J.T.I., Dekker, L.W. and Hamminga, W. 1999. Simulation of water flow and bromide transport in a water repellent sandy soil using a one-dimensional convection-dispersion model. Journal of Hydrology 215(1–4), pp. 172–187. Available at: https://linkinghub.elsevier.com/retrieve/pii/S0022169498002686.

Brindt, N. and Wallach, R. 2017. The moving-boundary approach for modeling gravity-driven stable and unstable flow in soils. Water Resources Research 53(1), pp. 344–360. Available at: http://doi.wiley.com/10.1002/2016WR019252.

Brindt, N. and Wallach, R. 2020. The Moving-Boundary Approach for Modeling 2-D Gravity-Driven Stable and Unstable Flow in Partially Wettable Soils. Water Resources Research 56(5). Available at: https://onlinelibrary.wiley.com/doi/10.1029/2019WR025772.

Brown, H. et al. 2018. Modelling soil-water dynamics in the rootzone of structured and water-repellent soils. Computers & Geosciences 113, pp. 33–42. Available at: https://linkinghub.elsevier.com/retrieve/pii/S0098300418300529.

Buczko, U. and Gerke, H.H. 2006. Modeling Two-Dimensional Water Flow and Bromide Transport in a Heterogeneous Lignitic Mine Soil. Vadose Zone Journal 5(1), pp. 14–26. Available at: http://doi.wiley.com/10.2136/vzj2005.0003.

Calvetti, D. et al. 2015a. Artificial boundary conditions and domain truncation in electrical impedance tomography. Part I: Theory and preliminary results. Inverse Problems and Imaging 9(3), pp. 749–766. doi: 10.3934/ipi.2015.9.749.

Calvetti, D., Hadwin, P.J., Huttunen, J.M.J., Kaipio, J.P. and Somersalo, E. 2015b. Artificial boundary conditions and domain truncation in electrical impedance tomography. Part II: Stochastic extension of the boundary map. Inverse Problems and Imaging 9(3), pp. 767–789. doi: 10.3934/ipi.2015.9.767.

Cavalcante, A.L.B., Borges, L.P. de F. and Zornberg, J.G. 2019. New 3D Analytical Solution for Modeling Transient Unsaturated Flow Due to Wetting and Drying. International Journal of Geomechanics 19(7). doi: 10.1061/(ASCE)GM.1943-5622.0001461.

Cerdà, A. 1998. Changes in overland flow and infiltration after a rangeland fire in a Mediterranean scrubland. Hydrological Processes 12(7), pp. 1031–1042. Available at: https://onlinelibrary.wiley.com/doi/10.1002/(SICI)1099-1085(19980615)12:7<1031::AID-HYP636>3.0.CO;2-V.

Cerdà, A. and Doerr, S.H. 2008. The effect of ash and needle cover on surface runoff and erosion in the immediate post-fire period. CATENA 74(3), pp. 256–263. Available at: https://linkinghub.elsevier.com/retrieve/pii/S0341816208000222.

Chen, G., Neuman, S.P. and Hills, R.G. 2000. Wetting front instability and fingering in random permeability fields. In: Theory, modeling, and field investigation in

hydrogeology: a special volume in honor of Shlomo P. Neumans 60th birthday. Geological Society of America. doi: 10.1130/0-8137-2348-5.53.

Chen, J., Pangle, L.A., Gannon, J.P. and Stewart, R.D. 2020. Soil water repellency after wildfires in the Blue Ridge Mountains, United States. International Journal of Wildland Fire 29(11), p. 1009. doi: 10.1071/WF20055.

Cheng, H., Chen, J., Chen, R., Chen, G. and Zhong, Y. 2018. Risk assessment of slope failure considering the variability in soil properties. Computers and Geotechnics 103, pp. 61–72. doi: 10.1016/j.compgeo.2018.07.006.

Chi, S., Feng, W., Jia, Y. and Zhang, Z. 2022. Application of the soil parameter random field in the 3D random finite element analysis of Guanyinyan composite dam. Case Studies in Construction Materials 17, p. e01329. doi: 10.1016/j.cscm.2022.e01329.

Cho, S.E. 2012. Probabilistic analysis of seepage that considers the spatial variability of permeability for an embankment on soil foundation. Engineering Geology 133–134, pp. 30–39. doi: 10.1016/j.enggeo.2012.02.013.

Cho, S.E. 2016. Stability analysis of unsaturated soil slopes considering water-air flow caused by rainfall infiltration. Engineering Geology 211, pp. 184–197. doi: 10.1016/j.enggeo.2016.07.008.

Coelho, C. de O.A., Ferreira, A.J.D., Boulet, A.-K. and Keizer, J.J. 2004. Overland flow generation processes, erosion yields and solute loss following different intensity fires. Quarterly Journal of Engineering Geology and Hydrogeology 37(3), pp. 233–240. doi: 10.1144/1470-9236/03-043.

Cueto-Felgueroso, L., Suarez-Navarro, M.J., Fu, X. and Juanes, R. 2020. Numerical Simulation of Unstable Preferential Flow during Water Infiltration into Heterogeneous Dry Soil. Water 12(3), p. 909. doi: 10.3390/w12030909.

Czachor, H., Doerr, S.H. and Lichner, L. 2010. Water retention of repellent and subcritical repellent soils: New insights from model and experimental investigations. Journal of Hydrology 380(1–2), pp. 104–111. Available at: https://linkinghub.elsevier.com/retrieve/pii/S0022169409006866.

van Dam, J.C., Hendrickx, J.M.H., van Ommen, H.C., Bannink, M.H., van Genuchten, M.Th. and Dekker, L.W. 1990. Water and solute movement in a coarse-textured water-repellent field soil. Journal of Hydrology 120(1–4), pp. 359–379. Available at: https://linkinghub.elsevier.com/retrieve/pii/002216949090159U.

van Dam, J.C., Wösten, J.H.M. and Nemes, A. 1996. Unsaturated soil water movement in hysteretic and water repellent field soils. Journal of Hydrology 184(3–4), pp. 153–173. Available at: https://linkinghub.elsevier.com/retrieve/pii/0022169495029966.

Daon, Y. and Stadler, G. 2018. Mitigating the influence of the boundary on PDE-based covariance operators. Inverse Problems & Imaging 12(5), pp. 1083–1102. doi: 10.3934/ipi.2018045.

Davydzenka, T., Fagbemi, S. and Tahmasebi, P. 2020. Wettability control on deformation: Coupled multiphase fluid and granular systems. Physical Review E 102(1), p. 013301. Available at: https://link.aps.org/doi/10.1103/PhysRevE.102.013301.

DeBano, L.F. 2000a. The role of fire and soil heating on water repellency in wildland environments: a review. Journal of Hydrology 231–232, pp. 195–206. doi: 10.1016/S0022-1694(00)00194-3.

DeBano, L.F. 2000b. Water repellency in soils: a historical overview. Journal of Hydrology 231–232, pp. 4–32. Available at: https://linkinghub.elsevier.com/retrieve/pii/S0022169400001803.

DiCarlo, D.A., Bauters, T.W.J., Darnault, C.J.G., Steenhuis, T.S. and Parlange, J.-Y. 1999. Lateral expansion of preferential flow paths in sands. Water Resources Research 35(2), pp. 427–434. Available at: http://doi.wiley.com/10.1029/1998WR900061.

Doerr, S.H., Blake, W.H., Shakesby, R.A., Stagnitti, F., Vuurens, S.H., Humphreys, G.S. and Wallbrink, P. 2004. Heating effects on water repellency in Australian eucalypt forest soils and their value in estimating wildfire soil temperatures. International Journal of Wildland Fire 13(2), p. 157. doi: 10.1071/WF03051.

Doerr, S.H., Shakesby, R.A. and Walsh, R.P.D. 2000. Soil water repellency: its causes, characteristics and hydro-geomorphological significance. Earth-Science Reviews 51(1–4), pp. 33–65. Available at: https://linkinghub.elsevier.com/retrieve/pii/S0012825200000118.

Egorov, A.G., Dautov, R.Z., Nieber, J.L. and Sheshukov, A.Y. 2003. Stability analysis of gravity-driven infiltrating flow. Water Resources Research 39(9). Available at: http://doi.wiley.com/10.1029/2002WR001886.

Elkateb, T., Chalaturnyk, R. and Robertson, P.K. 2003. An overview of soil heterogeneity: quantification and implications on geotechnical field problems. Canadian Geotechnical Journal 40(1), pp. 1–15. doi: 10.1139/t02-090.

Fenton, G.A. and Vanmarcke, E.H. 1990. Simulation of Random Fields via Local Average Subdivision. Journal of Engineering Mechanics 116(8), pp. 1733–1749. doi: 10.1061/(ASCE)0733-9399(1990)116:8(1733).

Ferreira, A.J.D., Coelho, C.O.A., Boulet, A.K., Leighton-Boyce, G., Keizer, J.J. and Ritsema, C.J. 2005. Influence of burning intensity on water repellency and hydrological processes at forest and shrub sites in Portugal. Soil Research 43(3), p. 327. doi: 10.1071/SR04084.

Fuglstad, G.-A., Simpson, D., Lindgren, F. and Rue, H. 2015. Does non-stationary spatial data always require non-stationary random fields? Spatial Statistics 14, pp. 505–531. doi: 10.1016/j.spasta.2015.10.001.

Gandolfi, C., Facchi, A. and Maggi, D. 2006. Comparison of 1D models of water flow in unsaturated soils. Environmental Modelling & Software 21(12), pp. 1759–1764. doi: 10.1016/j.envsoft.2006.04.004.

Ganz, C., Bachmann, J., Noell, U., Duijnisveld, W.H.M. and Lamparter, A. 2014. Hydraulic Modeling and in situ Electrical Resistivity Tomography to Analyze Ponded Infiltration into a Water Repellent Sand. Vadose Zone Journal 13(1), p. vzj2013.04.0074. Available at: http://doi.wiley.com/10.2136/vzj2013.04.0074.

Gelhar, L.W. and Axness, C.L. 1983. Three-dimensional stochastic analysis of macrodispersion in aquifers. Water Resources Research 19(1), pp. 161–180. doi: 10.1029/WR019i001p00161.

van Genuchten, M.Th. 1980. A Closed-form Equation for Predicting the Hydraulic Conductivity of Unsaturated Soils. Soil Science Society of America Journal 44(5), pp. 892–898. doi: 10.2136/sssaj1980.03615995004400050002x.

Gjettermann, B., Nielsen, K.L., Petersen, C.T., Jensen, H.E. and Hansen, S. 1997. Preferential flow in sandy loam soils as affected by irrigation intensity. Soil Technology 11(2), pp. 139–152. Available at: https://linkinghub.elsevier.com/retrieve/pii/S0933363097000019.

Glass, R.J., Parlange, J.-Y. and Steenhuis, T.S. 1989. Wetting front instability: 1. Theoretical discussion and dimensional analysis. Water Resources Research 25(6), pp. 1187–1194. Available at: http://doi.wiley.com/10.1029/WR025i006p01187.

Gómez-Hernández, J.J. and Cassiraga, E.F. 1994. Theory and Practice of Sequential Simulation. pp. 111–124. doi: 10.1007/978-94-015-8267-4_10.

Granged, A.J.P., Jordán, A., Zavala, L.M. and Bárcenas, G. 2011. Fire-induced changes in soil water repellency increased fingered flow and runoff rates following the 2004 Huelva wildfire. Hydrological Processes 25(10), pp. 1614–1629. Available at: https://onlinelibrary.wiley.com/doi/10.1002/hyp.7923.

Hallett, P.D. 2008. A brief overview of the causes, impacts and amelioration of soil water repellency – a review. Soil and Water Research 3(Special Issue No. 1), pp. S21–S29. Available at: http://www.agriculturejournals.cz/web/swr.htm?volume=3&firstPage=S21&type=publishedArticle.

Hammel, K., Gross, J., Wessolek, G. and Roth, K. 1999. Two-dimensional simulation of bromide transport in a heterogeneous field soil with transient unsaturated flow. European Journal of Soil Science 50(4), pp. 633–647. doi: 10.1046/j.1365-2389.1999.00273.x.

Hendrickx, J.M.H., Dekker, L.W., van Zuilen, E.J. and Boersma, O.H. 1988. Water and solute movement in a coarse-textured water-repellent field soil. In: Proceedings of a Conference on the Validation of Flow and Transport Models for the Unsaturated Zone. Ruidoso, New Mexico, pp. 131–146.

Hicks, M.A., Nuttall, J.D. and Chen, J. 2014. Influence of heterogeneity on 3D slope reliability and failure consequence. Computers and Geotechnics 61, pp. 198–208. doi: 10.1016/j.compgeo.2014.05.004.

Hu, R., Chen, Y.-F., Liu, H.-H. and Zhou, C.-B. 2016. A coupled two-phase fluid flow and elastoplastic deformation model for unsaturated soils: theory, implementation, and application. International Journal for Numerical and Analytical Methods in Geomechanics 40(7), pp. 1023–1058. doi: 10.1002/nag.2473.

Huang, H.W., Xiao, L., Zhang, D.M. and Zhang, J. 2017. Influence of spatial variability of soil Young's modulus on tunnel convergence in soft soils. Engineering Geology 228, pp. 357–370. doi: 10.1016/j.enggeo.2017.09.011.

Hungr, O. 1987. An extension of Bishop's simplified method of slope stability analysis to three dimensions. Géotechnique 37(1), pp. 113–117. doi: 10.1680/geot.1987.37.1.113.

Jiang, S.H., Huang, J., Griffiths, D. V. and Deng, Z.P. 2022. Advances in reliability and risk analyses of slopes in spatially variable soils: A state-of-the-art review. Computers and Geotechnics 141. doi: 10.1016/j.compgeo.2021.104498.

Jiang, S.-H., Huang, J., Huang, F., Yang, J., Yao, C. and Zhou, C.-B. 2018. Modelling of spatial variability of soil undrained shear strength by conditional random fields for slope reliability analysis. Applied Mathematical Modelling 63, pp. 374–389. doi: 10.1016/j.apm.2018.06.030.

Johansen, M.P., Hakonson, T.E. and Breshears, D.D. 2001. Post-fire runoff and erosion from rainfall simulation: contrasting forests with shrublands and grasslands. Hydrological Processes 15(15), pp. 2953–2965. doi: 10.1002/hyp.384.

Khristenko, U., Scarabosio, L., Swierczynski, P., Ullmann, E. and Wohlmuth, B. 2019. Analysis of Boundary Effects on PDE-Based Sampling of Whittle--Matérn Random Fields. SIAM/ASA Journal on Uncertainty Quantification 7(3), pp. 948–974. doi: 10.1137/18M1215700.

Kramers, G., van Dam, J.C., Ritsema, C.J., Stagnitti, F., Oostindie, K. and Dekker, L.W. 2005. A new modelling approach to simulate preferential flow and transport in water repellent porous media: Parameter sensitivity, and effects on crop growth and

solute leaching. Soil Research 43(3), p. 371. Available at: http://www.publish.csiro.au/?paper=SR04098.

Kuhlmann, A., Neuweiler, I., van der Zee, S.E.A.T.M. and Helmig, R. 2012. Influence of soil structure and root water uptake strategy on unsaturated flow in heterogeneous media. Water Resources Research 48(2). doi: 10.1029/2011WR010651.

Lang, A. and Potthoff, J. 2011. Fast simulation of Gaussian random fields. Available at: http://arxiv.org/abs/1105.2737.

Le, T.M.H., Gallipoli, D., Sanchez, M. and Wheeler, S.J. 2012. Stochastic analysis of unsaturated seepage through randomly heterogeneous earth embankments. International Journal for Numerical and Analytical Methods in Geomechanics 36(8), pp. 1056–1076. doi: 10.1002/nag.1047.

Lekshmi, K.R.A. and Arnepalli, D.N. 2017. A Review on Coupled Heat and Water Vapour Transport in Unsaturated Soils. In: Geotechnical Frontiers 2017. Reston, VA: American Society of Civil Engineers, pp. 746–755. doi: 10.1061/9780784480472.079.

Letey, J., Carrillo, M.L.K. and Pang, X.P. 2000. Approaches to characterize the degree of water repellency. Journal of Hydrology 231–232, pp. 61–65. Available at: https://linkinghub.elsevier.com/retrieve/pii/S0022169400001839.

Li, D.-Q., Jiang, S.-H., Cao, Z.-J., Zhou, W., Zhou, C.-B. and Zhang, L.-M. 2015. A multiple response-surface method for slope reliability analysis considering spatial variability of soil properties. Engineering Geology 187, pp. 60–72. doi: 10.1016/j.enggeo.2014.12.003.

Li, D.-Q., Xiao, T., Zhang, L.-M. and Cao, Z.-J. 2019. Stepwise covariance matrix decomposition for efficient simulation of multivariate large-scale three-dimensional random fields. Applied Mathematical Modelling 68, pp. 169–181. doi: 10.1016/j.apm.2018.11.011.

Li, H. and Zhang, D. 2007. Probabilistic collocation method for flow in porous media: Comparisons with other stochastic methods. Water Resources Research 43(9). doi: 10.1029/2006WR005673.

Li, H. and Zhang, D. 2009. Efficient and Accurate Quantification of Uncertainty for Multiphase Flow With the Probabilistic Collocation Method. SPE Journal 14(04), pp. 665–679. doi: 10.2118/114802-PA.

Li, W., Lu, Z. and Zhang, D. 2009. Stochastic analysis of unsaturated flow with probabilistic collocation method. Water Resources Research 45(8). doi: 10.1029/2008WR007530.

Li, Y.J., Hicks, M.A. and Vardon, P.J. 2016. Uncertainty reduction and sampling efficiency in slope designs using 3D conditional random fields. Computers and Geotechnics 79, pp. 159–172. doi: 10.1016/j.compgeo.2016.05.027.

Lindgren, F., Bolin, D. and Rue, H. 2022. The SPDE approach for Gaussian and non-Gaussian fields: 10 years and still running. Spatial Statistics 50. doi: 10.1016/j.spasta.2022.100599.

Lindgren, F., Rue, H. and Lindström, J. 2011. An explicit link between Gaussian fields and Gaussian Markov random fields: the stochastic partial differential equation approach.

Liu, H.H., Zhang, R. and Bodvarsson, G.S. 2005. An active region model for capturing fractal flow patterns in unsaturated soils: Model development. Journal of Contaminant Hydrology 80(1–2), pp. 18–30. doi: 10.1016/j.jconhyd.2005.07.002.

Liu, R. and Welfert, B.D. 2020. Reduced Model of One-Dimensional Unsaturated Flow in Heterogeneous Soils with Spatially Stochastic Soil Hydraulic Conductivities. International Journal of Geomechanics 20(3). doi: 10.1061/(ASCE)GM.1943-5622.0001563.

Liu, Y., Li, J., Sun, S. and Yu, B. 2019. Advances in Gaussian random field generation: a review. Computational Geosciences 23(5), pp. 1011–1047. doi: 10.1007/s10596-019-09867-y.

Liu, Y., Zhang, W., Zhang, L., Zhu, Z., Hu, J. and Wei, H. 2018. Probabilistic stability analyses of undrained slopes by 3D random fields and finite element methods. Geoscience Frontiers 9(6), pp. 1657–1664. doi: 10.1016/j.gsf.2017.09.003.

Lloret-Cabot, M., Fenton, G.A. and Hicks, M.A. 2014. On the estimation of scale of fluctuation in geostatistics. Georisk: Assessment and Management of Risk for

Engineered Systems and Geohazards 8(2), pp. 129–140. doi: 10.1080/17499518.2013.871189.

Malkinson, D. and Wittenberg, L. 2011. Post fire induced soil water repellency—Modeling short and long-term processes. Geomorphology 125(1), pp. 186–192. Available at: https://linkinghub.elsevier.com/retrieve/pii/S0169555X10004071.

Mantoglou, A. and Gelhar, LynnW. 1989. Three-dimensional unsaturated flow in heterogeneous systems and implications on groundwater contamination: A stochastic approach. Transport in Porous Media 4(6). doi: 10.1007/BF00223626.

Mataix-Solera, J. and Doerr, S.H. 2004. Hydrophobicity and aggregate stability in calcareous topsoils from fire-affected pine forests in southeastern Spain. Geoderma 118(1–2), pp. 77–88. doi: 10.1016/S0016-7061(03)00185-X.

McKissock, I., Gilkes, R.J., Harper, R.J. and Carter, D.J. 1998. Relationships of water repellency to soil properties for different spatial scales of study. Soil Research 36(3), p. 495. doi: 10.1071/S97071.

Montoya-Noguera, S., Zhao, T., Hu, Y., Wang, Y. and Phoon, K.-K. 2019. Simulation of non-stationary non-Gaussian random fields from sparse measurements using Bayesian compressive sampling and Karhunen-Loève expansion. Structural Safety 79, pp. 66–79. doi: 10.1016/j.strusafe.2019.03.006.

Morris, C. and Mooney, S.J. 2004. A high-resolution system for the quantification of preferential flow in undisturbed soil using observations of tracers. Geoderma 118(1–2), pp. 133–143. Available at: https://linkinghub.elsevier.com/retrieve/pii/S0016706103001897.

Mousavi Nezhad, M., Javadi, A.A. and Abbasi, F. 2011. Stochastic finite element modelling of water flow in variably saturated heterogeneous soils. International Journal for Numerical and Analytical Methods in Geomechanics 35(12), pp. 1389–1408. doi: 10.1002/nag.966.

Mualem, Y. 1976. A new model for predicting the hydraulic conductivity of unsaturated porous media. Water Resources Research 12(3), pp. 513–522. doi: 10.1029/WR012i003p00513.

Nakagawa, K., Saito, M. and Berndtsson, R. 2012. On the importance of hysteresis and heterogeneity in the numerical simulation of unsaturated flow. Hydrological Research Letters 6(0), pp. 59–64. doi: 10.3178/hrl.6.59.

Ng, C.W.W., Qu, C., Ni, J. and Guo, H. 2022. Three-dimensional reliability analysis of unsaturated soil slope considering permeability rotated anisotropy random fields. Computers and Geotechnics 151, p. 104944. doi: 10.1016/j.compgeo.2022.104944.

Nguyen, H.V., Nieber, J.L., Oduro, P., Ritsema, C.J., Dekker, L.W. and Steenhuis, T.S. 1999a. Modeling solute transport in a water repellent soil. Journal of Hydrology 215(1–4), pp. 188–201. Available at: https://linkinghub.elsevier.com/retrieve/pii/S0022169498002704.

Nguyen, H.V., Nieber, J.L., Ritsema, C.J., Dekker, L.W. and Steenhuis, T.S. 1999b. Modeling gravity driven unstable flow in a water repellent soil. Journal of Hydrology 215(1–4), pp. 202–214. Available at: https://linkinghub.elsevier.com/retrieve/pii/S0022169498002698.

Nieber, J., Sheshukov, A., Egorov, A. and Dautov, R. 2003. Non-equilibrium model for gravity-driven fingering in water repellent soils: Formulation and 2D simulations. In: Soil Water Repellency. Elsevier, pp. 245–257. Available at: https://linkinghub.elsevier.com/retrieve/pii/B9780444512697500254.

Nieber, J.L. 1996. Modeling finger development and persistence in initially dry porous media. Geoderma 70(2–4), pp. 207–229. Available at: https://linkinghub.elsevier.com/retrieve/pii/0016706195000860.

Nieber, J.L., Bauters, T.W.J., Steenhuis, T.S. and Parlange, J.-Y. 2000. Numerical simulation of experimental gravity-driven unstable flow in water repellent sand. Journal of Hydrology 231–232, pp. 295–307. Available at: https://linkinghub.elsevier.com/retrieve/pii/S002216940000202X.

Nyman, P., Sheridan, G.J., Smith, H.G. and Lane, P.N.J. 2014. Modeling the effects of surface storage, macropore flow and water repellency on infiltration after wildfire. Journal of Hydrology 513, pp. 301–313. Available at: https://linkinghub.elsevier.com/retrieve/pii/S0022169414001528.

Olsson, A. and Sandberg, G. 2002. Latin Hypercube Sampling for Stochastic Finite Element Analysis. Journal of Engineering Mechanics 128(1), pp. 121–125. doi: 10.1061/(ASCE)0733-9399(2002)128:1(121).

van Ommen, H.C., van Genuchten, M.Th., van der Molen, W.H., Dijksma, R. and Hulshof, J. 1989. Experimental and theoretical analysis of solute transport from a diffuse source of pollution. Journal of Hydrology 105(3–4), pp. 225–251. Available at: https://linkinghub.elsevier.com/retrieve/pii/0022169489901066.

Ou-Yang, J.-Y., Liu, Y., Yao, K., Yang, C.-J. and Niu, H.-F. 2021. Model Updating of Slope Stability Analysis Using 3D Conditional Random Fields. ASCE-ASME Journal of Risk and Uncertainty in Engineering Systems, Part A: Civil Engineering 7(3). doi: 10.1061/AJRUA6.0001150.

Pannkuk, C.D. and Robichaud, P.R. 2003. Effectiveness of needle cast at reducing erosion after forest fires. Water Resources Research 39(12). Available at: http://doi.wiley.com/10.1029/2003WR002318.

Parlange, J.-Y. and Hill, D.E. 1976. Theoretical analysis of wetting front instability in soils. Soil Science 122(4), pp. 236–239. Available at: http://journals.lww.com/00010694-197610000-00008.

Perkins, K.S., Nimmo, J.R., Rose, C.E. and Coupe, R.H. 2011. Field tracer investigation of unsaturated zone flow paths and mechanisms in agricultural soils of northwestern Mississippi, USA. Journal of Hydrology 396(1–2), pp. 1–11. Available at: https://linkinghub.elsevier.com/retrieve/pii/S0022169410005895.

Prosser, I.P. and Williams, L. 1998. The effect of wildfire on runoff and erosion in nativeEucalyptus forest. Hydrological Processes 12(2), pp. 251–265. doi: 10.1002/(SICI)1099-1085(199802)12:2<251::AID-HYP574>3.0.CO;2-4.

Raoof, A. and Hassanizadeh, S.M. 2012. A new formulation for pore-network modeling of two-phase flow. Water Resources Research 48(1). Available at: http://doi.wiley.com/10.1029/2010WR010180.

Reichenberger, S., Amelung, W., Laabs, V., Pinto, A., Totsche, K.U. and Zech, W. 2002. Pesticide displacement along preferential flow pathways in a Brazilian Oxisol.

Geoderma 110(1–2), pp. 63–86. Available at: https://linkinghub.elsevier.com/retrieve/pii/S0016706102001829.

Richards, L.A. 1931. CAPILLARY CONDUCTION OF LIQUIDS THROUGH POROUS MEDIUMS. Physics 1(5), pp. 318–333. doi: 10.1063/1.1745010.

Ritsema, C.J., van Dam, J.C., Dekker, L.W. and Oostindie, K. 2005. A new modelling approach to simulate preferential flow and transport in water repellent porous media: Model structure and validation. Soil Research 43(3), p. 361. Available at: http://www.publish.csiro.au/?paper=SR05054.

Ritsema, C.J. and Dekker, L.W. 2000. Preferential flow in water repellent sandy soils: principles and modeling implications. Journal of Hydrology 231–232, pp. 308–319. Available at: https://linkinghub.elsevier.com/retrieve/pii/S0022169400002031.

Ritsema, C.J., Dekker, L.W., Hendrickx, J.M.H. and Hamminga, W. 1993. Preferential flow mechanism in a water repellent sandy soil. Water Resources Research 29(7), pp. 2183–2193. Available at: http://doi.wiley.com/10.1029/93WR00394.

Ritsema, C.J., Dekker, L.W., Nieber, J.L. and Steenhuis, T.S. 1998. Modeling and field evidence of finger formation and finger recurrence in a water repellent sandy soil. Water Resources Research 34(4), pp. 555–567. Available at: http://doi.wiley.com/10.1029/97WR02407.

Roininen, L., Huttunen, J.M.J. and Lasanen, S. 2014. Whittle-matérn priors for Bayesian statistical inversion with applications in electrical impedance tomography. Inverse Problems and Imaging 8(2), pp. 561–586. doi: 10.3934/ipi.2014.8.561.

de Rooij, G.H. and de Vries, P. 1996. Solute leaching in a sandy soil with a water-repellent surface layer: A simulation. Geoderma 70(2–4), pp. 253–263. Available at: https://linkinghub.elsevier.com/retrieve/pii/001670619500081X.

Rubin, Y. and Or, D. 1993. Stochastic modeling of unsaturated flow in heterogeneous soils with water uptake by plant roots: The Parallel Columns Model. Water Resources Research 29(3), pp. 619–631. doi: 10.1029/92WR02292.

Schweizer, B. 2017. Hysteresis in porous media: Modelling and analysis. Interfaces and Free Boundaries 19(3), pp. 417–447. Available at: https://ems.press/doi/10.4171/ifb/388.

Sepehrnia, N., Bachmann, J., Hajabbasi, M.A., Afyuni, M. and Horn, M.A. 2018. Modeling Escherichia coli and Rhodococcus erythropolis transport through wettable and water repellent porous media. Colloids and Surfaces B: Biointerfaces 172, pp. 280–287. Available at: https://linkinghub.elsevier.com/retrieve/pii/S0927776518305757.

Shakesby, R. and Doerr, S. 2006. Wildfire as a hydrological and geomorphological agent. Earth-Science Reviews 74(3–4), pp. 269–307. Available at: https://linkinghub.elsevier.com/retrieve/pii/S0012825205001467.

Sheng, F., Liu, H., Wang, K., Zhang, R. and Tang, Z. 2014. Investigation into preferential flow in natural unsaturated soils with field multiple-tracer infiltration experiments and the active region model. Journal of Hydrology 508, pp. 137–146. doi: 10.1016/j.jhydrol.2013.10.048.

Sheng, F., Liu, H., Zhang, R. and Wang, K. 2012. Determining the active region model parameter from dye staining experiments for characterizing the preferential flow heterogeneity in unsaturated soils. Environmental Earth Sciences 65(7), pp. 1977–1985. doi: 10.1007/s12665-011-1178-6.

Sheng, F., Wang, K., Zhang, R. and Liu, H. 2011. Modeling preferential water flow and solute transport in unsaturated soil using the active region model. Environmental Earth Sciences 62(7), pp. 1491–1501. doi: 10.1007/s12665-010-0633-0.

Siemens, G., Oldroyd, C. and Beddoe, R. 2021. Flow Cell with High-Resolution Spatial and Temporal Degree of Saturation Measurements for Two-Dimensional Near-Surface Phenomena Using Unsaturated Transparent Soil. Geotechnical Testing Journal 44(6), p. 20200082. doi: 10.1520/GTJ20200082.

Sililo, O.T.N. and Tellam, J.H. 2000. Fingering in Unsaturated Zone Flow: A Qualitative Review with Laboratory Experiments on Heterogeneous Systems. Ground Water 38(6), pp. 864–871. doi: 10.1111/j.1745-6584.2000.tb00685.x.

Srivastava, A., Babu, G.L.S. and Haldar, S. 2010. Influence of spatial variability of permeability property on steady state seepage flow and slope stability analysis. Engineering Geology 110(3–4), pp. 93–101. doi: 10.1016/j.enggeo.2009.11.006.

Takeuchi, J., Takahashi, T. and Fujihara, M. 2014. Sub-darcy-scale modeling of non-uniform flow through porous media with mixed wettabilities. International Journal of Geomate 6(2), pp. 840–847. Available at: https://geomatejournal.com/geomate/article/view/2926/2479.

Takeuchi, J., Tsuji, H. and Fujihara, M. 2017. Modeling of permeability of porous media with mixed wettabilities based on noncircular capillaries. International Journal of GEOMATE 12(34), pp. 1–7. Available at: https://geomatejournal.com/geomate/article/view/1353/1294.

Tamai, N., Asaeda, T. and Jeevaraj, C.G. 1987. Fingering in two-dimensional, homogeneous, unsaturated porous media. Soil Science 144(2), pp. 107–112. Available at: http://journals.lww.com/00010694-198708000-00004.

Tang, K., Wang, J. and Li, L. 2020. A prediction method based on Monte Carlo simulations for finite element analysis of soil medium considering spatial variability in soil parameters. Advances in Materials Science and Engineering 2020. doi: 10.1155/2020/7064640.

Terry, J.P. and Shakesby, R.A. 1993. Soil hydrophobicity effects on rainsplash: Simulated rainfall and photographic evidence. Earth Surface Processes and Landforms 18(6), pp. 519–525. doi: 10.1002/esp.3290180605.

Ustohal, P., Stauffer, F. and Dracos, T. 1998. Measurement and modeling of hydraulic characteristics of unsaturated porous media with mixed wettability. Journal of Contaminant Hydrology 33(1–2), pp. 5–37. Available at: https://linkinghub.elsevier.com/retrieve/pii/S0169772298000631.

Vanmarcke, E.H. 1977. Probabilistic Modeling of Soil Profiles. Journal of the Geotechnical Engineering Division 103(11), pp. 1227–1246. doi: 10.1061/AJGEB6.0000517.

Vervoort, R.W. and Cattle, S.R. 2003. Linking hydraulic conductivity and tortuosity parameters to pore space geometry and pore-size distribution. Journal of Hydrology

272(1–4), pp. 36–49. Available at: https://linkinghub.elsevier.com/retrieve/pii/S0022169402002536.

Wallach, R., Ben-Arie, O. and Graber, E.R. 2005. Soil Water Repellency Induced By Long-Term Irrigation with Treated Sewage Effluent. Journal of Environmental Quality 34(5), pp. 1910–1920. Available at: http://doi.wiley.com/10.2134/jeq2005.0073.

Wang, X., Li, Y., Wang, Y. and Liu, C. 2018. Performance of HYDRUS-1D for simulating water movement in water-repellent soils. Lupwayi, N. ed. Canadian Journal of Soil Science 98(3), pp. 407–420. Available at: http://www.nrcresearchpress.com/doi/10.1139/cjss-2017-0116.

Wang, Z. and Wallach, R. 2020. Effects of Time-Dependent Contact Angle on Wettability of Subcritically Water-Repellent Soils. Water Resources Research 56(10). Available at: https://onlinelibrary.wiley.com/doi/10.1029/2020WR027314.

Wohlgemuth, P.M., Hubbert, K.R. and Robichaud, P.R. 2001. The effects of log erosion barriers on post-fire hydrologic response and sediment yield in small forested watersheds, southern California. Hydrological Processes 15(15), pp. 3053–3066. doi: 10.1002/hyp.391.

Xiong, Y., Furman, A. and Wallach, R. 2012. Moment analysis description of wetting and redistribution plumes in wettable and water-repellent soils. Journal of Hydrology 422–423, pp. 30–42. Available at: https://linkinghub.elsevier.com/retrieve/pii/S0022169411008833.

Xiong, Y., Wallach, R. and Furman, A. 2011. Modeling multidimensional flow in wettable and water-repellent soils using artificial neural networks. Journal of Hydrology 410(1–2), pp. 92–104. Available at: https://linkinghub.elsevier.com/retrieve/pii/S0022169411006548.

Yang, B., Blackwell, P.S. and Nicholson, D.F. 1996. A numerical model of heat and water movement in furrow-sown water repellent sandy soils. Water Resources Research 32(10), pp. 3051–3061. Available at: http://doi.wiley.com/10.1029/96WR02103.

Zha, Y., Yang, J., Shi, L. and Song, X. 2013. Simulating One-Dimensional Unsaturated Flow in Heterogeneous Soils with Water Content-Based Richards Equation. Vadose Zone Journal 12(2), p. vzj2012.0109. doi: 10.2136/vzj2012.0109.

Zhang, X., Zhu, Y., Fang, C. and Chen, S. 2009. Numerical simulation of water-air two-phase flow in soil slope under water level rise condition. Wuhan University Journal of Natural Sciences 14(5), pp. 442–446. doi: 10.1007/s11859-009-0514-0.

Zhao, Y., Ren, C., Gong, J., Wang, J. and Li, H. 2020. Application of a water infiltration model for simulating water repellency of humus soil. Hydrological Processes 34(12), pp. 2793–2809. Available at: https://onlinelibrary.wiley.com/doi/10.1002/hyp.13764.

Zhu, J. and Mohanty, B.P. 2002. Spatial Averaging of van Genuchten Hydraulic Parameters for Steady-State Flow in Heterogeneous Soils: A Numerical Study. Vadose Zone Journal 1(2), pp. 261–272. doi: 10.2136/vzj2002.2610.

Chapter 3

Theoretical formulation

3.1 Introduction

This chapter presents two theoretical formulations that underpin the numerical research reported in this thesis, namely, the hydraulic behaviour of unsaturated soils, and the generation of Gaussian random fields through the solution of stochastic partial differential equations.

The theory of moisture transfer in unsaturated soils is based on the fully coupled model for heat, moisture and air flow developed by Thomas & Sansom (1995). This model is well established, and has seen further extension to represent mechanical and chemical processes (Thomas and He 1995; Cleall et al. 2007). Darcy's law is the underlying mechanism to describe the movement of the moisture phase over representative elementary volumes of the unsaturated medium. A significant limitation here is that the use of Darcy's law assumes the soil to be homogeneous and isotropic. As seen in the previous chapter, the effects of soil heterogeneity on flow processes are complex, and need to be modelled to simulate important characteristics of soil behaviour.

To account for this, Gaussian random fields are used to represent the spatially varying material parameters that soils exhibit. The theory is based on the work of Lindgren et al. (2011) and Roininen et al. (2014), where the random fields are generated by solving stochastic partial differential equations (SPDE). The approach is applicable to very large data sets ($>10^6$) because the sparsity of the matrices in the discretised PDE allow for extremely efficient treatment. By contrast, classical geostatistical methods often struggle to solve such problems (Vergara et al. 2018). For further discussion on the SPDE approach versus kernel-based methods, such as covariance matrix decomposition (Tang et al. 2020), see Simpson et al. (2012). Since the PDEs have the same structure as those of transport problem, the same FE framework may be used for their solution, thereby removing the need for potentially complex dual implementations (Jiang et al. 2022).

Section 3.2 presents the governing equations for moisture transfer in unsaturated soil where conservation of mass and Darcy's law are used to derive the governing equation in terms of the liquid pressure. Section 3.3 presents the derivation of the stochastic PDE relating to Gaussian field generation based on posing the Matérn autocorrelation function as a PDE with Fourier transform pairs.

3.2 Moisture transfer in unsaturated soils

The theoretical model is based on the approach of Cleall et al. (2007). The transport process for moisture in soil is dictated by two phases, liquid water and water vapour. Here, the influence of the gaseous phase is neglected, such that the volumetric water content θ is solely dependent on the liquid phase, such that

$$\theta = \theta_l \tag{3.1}$$

where θ_l is the volumetric liquid content. Similarly, the law of mass conservation is composed of mass conservation relating to the liquid phase alone, such that the following must hold true

$$\rho_l \frac{\partial \theta_l}{\partial t} = -\rho_l \boldsymbol{\nabla} \boldsymbol{v_l} - \rho_l E_{ss} \tag{3.2}$$

where t is time, ρ_l is the liquid density, E_{ss} is a sink/source term, and $\boldsymbol{v_l}$ is the liquid velocity. This then leads to the law of conservation of mass as

$$\rho_l \frac{\partial \theta_l}{\partial t} = -\rho_l \boldsymbol{\nabla} \boldsymbol{v_l}. \tag{3.3}$$

The volumetric liquid content can be formulated in terms of the degree of saturation as

$$\theta_l = nS_l \tag{3.4}$$

where n is the porosity and S_l is the degree of saturation of pore water. Upon substituting (3.4) into (3.3), this leads to

$$\frac{\partial (\rho_l n S_l)}{\partial t} + \rho_l \boldsymbol{\nabla} \boldsymbol{v_l} = 0. \tag{3.5}$$

From (3.5), it is seen that the movement of water is governed by liquid flux in the soil medium. Flow can be induced by various means such as thermal or chemical concentration gradients (Fredlund and Rahardjo 1993; Mitchell 1993); however, here flow is assumed to be driven by changes in pressure head. As such, the widely

adopted (Nielsen et al. 1986; Rosso et al. 2006; Hosseinejad et al. 2019) Darcy's law is employed (Darcy 1856). For multiphase flow in unsaturated soil, Darcy's law can be expressed as

$$v_l = -\frac{k_l}{\mu_l}\left[\nabla\left(\frac{u_l}{\gamma_l} + \nabla z\right)\right] = -K_l\left[\nabla\left(\frac{u_l}{\gamma_l} + \nabla z\right)\right] \quad (3.6)$$

where k_l is the effective permeability, μ_l is the absolute viscosity of pore liquid, γ_l is the unit weight of liquid, z is the elevation, K_l is the unsaturated hydraulic conductivity, and u_l is the liquid pressure and primary variable of the formulation.

A number of factors can influence the unsaturated hydraulic conductivity, such as void ratio, particle sizes and their distribution, degree of saturation, and turbulence of flow (Mitchell 1993). As the flow is assumed to be slow under Darcy's law, turbulent effects become negligible. Due to this, the unsaturated hydraulic conductivity is dependent on the degree of liquid saturation and void ratio (Fredlund 1981; Lloret and Alonso 1985), such that

$$K_l = K_l(e, S_l). \quad (3.7)$$

Initial values of void ratio and degree of saturation, as well as stress parameters, are known to influence the degree of saturation. The stress parameters -namely deviatoric stress and net stress- have been shown to be negligible in this context (Fredlund and Rahardjo 1993). Thus, given the control over the initial state of the soil mass, the degree of saturation can be expressed in term of soil suction as

$$S_l = S_l(s) \quad (3.8)$$

where s is the suction. Suction can be related to the primary variable u_l by

$$s = u_l - u_a, \quad (3.9)$$

where u_a is the pore air pressure, assumed atmospheric.

To reach the final governing differential equation for moisture transfer, the components of liquid flow need to be included in the mass conservation of water flow (3.5) and formulated in terms of the primary variable. By substituting (3.6) into (3.5), this results in

$$n\rho_l \frac{\partial S_l}{\partial t} + S_l\rho_l \frac{\partial n}{\partial t} - \frac{\rho_l}{\gamma_l}\nabla(K_l\nabla u_l) = \rho_l\nabla(K_l\nabla z). \quad (3.10)$$

By the chain rule, the time derivative of the degree of saturation can be reformulated in terms of the primary variable as

$$\frac{\partial S_l}{\partial t} = \frac{\partial S_l}{\partial s}\frac{\partial u_a}{\partial t} - \frac{\partial S_l}{\partial s}\frac{\partial u_l}{\partial t}, \tag{3.11}$$

and as u_a is assumed atmospheric, its time derivative vanishes. Similarly, the porosity n is assumed constant with time, such that its time derivative will vanish also. Thus, with substitution of the reduced (3.11) into (3.10), the governing differential equation for water transport in terms of the primary variable u_l is given as

$$C_{ll}\frac{\partial u_l}{\partial t} - \nabla(K_{ll}\nabla u_l) = J_l, \tag{3.12}$$

where

$$C_{ll} = -n\rho_l\frac{\partial S_l}{\partial s}, \tag{3.13}$$

$$K_{ll} = \frac{\rho_l K_l}{\gamma_l}, \tag{3.14}$$

$$J_l = \rho_l\nabla(K_l\nabla z). \tag{3.15}$$

By solving (3.12), the flow of moisture in soils can be represented in terms of its associated liquid pressure. A direct analytical solution to this is not necessarily straight-forward, so a numerical approach will be taken as detailed in the next chapter.

3.3 Gaussian random field generation

The underlying physical structure of the soil domain has not been considered in most previous studies. Ignoring this structure, in particular the intrinsic length scale of the domain, implies that certain aspects of behaviour -such as preferential flow- cannot be represented in an objective manner. This issue may be addressed by introducing a correlated structure to the field that is derived from a covariance kernel with a given correlation length. This length defines the size of region over which the field values (e.g. material properties) are correlated. Structurally, correlated random fields share a common form of soil material parameters (Liu and Leung 2018). For example, the conductivity at a given point in the soil mass should be similar in a nearby region of soil, where the size of said region is determined by the correlation length of the material parameter.

In the following, the theory used for generating correlated random fields is described. A particular advantage of the approach adopted is that the unknown field values ($\mathbf{X}$) (e.g. nodal values of the hydraulic conductivity) are determined by solving a system of partial differential equations that have the same general structure as those used to solve the transport problem. Depending on the boundary conditions applied in the formulation, the resulting discretised finite element matrix equation has the general form

$$(\mathbf{M} + l^2\mathbf{S})\mathbf{X} = \mathbf{R} \tag{3.16}$$

where the solution $\mathbf{X}$ is a Gaussian random field, $\mathbf{M}$ and $\mathbf{S}$ are the standard mass and stiffness matricies respectively (Zienkiewicz et al. 2013), l is the length-scale parameter determining the correlation length, and $\mathbf{R}$ is a combination of Gaussian noise and the mass matrix $\mathbf{M}$. This is the standard stochastic PDE formulation of the Matérn autocorrelation function. According to Stein (1999), the Matérn covariance function is a generalisation of several covariance functions due to its smoothness parameter. Stein (1999) also suggested that this function is more flexible when compared with other common autocorrelation functions employed in geostatistical analysis (see Li et al. (2015) for example functions). Its use can lead to more physically representative results when matching physical processes (Stein 1999), and has been shown to be suitable for representing soil material properties (Minasny and McBratney 2005).

The method of random field generation through solutions of SPDEs concerns Bayesian statistical inverse problems, where the probability distribution, often called a *prior*, of an unknown object X is estimated (Lindgren et al. 2011; Roininen et al. 2014). Here, a Gaussian random field $\mathbf{X} \in \mathbb{R}^{\mathrm{d}} \otimes \mathbb{S}$ is considered, where $\mathbb{S}$ is the stochastic space, and its contents are parameterised collections of Gaussian random variables $\{\mathbf{X}(\mathbf{x})\}_{\mathbf{x}\in\mathbb{R}^{\mathrm{d}}}$. An example of $\mathbf{X}$ generated through the SPDE approach is given in Figure 3.1, illustrating the correlated structure of the saturated conductivity for a soil layer of arbitrary size. A non-isotropic kernel was used such that the field is three times more correlated in the y axis, where the field was scaled to have a mean value of 7.1E-06 m/s with standard deviation of 2.3E-06 m/s.

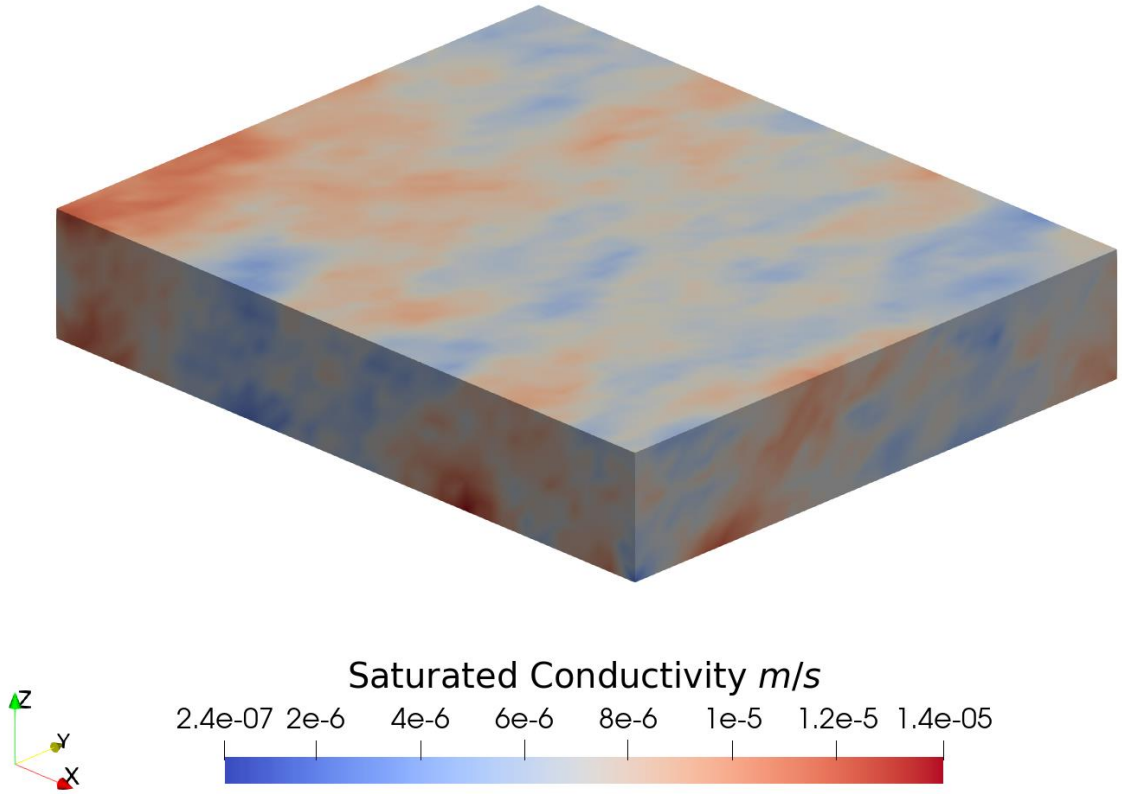

Figure 3.1: An example random field generated through the SPDE approach, representing the saturated conductivity of a soil layer of arbitrary size

Stationary random fields are considered, where the covariance of the field is a function of spatial distance alone, so that the correlation structure can be realised by the standard autocorrelation function form. Due to its smoothness, the Matérn autocorrelation function ($\mathrm{ACF}_{\mathbf{x}}(\mathbf{x})$) is adopted

$$\mathrm{ACF}_{\mathbf{x}}(\mathbf{x}) = \frac{2^{1-\nu}}{\Gamma(\nu)}\left(\frac{|\mathbf{x}|}{l}\right)^{\nu} K_{\nu}\left(\frac{|\mathbf{x}|}{l}\right) \tag{3.17}$$

for $\mathbf{x} \in \mathbb{R}^d$, where $\nu > 0$ is the smoothness parameter, $|\mathbf{x}|$ is the Euclidean distance, Γ is the gamma function, and K_{ν} is the Bessel function of the second kind of order ν (Rasmussen and Williams 2005). An important parameter $l > 0$ is the length-scale parameter for which $\delta = l\sqrt{8\nu}$ is the distance for correlations near 0.1 (Lindgren et al. 2011). Through l, the correlation length of the solution can be controlled. To avoid cumbersome matrix inversion, the prior covariance is approximated by posing the prior as a stochastic PDE.

This is achieved by forming the spectral density $S(\xi)$ as the Fourier transform pair of the autocorrelation function (Gihman and Skorokhod 2004), which gives the following spectral density

$$S(\xi) = \frac{2^d \pi^{\frac{d}{2}} \Gamma\left(\nu + \frac{d}{2}\right)}{\Gamma(\nu) l^{2\nu}} \left(\frac{1}{l^2} + |\xi|^2\right)^{-\left(\nu + \frac{d}{2}\right)}, \tag{3.18}$$

where $d = 1,2,3$, such that $S(\xi) = \widehat{\mathrm{ACF}_{\mathbf{X}}}(\mathbf{x})$ denotes the Fourier pair, where $\widehat{\mathrm{ACF}_{\mathbf{X}}}(\mathbf{x})$ is the Fourier transform of (3.17). Thus, $\mathbf{X}$ can be defined as

$$\mathbf{X} = \sigma\sqrt{S(\xi)}\mathbf{W}, \tag{3.19}$$

where σ is the standard deviation, and $\mathbf{W}$ is the white noise on $\mathbb{R}^d$, resulting in $\mathbf{X}$ being the Gaussian random field with correlation structure based on the Whittle-Matérn autocorrelation function. Finally, the stochastic PDE is attained after dividing (3.19) by $\sqrt{S(\xi)}$ and computing the inverse Fourier transform

$$(1 - l^2\Delta)^{\frac{(\nu + d/2)}{2}} \mathbf{X} = \sqrt{\varrho l^d}\mathbf{W} \tag{3.20}$$

where ϱ is a constant such that

$$\varrho \coloneqq \sigma^2 \frac{2^d \pi^{d/2} \Gamma(\nu + d/2)}{\Gamma(\nu)} \tag{3.21}$$

where $(1 - l^2\Delta)^{\frac{(\nu + d/2)}{2}}$ is a pseudo-differential operator defined by its Fourier transform. The smoothness parameter is now fixed such that $\nu = 2 - d/2$. Then, by defining the operator $\mathbf{H} \coloneqq \mathbf{I} - l^2\Delta$, where Δ is the Laplace operator, (3.20) becomes

$$\mathbf{H}\mathbf{X} = (\mathbf{I} - l^2\Delta)\mathbf{X} = \sqrt{\varrho l^d}\mathbf{W} \tag{3.22}$$

where $\mathbf{I}$ is the standard identity matrix.

3.4 Conclusion

The derivation of the governing equations to describe the characteristics of moisture transport in unsaturated soil have been presented. This approach is well established in coupled models and can closely match the soil behaviour observed in the field. Similarly, the derivation of the SPDE, which when solved results in a Gaussian random field, has been given. As the random field generation and moisture transport problems are formulated as PDEs, the same approach can be used for their solution.

In this way, the random fields will integrate seamlessly with the existing model architecture. Similarly, the mathematical formulation of the problem ensures that the correlation structure observed in the generated fields closely matches that of the autocorrelation function it is based on. This ensures that the material parameters represented by the random fields are similar in structure to those observed in the field.

In the next chapter, the numerical discretisation of both equations will be considered to allow for them to be solved numerically.

3.5 References

Cleall, P. J., Seetharam, S. C., & Thomas, H. R. (2007). Inclusion of Some Aspects of Chemical Behavior of Unsaturated Soil in Thermo/Hydro/Chemical/Mechanical Models. I: Model Development. Journal of Engineering Mechanics, 133(3), 338–347. https://doi.org/10.1061/(ASCE)0733-9399(2007)133:3(338)

Darcy, H. (1856). Les fontaines publiques de la vile de Dijon.

Fredlund, D. G. (1981). "Seepage in saturated soils. Panel Discussion : Ground water and seepage problems. Proc. 10th Int. Conf Soil Mech. Fdn. Engng, , 629–641.

Fredlund, D. G., & Rahardjo, H. (1993). Soil Mechanics for Unsaturated Soils. John Wiley & Sons, Inc. https://doi.org/10.1002/9780470172759

Gihman, I. I., & Skorokhod, A. V. (2004). The Theory of Stochastic Processes I. Springer Berlin Heidelberg. https://doi.org/10.1007/978-3-642-61943-4

Hosseinejad, F., Kalateh, F., & Mojtahedi, A. (2019). Numerical Investigation of liquefaction in earth dams: A Comparison of Darcy and Non-Darcy flow models. Computers and Geotechnics, 116. https://doi.org/10.1016/j.compgeo.2019.103182

Jiang, S. H., Huang, J., Griffiths, D. V., & Deng, Z. P. (2022). Advances in reliability and risk analyses of slopes in spatially variable soils: A state-of-the-art review. Computers and Geotechnics, 141. https://doi.org/10.1016/j.compgeo.2021.104498

Li, D.-Q., Jiang, S.-H., Cao, Z.-J., Zhou, W., Zhou, C.-B., & Zhang, L.-M. (2015). A multiple response-surface method for slope reliability analysis considering spatial variability of soil properties. Engineering Geology, 187, 60–72. https://doi.org/10.1016/j.enggeo.2014.12.003

Lindgren, F., Rue, H., & Lindström, J. (2011). An explicit link between Gaussian fields and Gaussian Markov random fields: the stochastic partial differential equation approach. In J. R. Statist. Soc. B (Vol. 73).

Liu, W. F., & Leung, Y. F. (2018). Characterising three-dimensional anisotropic spatial correlation of soil properties through in situ test results. Géotechnique, 68(9), 805–819. https://doi.org/10.1680/jgeot.16.P.336

Lloret, A., & Alonso, E. E. (1985). State surfaces for partially saturated soils. Proc. 11th Int. Conf. Soil Mech. Fdn. Engng, 557–562.

Minasny, B., & McBratney, Alex. B. (2005). The Matérn function as a general model for soil variograms. Geoderma, 128(3–4), 192–207. https://doi.org/10.1016/j.geoderma.2005.04.003

Mitchell, J. K. (1993). Fundamentals of Soil Behaviour. John Wiley.

Nielsen, D. R., Th. Van Genuchten, M., & Biggar, J. W. (1986). Water flow and solute transport processes in the unsaturated zone. Water Resources Research, 22(9S), 89S-108S. https://doi.org/10.1029/WR022i09Sp0089S

Rasmussen, C. E., & Williams, C. K. I. (2005). Gaussian Processes for Machine Learning. The MIT Press. https://doi.org/10.7551/mitpress/3206.001.0001

Roininen, L., Huttunen, J. M. J., & Lasanen, S. (2014). Whittle-matérn priors for Bayesian statistical inversion with applications in electrical impedance tomography. Inverse Problems and Imaging, 8(2), 561–586. https://doi.org/10.3934/ipi.2014.8.561

Rosso, R., Rulli, M. C., & Vannucchi, G. (2006). A physically based model for the hydrologic control on shallow landsliding. Water Resources Research, 42(6). https://doi.org/10.1029/2005WR004369

Simpson, D., Lindgren, F., & Rue, H. (2012). In order to make spatial statistics computationally feasible, we need to forget about the covariance function. Environmetrics, 23(1), 65–74. https://doi.org/10.1002/env.1137

Stein, M. L. (1999). Interpolation of Spatial Data. Springer New York. https://doi.org/10.1007/978-1-4612-1494-6

Tang, K., Wang, J., & Li, L. (2020). A prediction method based on Monte Carlo simulations for finite element analysis of soil medium considering spatial variability in soil parameters. Advances in Materials Science and Engineering, 2020. https://doi.org/10.1155/2020/7064640

Thomas, H. R., & He, Y. (1995). Analysis of coupled heat, moisture and air transfer in a deformable unsaturated soil. Géotechnique, 45(4), 677–689. https://doi.org/10.1680/geot.1995.45.4.677

Thomas, H. R., & Sansom, M. R. (1995). Fully Coupled Analysis of Heat, Moisture, and Air Transfer in Unsaturated Soil. Journal of Engineering Mechanics, 121(3), 392–405. https://doi.org/10.1061/(ASCE)0733-9399(1995)121:3(392)

Vergara, R. C., Allard, D., & Desassis, N. (2018). A general framework for SPDE-based stationary random fields. http://arxiv.org/abs/1806.04999

Zienkiewicz, O. C., Taylor, R. L., & Zhu, J. Z. (2013). The Finite Element Method: its Basis and Fundamentals. Elsevier. https://doi.org/10.1016/C2009-0-24909-9

Chapter 4

Numerical formulation

4.1 Introduction

Due to the complex nature of PDEs, the formulation of a direct analytical solution can be challenging. An alternative approach is the use of numerical approximation methods. Hence, due to the underlying complexity of the governing equations presented in Chapter three, this chapter presents their numerical solution through finite elements (FE). This approach is used widely in many areas of research and commercial codes for mechanics and transport based problems (Ghosh and Liu 1995; Stefanou 2009; Huang et al. 2014; Yi et al. 2020; Liu and Wang 2021; Pande et al. 2021), and has seen high levels of development since its conception. By using FE, the model is not restricted from potential future extensions to account for other mechanics based soil phenomena such as slope failure. Another key component is the existence of a well-established FE code base at Cardiff that could be used as a basis for developing the soil moisture and stochastic solution. Time stepping was achieved through an implicit Euler backward difference scheme. When compared with the classical forward method, this approach has been seen to be very numerically stable, and is able to find solutions where classical methods may struggle (Rapp 2017). It is also accurate due to the error level related to the governing equation being defined by a selected tolerance. An incremental-iterative solution of the non-linear problem was achieved using the Newton-Raphson approach, which is known for its accuracy and fast convergence to a given incremental solution (Sheng et al. 2002). If the problem poses strong non-linearities, the convergence of the iterative solution may not be guaranteed. To address this, many effective methods have been developed to improve the performance of the standard algorithm, as well as dealing with break down conditions (de Borst et al. 2012). See de Borst et al. (2012) and Potts & Zdravkovic (1999) for detailed reviews of incremental and iterative schemes.

Section 4.2.1 presents the spatial discretisation of the problem through finite elements, whereas the temporal discretisation is considered in section 4.2.2. Section

4.3 presents the problem formulation and discretisation for the matrix equivalent of the stochastic PDE seen in Section 3.3.

4.2 Moisture transfer in unsaturated soils

As stated, a numerical approach is employed to solve the governing PDE for moisture transport (3.12) from Chapter 3. Here, we use the finite element method for spatial discretisation of the problem, with an implicit Euler backward difference scheme for time discretisation. As the problem is highly non-linear, a standard Newton-Raphson procedure is implemented for incremental updating of the solution (Zienkiewicz et al. 2013).

4.2.1 Spatial discretisation

Here, the Galerkin weighted residual approach is employed (Zienkiewicz et al. 2013). The domain discretisation employed in the simulations presented in later chapters is that of three dimensional 8-noded hexahedral elements. This element was chosen due its ease of meshing and computational efficiency (Zhou et al. 2017; Shang et al. 2020; Karpik et al. 2023). Tetrahedral elements are also commonly used in FE codes due to their ability to adapt to complex domain geometries, but the higher accuracy of hexahedral elements allows for lower mesh density, and an overall increase in computational efficiency (Parrish et al. 2008; Schneider et al. 2022). Whilst the derivation could be presented generally for arbitrary elements, what follows conforms with the assumption of 3-D 8-noded hexahedral elements to keep with the wider narrative of the study.

The primary variable u_l and its derivatives can be approximated using the standard shape function approach

$$u_l \approx \widehat{u_l} = \sum_{s=1}^{n_e} N_s \widehat{u_{l_s}} \tag{4.1}$$

$$\nabla u_l \approx \nabla \widehat{u_l} = \sum_{s=1}^{n_e} (\nabla N_s) \widehat{u_{l_s}} \tag{4.2}$$

where the subscript s denotes the nodal values, N_s denotes the shape function, n_e is the number of nodes per element, and the symbol ^ denotes the approximate form. The governing equation (3.12) can be rewritten using the approximation (4.1), such that

$$-C_{ll} \frac{\partial \widehat{u_l}}{\partial t} + \nabla(K_{ll} \nabla \widehat{u_l}) + J_l = R_\Omega \tag{4.3}$$

where R_Ω is the residual error arising from the approximate form. The Galerkin weighted residual approach can be used to minimise the element-wise error by enforcing

$$\int_{\Omega^e} N\left(-C_{ll}\frac{\partial \widehat{u_l}}{\partial t}+\nabla(K_{ll}\nabla\widehat{u_l})+J_l\right)\mathrm{d}\Omega^e=0 \tag{4.4}$$

where Ω^e is the element domain, and $J_l=\rho_l\nabla(K_l\nabla z)$. The variational form can them be found by integration by parts of (4.4), such that

$$\int_{\Omega^e}\left\{\nabla(NK_{ll}\nabla\widehat{u_l})-K_{ll}\nabla\widehat{u_l}\nabla N+\nabla(N\rho_lK_l\nabla z)-K_l\rho_l\nabla z\nabla N-NC_{ll}\frac{\partial\widehat{u_l}}{\partial t}\right\}\mathrm{d}\Omega^e=0. \tag{4.5}$$

To reduce this further, the Gauss Divergence theorem is applied to reduce second order terms. For adjacent elements, the resulting surface integral will vanish, such that their contribution will exist only on the limit of the domain. Thus, (4.5) becomes

$$\int_{\Omega^e}\left\{-K_{ll}\nabla\widehat{u_l}\nabla N-K_l\rho_l\nabla z\nabla N-NC_{ll}\frac{\partial\widehat{u_l}}{\partial t}\right\}\mathrm{d}\Omega^e+\int_{\zeta^e}\{N(K_{ll}\nabla\widehat{u_l}+\rho_lK_l\nabla z)\mathbf{n}\}\mathrm{d}\zeta^e=0 \tag{4.6}$$

where ζ^e is the element boundary surface. Furthermore, introducing the derivative approximations (4.3) leads to

$$\int_{\Omega^\mathrm{e}}K_{ll}\,\nabla\mathbf{N}^T\nabla\mathbf{N}\,\mathrm{d}\Omega\boldsymbol{u_l}+\int_{\Omega^\mathrm{e}}C_{ll}\,\mathbf{N}^T\mathbf{N}\,\mathrm{d}\Omega^\mathrm{e}\frac{\partial\mathbf{u}_l}{\partial t}+\int_{\Omega^\mathrm{e}}K_l\,\rho_l\nabla\mathbf{N}^T\nabla z\,\mathrm{d}\Omega^\mathrm{e}-\int_{\zeta^\mathrm{e}}\mathbf{N}^T[\rho_l\widehat{\mathbf{v}_l}]\,\mathrm{d}\zeta^\mathrm{e}=0 \tag{4.7}$$

where $\mathbf{N}$ are the shape functions in matrix form, and $\widehat{\mathbf{v}_l}$ is the approximate liquid velocity normal to the boundary. This can be written compactly using matrix notation as

$$\mathbf{C}\frac{\partial\mathbf{u}_l}{\partial t}+\mathbf{K}\mathbf{u}_l=\mathbf{F} \tag{4.8}$$

where

$$\mathbf{C}=\sum_{e=1}^{n_e}\int_{\Omega^\mathrm{e}}C_{ll}\,\mathbf{N}^T\mathbf{N}\,\mathrm{d}\Omega^\mathrm{e} \tag{4.9}$$

$$\mathbf{K}=\sum_{e=1}^{n_e}\int_{\Omega^\mathrm{e}}K_{ll}\,\nabla\mathbf{N}^T\nabla\mathbf{N}\,\mathrm{d}\Omega \tag{4.10}$$

$$\mathbf{F}=\sum_{e=1}^{n_e}\int_{\Omega^\mathrm{e}}K_l\,\rho_l\nabla\mathbf{N}^T\nabla z\,\mathrm{d}\Omega^\mathrm{e}-\sum_{e=1}^{n_e}\int_{\zeta^\mathrm{e}}\mathbf{N}^T[\rho_l\widehat{\mathbf{v}_l}]\,\mathrm{d}\zeta^\mathrm{e} \tag{4.11}$$

Non-linearity is present in C_{ll}, K_{ll}, and K_l based on the constitutive laws required for their calculation. For example, to calculate the unsaturated conductivity K_l, non-

linear constitutive laws such as the van Genuchten-Mualem model are required (Mualem 1976), introducing non-linearity into the system. Similar constitutive laws are required for K_{ll} and C_{ll} based on the well-known van-Genuchten relation (van Genuchten 1980).

4.2.2 Temporal discretisation

As previously stated, an implicit Euler backward difference scheme is employed for time discretisation (Zienkiewicz et al. 2013), such that

$$\mathbf{K}\mathbf{u}_l^{t+1} + \frac{1}{\Delta t}\mathbf{C}(\mathbf{u}_l^{t+1} - \mathbf{u}_l^t) = \mathbf{F} \tag{4.12}$$

where t indicated the given time step. The standard Newton-Raphson procedure is applied to solve the non-linear equation, and is based on the first-order Taylor series expansion of the mass balance error (Chitez and Jefferson 2015). Similarly to Freeman et al. (2019), the primary variable vector is updated incrementally through an iterative process as

$$\delta\mathbf{u}_{l}{}_{k+1}^{t+1} = \left[\frac{\partial \boldsymbol{\Psi}}{\partial \mathbf{u}_{l}{}_{k}^{t+1}}\right]^{-1}(-\boldsymbol{\Psi}) \tag{4.13}$$

where k indicates the current increment, δ represents the incremental change in the primary variable vector, and $\boldsymbol{\Psi}$ is the approximate error, given by

$$\boldsymbol{\Psi} = \Delta t\mathbf{K}\mathbf{u}_l^{t+1} + \mathbf{C}(\mathbf{u}_l^{t+1} - \mathbf{u}_l^t) - \Delta t\mathbf{F}. \tag{4.14}$$

Once the solution vector is updated, tolerance checks are conducted based on a pre-defined convergence criterion. It may be the case that the solution does not converge within a given number of iterations, and if this is the case, then the simulation configuration would need to be re-assessed, possibly in terms of mesh or time-step refinement. Pseudo code for the solution algorithm is given below to highlight the process

Algorithm 1: Primary variable solution

Objective:

To solve for the primary variable u_l over a given time and within specified tolerance conditions.

Parameters:

- Initial arrays for storing results
- Total number of time steps *ntime*
- Maximum number of iterations *niter*
- Tolerance condition for convergence, taken as 0.01

Convergence Criterion:

Algorithm terminates for a time step when the tolerance between the norms of the solution is satisfied.

```
Initialise arrays
DO itime=1,ntime
    DO iiter=1,niter
        Calculate boundary flux
        Calculate error Ψ   (4.14)
        Solve for incremental primary variable δu_l   (4.13)
        Update primary variable vector u_l = u_l + δu_l
        IF tolerance condition satisfied THEN
            BREAK
        END IF
    END
    Update solution matrix
END
```

4.3 Gaussian random field generation

Previous work has been conducted by Roininen et al. (2014) to discretise the governing equation for stochastic PDE based random field generation for regular lattices. As a finite element approach is taken for the moisture transport problem, it is the natural approach for solving the random field generation problem.

In Chapter 3, $\mathbf{W}$ was considered white noise on $\mathbb{R}^d$, but is now considered to be a generalised random variable, i.e. a continuous linear mapping from the space of rapidly decreasing smooth functions $\mathcal{S}(\mathbb{R}^d)$ to square-integrable random variables. Hence, if $\mathbf{X}$ is a generalised random variable, then the duality pair $\langle \mathbf{X}, \boldsymbol{\phi} \rangle$ is a square integrable random variable for all $\boldsymbol{\phi} \in \mathcal{S}(\mathbb{R}^d)$, where:

$$\langle \mathbf{X}, \boldsymbol{\phi} \rangle = \int \mathbf{X}(\mathbf{x}) \boldsymbol{\phi}(\mathbf{x}) \, \mathrm{dx} \tag{4.15}$$

defines the inner product of smooth functions over the physical domain $\mathbb{R}^d$. By the definition of $\mathbf{W}$, for all $\boldsymbol{\phi}, \boldsymbol{\varphi} \in \mathcal{S}(\mathbb{R}^d)$, $\langle \mathbf{W}, \boldsymbol{\phi} \rangle$ is a Gaussian random variable such that

$$E\langle \mathbf{W}, \boldsymbol{\phi} \rangle = 0 \text{ and } E(\langle \mathbf{W}, \boldsymbol{\phi} \rangle, \langle \mathbf{W}, \boldsymbol{\varphi} \rangle) = \int \boldsymbol{\phi} \boldsymbol{\varphi} \, \mathrm{dx}, \tag{4.16}$$

completing the inner product in the physical and stochastic domain. Furthermore, $\mathbf{W}$ can be extended to be a linear function on $L^2(\mathbb{R}^d)$ (Lasanen 2002), suggesting that (3.19) can be reduced to: find $\mathbf{X}$ such that

$$\langle (\mathbf{I} - l^2 \Delta) \mathbf{X}, \boldsymbol{\phi} \rangle = \left\langle \sqrt{\varrho l^d} \mathbf{W}, \boldsymbol{\phi} \right\rangle = \left\langle \mathbf{W}, \sqrt{\varrho l^d} \right\rangle \tag{4.17}$$

for all $\boldsymbol{\phi} \in \mathcal{S}(\mathbb{R}^d)$.

For numerical implementation, the problem must be reduced to a bounded domain. Let $\Omega \subset \mathbb{R}^d$ be a bounded Lipshitz domain, then the problem becomes: find $\mathbf{X}$ on Ω such that equation (4.17) holds for all $C_0^\infty(\Omega)$. The solution to this is non-unique, so additional conditions need to be supplied to make the problem well-posed. The common boundary conditions (Dirichlet, Neumann and Robin respectively) are specified as

$$\mathbf{X}|_{\partial\Omega} = 0, \tag{4.18}$$

$$\frac{\partial \mathbf{X}}{\partial \mathbf{n}}|_{\partial\Omega} = 0, \tag{4.19}$$

$$\left(\mathbf{X} + \lambda \frac{\partial \mathbf{X}}{\partial \mathbf{n}}\right)|_{\partial\Omega} = 0, \tag{4.20}$$

where $\mathbf{n}$ is the unit normal to the boundary, and λ is a scalar value denoted as the Robin coefficient. By imposing these conditions, a change in the correlation properties of the field may be inferred, which is considered in the next section. It is now possible to derive a weak bilinear approximation of the problem; however, the

resulting fields may not lie within the defined problem space. It is with this in mind that finite element approximations are employed, such that

$$\mathbf{X} \approx \sum_{j=1}^{N} X_j \psi_j, \tag{4.21}$$

where ψ_j are the basis functions in $H^1(\Omega)$ (Sobolev space), and X_j are random variables.

Considering first the Neumann boundary condition (4.19) for X in (4.21), and by applying Green's first identity, the following equation may be derived

$$\langle (\mathbf{I} - l^2\Delta)\mathbf{X}, \boldsymbol{\phi} \rangle = \int_\Omega \mathbf{X}\boldsymbol{\phi} \mathrm{d}x + l^2 \int_\Omega \nabla \mathbf{X} \cdot \nabla \boldsymbol{\phi} \mathrm{d}x. \tag{4.22}$$

By following the usual Galerkin choice of $\phi = \psi_i$, the problem can now be approximated as

$$\text{find } \mathbf{X} \approx \sum_{j=1}^{N} X_j \psi_j \text{ such that } a(\mathbf{X}, \psi_i) = \left\langle \mathbf{W}, \sqrt{\varrho l^d}\psi_i \right\rangle \text{ for all } i = 1, \dots, N, \tag{4.23}$$

where a is a bilinear functional defined as

$$a(\boldsymbol{\varphi}, \boldsymbol{\phi}) = \int_\Omega \boldsymbol{\varphi}\boldsymbol{\phi} \mathrm{d}x + l^2 \int_\Omega \nabla \boldsymbol{\varphi} \cdot \nabla \boldsymbol{\phi} \mathrm{d}x, \quad \boldsymbol{\varphi}, \boldsymbol{\phi} \in H^1(\Omega). \tag{4.24}$$

Thus, (4.24) can be formulated as the matrix equation

$$\mathbf{H}\mathbf{X} = (\mathbf{M} + l^2\mathbf{S})\mathbf{X} = \mathbf{W}, \tag{4.25}$$

where $\mathbf{X} = \left(X_j\right)$ and the given matrices $\mathbf{M}$ and $\mathbf{S}$ and the vector $\mathbf{W}$ are

$$M_{i,j} = \int_\Omega \psi_j \psi_i \mathrm{d}x \tag{4.26}$$

$$S_{i,j} = \int_\Omega \nabla \psi_j \cdot \nabla \psi_i \mathrm{d}x \tag{4.27}$$

$$W_i = \left\langle W, \sqrt{\varrho l^d}\psi_i \right\rangle. \tag{4.28}$$

Dirichlet and Robin conditions may be considered in a similar fashion. For the Robin condition, after applying Green's theorem, the approximation becomes the bilinear form

$$b(\boldsymbol{\varphi}, \boldsymbol{\phi}) = a(\boldsymbol{\varphi}, \boldsymbol{\phi}) + \frac{l^2}{\lambda} \int_\zeta \boldsymbol{\varphi}\boldsymbol{\phi} \, \mathrm{d}\zeta, \ \boldsymbol{\varphi}, \boldsymbol{\phi} \in H^1(\Omega) \tag{4.29}$$

where $\zeta = \partial\Omega$, corresponding to the matrix equation

$$\mathbf{HX} = (\mathbf{M} + l^2\mathbf{S} + l^2/\lambda\mathbf{N})\mathbf{X} = \mathbf{W} \text{ where } N_{i,j} = \int_\zeta \psi_j \psi_i \, \mathrm{d}\zeta. \quad (4.30)$$

For the Dirichlet condition, choosing the function space to be $H_0^1(\Omega)$ and applying Green's theorem results in the same expression as (4.22), and so the problem can be formulated as seen in the matrix equation (4.25).

Solving either equation (4.25) or (4.29) will result in a random field with correlated properties that could, for example, be utilised in numerical solution routines for physical representation of initial conditions or material properties. Pseudo code for the solution algorithm is given below to highlight the process

Algorithm 2: Random field generation through SPDE

Objective:
To generate a random field $\mathbf{X}$ by solving the stochastic partial differential equation given by Eqn (4.30).
Parameters:
- Initial arrays for storing intermediate results and $\mathbf{X}$
- Random seed for generating stochastic processes
- LHS (Left Hand Side) and RHS (Right Hand Side) of Eqn (4.30)

Initialise arrays
Set random seed
Assemble LHS of (4.30)
Compute Cholesky decomposition of $\mathbf{M}$
Generate random array W based on a normal distribution
Compute RHS of (4.30)
Solve (4.30) for $\mathbf{X}$

Following this procedure, the random field $\mathbf{X}$ can be scaled to represent a given parameter used in the wider solution process.

4.4 Conclusion

The approximate solution of the governing equations for moisture transfer and Gaussian random field generation have been derived through the finite element method for spatial discretisation. By using this method, future development of the model is not impeded by the physical processes that can be represented, such as

mechanical or chemical. Similarly, the FE architecture employed could be modified to allow for more advanced approaches, such as unfitted methods. By also using FE for the solution of the random field problem, the model architecture does not need to be reinvented, and similar solution processes can be carried out as in the moisture transport stage. Many of the matrices present in equation (4.30) are equivalent to those seen in equation (4.8), such as the classical stiffness and storage matrix. The main advantage is that the random fields are solved using an identical mesh (elements and nodes) to that used for the solution of the moisture transfer problem, so their nodal and element values can easily be included in the constitutive components of equation (4.8) without the need for complex mapping rules. The random field generation is a stationary solution, but time discretisation was necessary for the moisture transport processes, and was achieved though and implicit Euler backwards difference scheme. Whilst the modelling of moisture transfer in heterogeneous soil is a highly non-linear problem, the Newton-Raphson approach works effectively under these tight constraints, as will be seen in later chapters.

4.5 References

Chitez, A. S., & Jefferson, A. D. (2015). Porosity development in a thermo-hygral finite element model for cementitious materials. Cement and Concrete Research, 78, 216–233. https://doi.org/10.1016/j.cemconres.2015.07.010

de Borst, R., Crisfield, M. A., Remmers, J. J. C., & Verhoosel, C. V. (2012). Non-Linear Finite Element Analysis of Solids and Structures. Wiley. https://doi.org/10.1002/9781118375938

Freeman, B. L., Cleall, P. J., & Jefferson, A. D. (2019). An indicator-based problem reduction scheme for coupled reactive transport models. International Journal for Numerical Methods in Engineering, 120(13), 1428–1455. https://doi.org/10.1002/nme.6186

Ghosh, S., & Liu, Y. (1995). Voronoi cell finite element model based on micropolar theory of thermoelasticity for heterogeneous materials. International Journal for Numerical Methods in Engineering, 38(8), 1361–1398. https://doi.org/10.1002/nme.1620380808

Huang, J., Chen, M., & Sun, J. (2014). Mesoscopic characterization and modeling of microcracking in cementitious materials by the extended finite element method. Theoretical and Applied Mechanics Letters, 4(4), 041001. https://doi.org/10.1063/2.1404101

Karpik, A., Cosco, F., & Mundo, D. (2023). Higher-Order Hexahedral Finite Elements for Structural Dynamics: A Comparative Review. Machines, 11(3), 326. https://doi.org/10.3390/machines11030326

Lasanen, S. (2002). Discretizations of Generalized Random Variables with Applications to Inverse Problems.

Liu, X., & Wang, Y. (2021). Probabilistic simulation of entire process of rainfall-induced landslides using random finite element and material point methods with hydro-mechanical coupling. Computers and Geotechnics, 132. https://doi.org/10.1016/j.compgeo.2020.103989

Pande, S., Papadopoulos, P., & Babuška, I. (2021). A cut-cell finite element method for Poisson's equation on arbitrary planar domains. Computer Methods in Applied Mechanics and Engineering, 383. https://doi.org/10.1016/j.cma.2021.113875

Parrish, M., Borden, M., Staten, M., & Benzley, S. (2008). A Selective Approach to Conformal Refinement of Unstructured Hexahedral Finite Element Meshes. In Proceedings of the 16th International Meshing Roundtable (pp. 251–268). Springer Berlin Heidelberg. https://doi.org/10.1007/978-3-540-75103-8_15

Potts, D. M., & Zdravkovic, L. (1999). Finite Element Analysis in Geotechnical Engineering: Volume One - Theory. Thomas Telford Ltd. https://doi.org/10.1680/feaiget.27534

Rapp, B. E. (2017). Numerical Methods for Solving Differential Equations. In Microfluidics: Modelling, Mechanics and Mathematics (pp. 549–593). Elsevier. https://doi.org/10.1016/B978-1-4557-3141-1.50027-7

Roininen, L., Huttunen, J. M. J., & Lasanen, S. (2014). Whittle-matérn priors for Bayesian statistical inversion with applications in electrical impedance tomography. Inverse Problems and Imaging, 8(2), 561–586. https://doi.org/10.3934/ipi.2014.8.561

Schneider, T., Hu, Y., Gao, X., Dumas, J., Zorin, D., & Panozzo, D. (2022). A Large-Scale Comparison of Tetrahedral and Hexahedral Elements for Solving Elliptic PDEs with the Finite Element Method. ACM Transactions on Graphics, 41(3), 1–14. https://doi.org/10.1145/3508372

Shang, Y., Li, C., & Jia, K. (2020). 8-node hexahedral unsymmetric element with rotation degrees of freedom for modified couple stress elasticity. International Journal for Numerical Methods in Engineering, 121(12), 2683–2700. https://doi.org/10.1002/nme.6325

Sheng, D., Sloan, S. W., & Abbo, A. J. (2002). An Automatic Newton-Raphson Scheme. International Journal of Geomechanics, 2(4), 471–502. https://doi.org/10.1061/(ASCE)1532-3641(2002)2:4(471)

Stefanou, G. (2009). The stochastic finite element method: Past, present and future. In Computer Methods in Applied Mechanics and Engineering (Vol. 198, Issues 9–12, pp. 1031–1051). https://doi.org/10.1016/j.cma.2008.11.007

Yi, J. T., Huang, L. Y., Li, D. Q., & Liu, Y. (2020). A large-deformation random finite-element study: failure mechanism and bearing capacity of spudcan in a spatially varying clayey seabed. Géotechnique, 70(5), 392–405. https://doi.org/10.1680/jgeot.18.P.171

Zhou, P.-L., Cen, S., Huang, J.-B., Li, C.-F., & Zhang, Q. (2017). An unsymmetric 8-node hexahedral element with high distortion tolerance. International Journal for Numerical Methods in Engineering, 109(8), 1130–1158. https://doi.org/10.1002/nme.5318

Zienkiewicz, O. C., Taylor, R. L., & Zhu, J. Z. (2013). The Finite Element Method: its Basis and Fundamentals. Elsevier. https://doi.org/10.1016/C2009-0-24909-9

Chapter 5

Near-boundary error reduction in stochastic PDE based Gaussian random field generators

5.1 Introduction

As seen in Chapter 4, to be able to generate random fields numerically, the problem domain must be reduced to a bounded domain, often requiring boundary conditions that are not generally known (Khristenko et al. 2019). The standard Dirichlet, Neumann, and Robin conditions are commonly applied, where each comes with its respective method of error reduction in the near-boundary region $\Omega_B \subseteq \Omega$ (see Figure 5.1 (c)). More formally, this is defined as the near-boundary region which includes all points that are at a distance of less than or equal to the length-scale parameter l from $\partial\Omega$. As l grows, the approximation of the autocorrelation function (ACF) inherent to the field structure breaks down in Ω_B due to its increasing size relative to Ω. When implementing the stochastic PDE approach, it is advisable to minimise Ω_B in relation to Ω to avoid heavily constraining the problem.

The following will present the current mitigation strategies for reducing the near-boundary error, depending on the boundary condition applied, as well as a new approach which is shown in the present study to be systematically more flexible in reducing said error. This alternative approach is presented for reducing spurious values in the near-boundary region through a weighted Dirichlet-Neumann (D-N) boundary condition. Two variants of the condition are proposed based upon adopting different dependencies to define the Neumann coefficient used. The proposed conditions are both dependent on a weighting parameter α that controls the ratio of Dirichlet to Neumann components applied to the boundary, with the second also containing a dependency based on l. Through a detailed parametric investigation, optimal values of α are found based on the length-scale parameter l. To allow for comparison between the two weighted D-N approaches, the homogeneous Neumann boundary condition, with and without domain extension, and the Robin

boundary condition with Robin coefficient $\lambda = 1.42l$ are also applied. The error reduction at the boundary based on the applied condition is then evaluated through computing the covariance functions of the corresponding generated fields, and compared with the true ACF. Finally, a relation between α and l is proposed to generalise the condition, allowing for simpler application when considering other problems.

Section 5.2 considers methods to mitigate boundary error when employing a given boundary condition, Section 5.3 presents the weighted Dirichlet-Neumann boundary condition and shows the processes of its testing, and Section 5.4 concludes on the investigation.

5.2 Existing methods in near-boundary error mitigation

5.2.1 Extended domain

The application of both Dirichlet and Neumann boundary conditions result in the same matrix equation (4.25). In this way, the strategy for error reduction is applicable for both applied conditions. Similarly, both conditions are independent of components that can be tuned, so the use of numerical techniques is necessary.

One approach involves computing the random field over an extended domain - denoted Ω_{EXT}- such that the desired problem domain Ω sits within it, and can be extracted. By extending the domain, the error in the near-boundary is moved from the near-boundary of Ω, to that of the extending domain Ω_{EXT}. This will ensure the correlation structure of Ω more closely matches the assumed structure of the autocorrelation function, being of Matérn form. Figure 5.1 (a-b) shows two schematics of this process in both two and three dimensions.

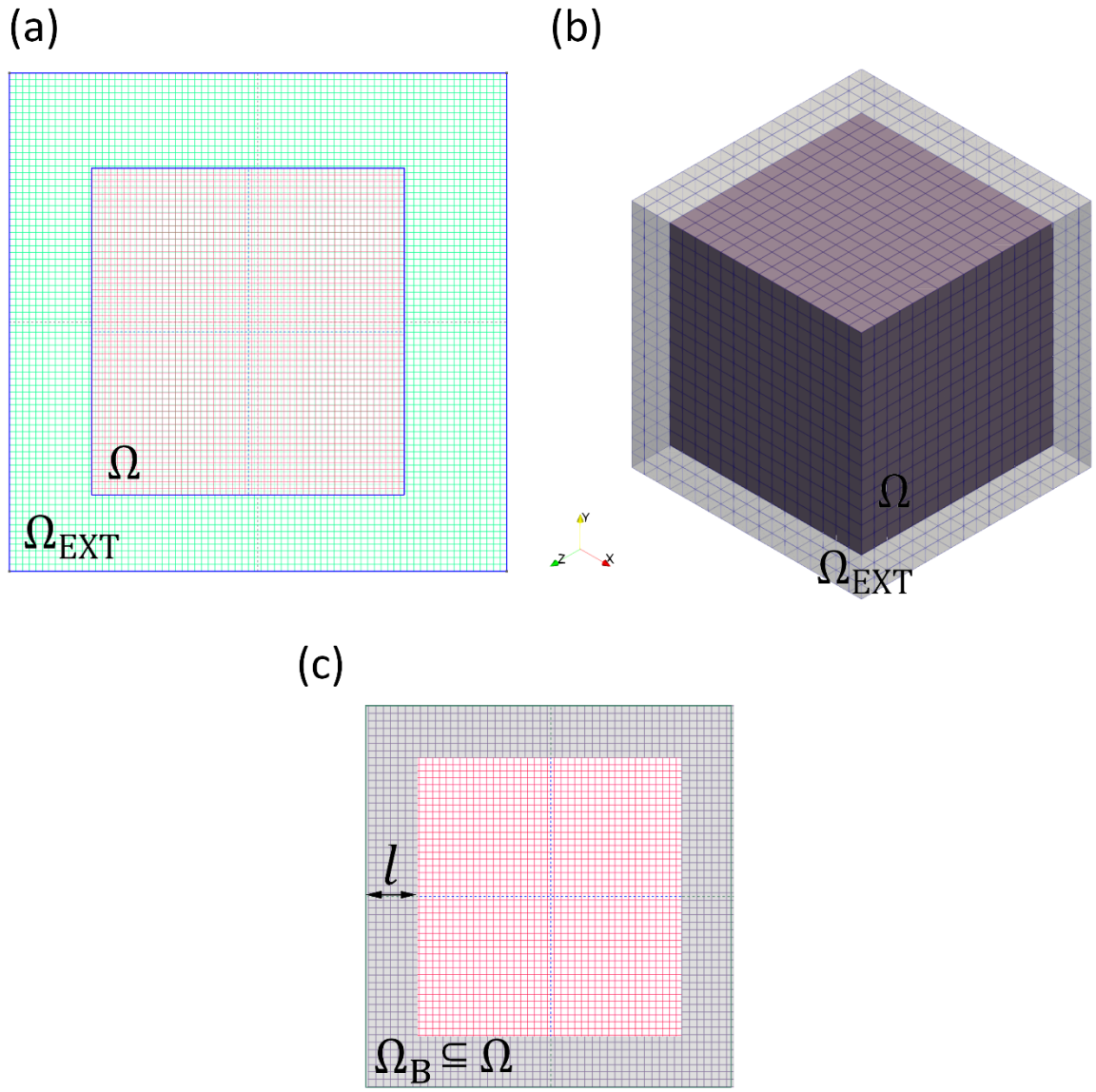

Figure 5.1: Domain extension schematics for: (a) the 2-D case, (b) the 3-D case, where both Ω_{EXT} and Ω are labelled for each dimension, and (c) an illustration of Ω_B in 2-D

Clearly the extension of the domain in this manner increases the computational cost of computing the solution, this issue being more critical in 3-D than 2-D. However, this does depend on how fine the discretisation is across Ω. The number of random variables used to represent the field is equal to the number of nodes, so an extension of the domain could increase this significantly. An alternative could be to use a coarser mesh in the extended region of Ω_{EXT}, since capturing a more accurate solution here is unnecessary as it will be neglected after solving. Another question that is raised is the amount that the domain must be extended such that the error is

eliminated in all Ω. As Ω_B is dependent on the length-scale parameter of the field l, an extension of at least l away from the boundary will leave no intersection between Ω and Ω_B due to their definition. Of course, this depends on the domain geometry, and in some cases, an extension of less than l would also be sufficient in reducing the error.

5.2.2 Robin boundary condition

Clearly, computing a solution directly over Ω rather than an extended domain would reduce the computational cost, and neglect the need to implement numerical routines to consider multiple domains. This can be done by using the Robin boundary condition (4.20), which depends on the Robin coefficient λ (see also equation 5.1 below), and can be interpreted as a tuning parameter for the correlated structure in Ω_B. As such, the use of an extended computational domain is not strictly necessary when applying this condition. The choice of λ, however, is not well understood. Roininen et al. (2014) suggested that $\lambda = 1.42l$ results in an adequate fit to the correlation structure. This choice of λ was not shown to be established in a rigorous way as it was deemed out of the scope of the study (Roininen et al. 2014), suggesting the need for further investigation to verify the condition. It was also suggested that λ should vary as a function of the boundary, which was later considered by Daon and Stadler (2018) who utilised a spatially varying Robin coefficient to provide domain Green's functions that are close to the free-space Green's functions of the Matérn covariance function. Other approaches have also been taken, such as the use of a partial Dirichlet-to-Neumann operator on the extended boundary (Calvetti et al. 2015a).

5.3 Weighted Dirichlet-Neumann boundary condition

5.3.1 Theory

Here, two alternative coefficients λ_1, λ_2 are proposed by formulating the Robin condition in equation (4.20) as a weighted boundary condition between the Dirichlet and Neumann components, denoted as the weighted Dirichlet-Neumann (D-N) condition. The conditions will depend on the weighting parameter $\alpha \in [0,1]$ which controls the ratio of the Dirichlet and Neumann components.

First consider λ_1, where the weighted D-N condition is

$$\left(\alpha X + (1-\alpha)\frac{\partial X}{\partial \mathbf{n}}\right) = R_\gamma \text{ on } \partial\Omega. \quad (5.1)$$

Here, R_γ is assumed zero, such that

$$\left(\alpha X + (1-\alpha)\frac{\partial X}{\partial \mathbf{n}}\right) = 0 \text{ on } \partial\Omega. \quad (5.2)$$

It is possible that a non-zero value would provide a meaningful boundary conditions, but this is not further investigated. Taking equation (5.2) in the standard form of equation (4.20), it can be seen that

$$\lambda = \lambda_1(\alpha) = \frac{1-\alpha}{\alpha}. \quad (5.3)$$

Similarly, when considering λ_2, the given boundary condition is

$$\left(\alpha X + (1-\alpha) l \frac{\partial X}{\partial \mathbf{n}}\right) = 0 \text{ on } \partial\Omega, \quad (5.4)$$

where in this case

$$\lambda = \lambda_2(\alpha, l) = \frac{1-\alpha}{\alpha} l. \quad (5.5)$$

Both (5.2) and (5.4) are functionally the same as the Robin condition, where in this case, α can be used to tune the influence of its components. The inclusion of l in equation (5.5) follows the functional dependency of the proposed Robin coefficient in Roininen et al. (2014), and whilst similar to equation (5.3), the additional dependence will result in a different optimal range when tuning α to reduce errors in the near-boundary region. Equations (5.2) and (5.4) can be applied by simply exchanging the expression for λ in the approximate matrix equation (4.30) to that of λ_1 or λ_2. To illustrate the effects of changing α, random fields were generated by solving equation (4.30) after applying equation (5.4) for a 1 m cube consisting of hexahedral elements with $l = 0.2$ m. Figure 5.2 shows a partition of the resulting fields generated over a cube for (a) $\alpha = 0$, (b) $\alpha = 0.5$, (c) $\alpha \to 1$, and (d) the result of implementing the standard Neumann boundary condition where the fields are scaled to have zero mean and a standard deviation of 1.

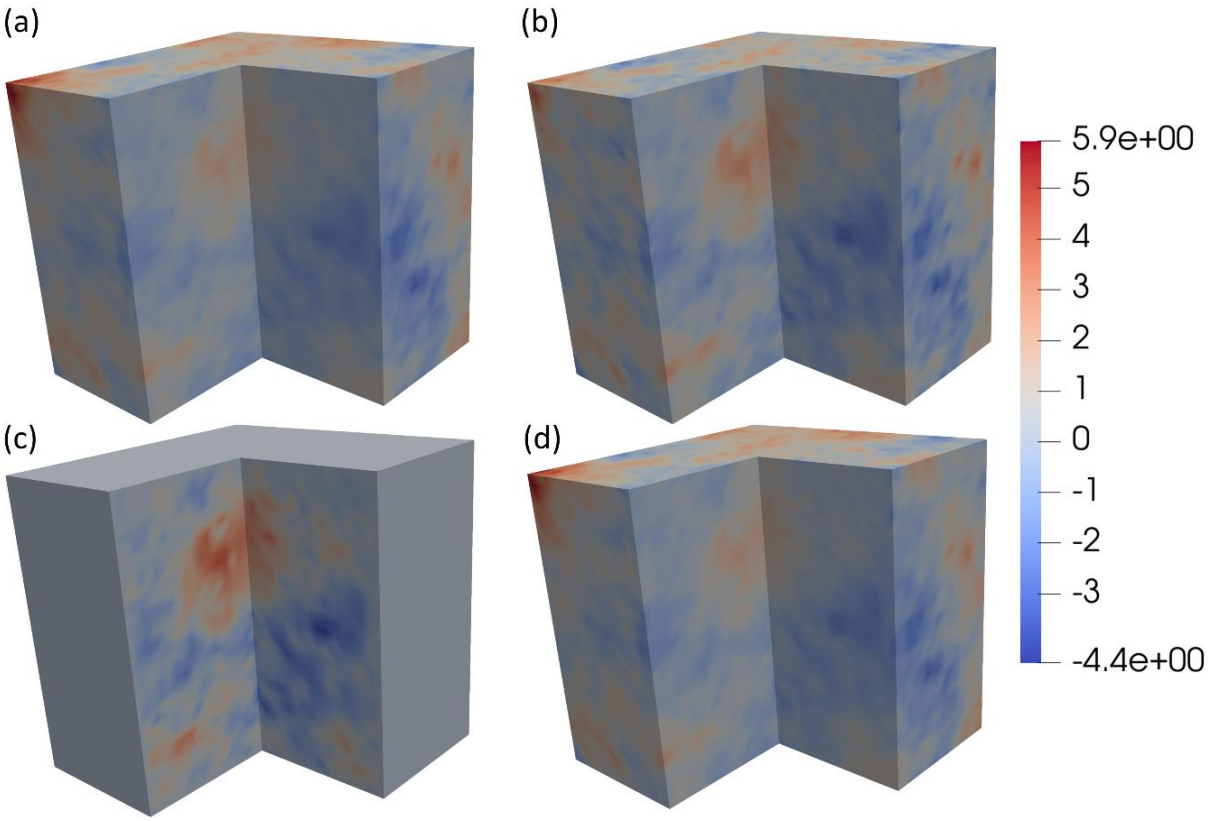

Figure 5.2: Differing correlation structures of a general spatially varying parameter based on the weighted D-N boundary condition for changing α *where (a)* $\alpha = 0$*, (b)* $\alpha = 0.5$*, (c)* $\alpha \to 1$ *, and (d) the result of applying the standard Neumann condition (scaled to zero mean and standard deviation of 1)*

As $\alpha \to 1$, the Neumann component of equation (5.4) tends to zero, relating to a fixed (Dirichlet) condition on all boundaries as seen in Figure 5.2 (c). On the other hand, when $\alpha = 0$, the Dirichlet component is removed, leading to the resulting field matching the corelation structure of the pure Neumann enforcement (see Figure 5.2 (a) and (d)). It can also be seen in (a) and (d) that variability within the domain is more diffuse than the variation over the boundary. This is commonly observed when considering Neumann boundary conditions. The converse is apparent in Figure 5.2 (c), as $\alpha \to 1$, with no variability over the boundary and more pronounced structures within the domain. Figure 5.2 (b) is the generated field for $\alpha = 0.5$, highlighting that combing the components of both conditions can lead to correlation structures that are more consistent with those expected over the whole domain (this is more explicitly quantified in the following sections). Whilst $\alpha = 0.5$ may not be the optimal value of α for this particular length-scale l, there is a distinct change in the correlation

structure in the near-boundary which appears to be more coherent with that observed over the full domain.

5.3.2 Testing Procedure

To determine the relationship between the optimised value of α and l for λ_1 and λ_2, a detailed parametric testing regime was devised to find the optimal value of α for a given range of l. Here, l is in relative terms, where $l = 0.1$ would relate to a length-scale parameter of 10% of the domain length. The fields were generated for values of $l = 0.1$, 0.15, 0.2, 0.25, 0.3, 0.35, and 0.4. For each l, α is varied from 0 to near 1 in increments of 0.1, with 10 realisations being generated at each α to allow for the average covariance function for each α to be calculated and compared with the true ACF equation (3.17). The average is taken since multiple realisations are often required to achieve objective results for a given quantity of interest when conducting stochastic analyses. Once the optimal value of α is found for this level of precision, the search is continued between the two best choices of α for each l. Here, the maximal value of l is taken as 0.4. When applying spatial variation using Gaussian random fields in numerical models, it is unlikely that larger values will be used due to resulting low levels of variation across the domain defeating the purpose of imposing variability in the system. It is more likely to be at most 0.3 in relative terms. Similarly, due to the break down in the formulation, taking l larger than 0.4 will not give a reasonable approximation of the desired correlation structure for all boundary conditions considered. As l approaches 0.4, the domain is largely composed of Ω_{B}, so the error associated with the near-boundary will manifest throughout all of Ω.

In order to compare the generated field structures with equation (3.17), the semivariogram of each field is computed. The semivariogram is used to measure the level of spatial continuity for a given domain, these being most commonly applied in the area of geostatistics (Zhao and Wall 2004; Bachmaier and Backes 2011). It can be calculated as half the average squared difference of values separated by a location vector, such that

$$\gamma(h) = \frac{1}{2N(h)} \sum_{\mathrm{i}=1}^{N(h)} \big(z(\mathbf{u}_i) - z(\mathbf{u}_i + h)\big)^2, \tag{5.6}$$

where h is the lag distance, $N(h)$ is the number of pairs of points in Ω of separation h, $\mathbf{u}$ is the location vector, and $z(\mathbf{u})$ is the value in the domain at the vector $\mathbf{u}$. Figure

5.3 shows a schematic of the semivariogram, where the range can be thought of as the correlation length or distance for which points become uncorrelated, the sill is the total variance of the data, and the nugget describes the small-scale variability of the data (which could be attributed to measurement error in some cases).

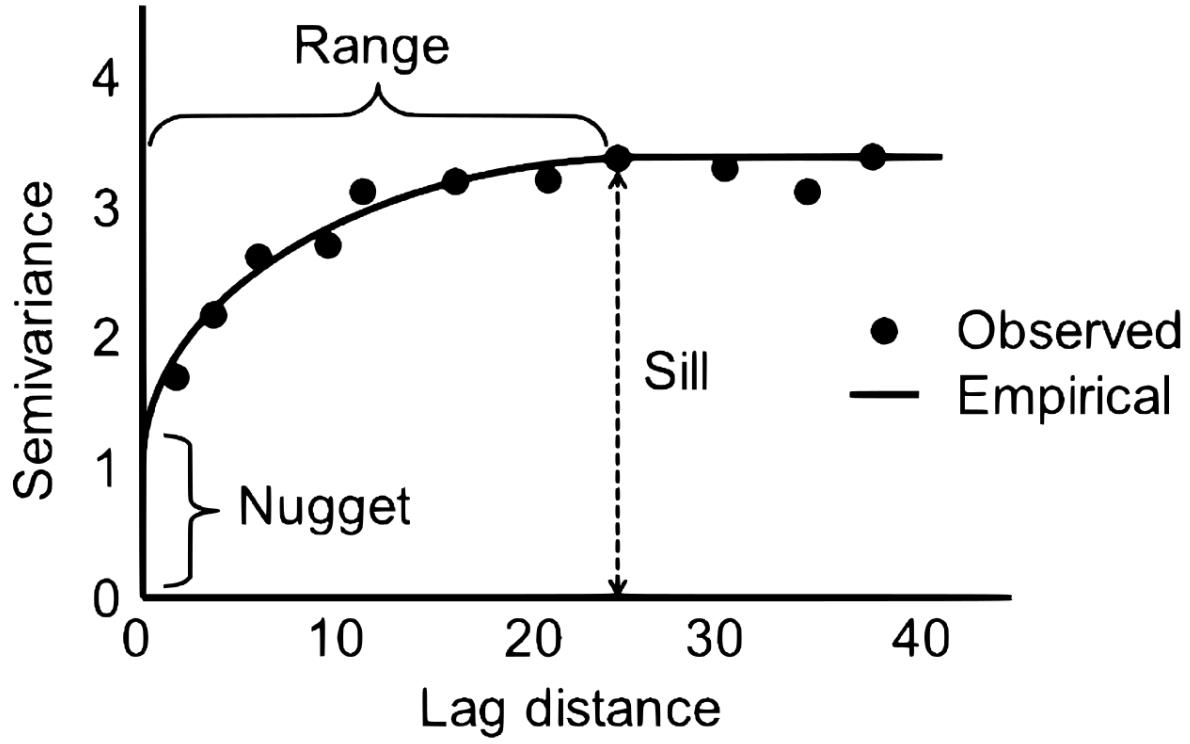

Figure 5.3: Schematic of a semivariogram calculated based on empirical data (after Biswas & Cheng (2013)*)*

The covariance function and semivariogram are directly related by

$$C(h) = \sigma - \gamma(\mathrm{h}), \tag{5.7}$$

where σ is the standard deviation of the field values. In this way, we can compute the covariance function of each field, averaging the individual covariance functions over the 10 realisations for each choice of α, and compare this with equation (3.17) to determine an optimal value of α.

The standard Neumann and Robin conditions, with $\lambda = 1.42l$, are also given the same treatment, with 10 realisations being generated for each l. In doing so, the optimal choice of boundary condition can be evaluated, and further insight to the choice of $\lambda = 1.42l$ can be used to determine its suitability in matching the true covariance function equation (3.17). Furthermore, use of an extended domain, Ω_{EXT}

with a Neumann condition is also considered (denoted as Neumann-Extended) again with 10 realisations being generated for each l.

5.3.3 Results

In this section, results relating to the application of the following boundary conditions are presented: Neumann, Neumann-Extended, Robin with $\lambda = 1.42l$, weighted D-N with $\lambda = \lambda_1$, and weighted D-N with $\lambda = \lambda_2$. The covariance functions are computed over the full domain Ω, as well as the near-boundary region as a means of comparison. The computational domain of the standard case (Ω) is a 1 m cube sub-domain of Ω_{EXT} , aligned concentrically, consisting of 29791 nodes discretised with 27000 elements, where Ω_{EXT} is a 1.5 m cube consisting of 97336 nodes discretised into 91125 8-noded hexahedral elements. For both domains, the relative element length is 0.03333. Once the field has been generated over Ω_{EXT}, the 1 m cube internal domain Ω is extracted and used to compare with the other methods whose fields are generated directly over Ω. The computational domains can be seen in Figure 5.4, being Ω (a) and Ω_{EXT} (b).

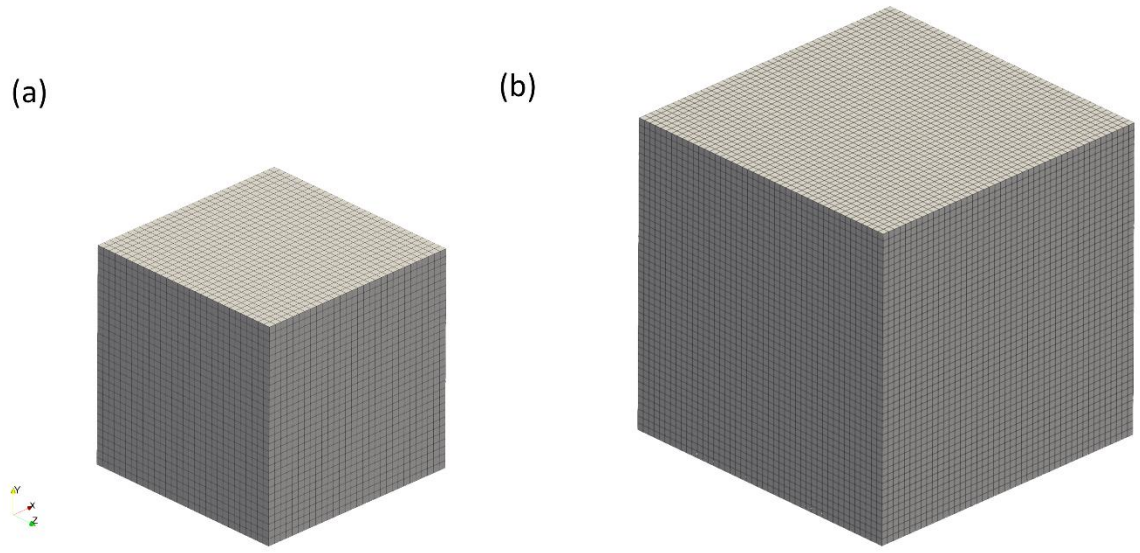

Figure 5.4: The computational domains used for field generation, being: (a) Ω, a 1 m cube with 29791 nodes, and (b) Ω_{EXT}, a 1.5 m cube with 97336 nodes

It is worth noting that the strongly enforced Dirichlet boundary condition is neglected here, as upon its enforcement the variation on the boundary will vanish (as in Figure 5.2 (c)), defeating the purpose of having a random field to represent variable spatial continuity. It could be argued that the domain extension principle should be applied

in this case, but doing so would lead to an identical field as that of the Neumann-Extended condition, and so it has not been considered.

Figure 5.5 shows the range of average covariance functions obtained when applying the weighted D-N boundary condition with $\lambda = \lambda_1$ for α from 0 to near 1 with increasing correlation length (a-d) over Ω. In (a-d), the maximum and minimum alpha will define the range over which the correlation values lie for linearly increasing α, and are compared against the ACF equation (3.17).

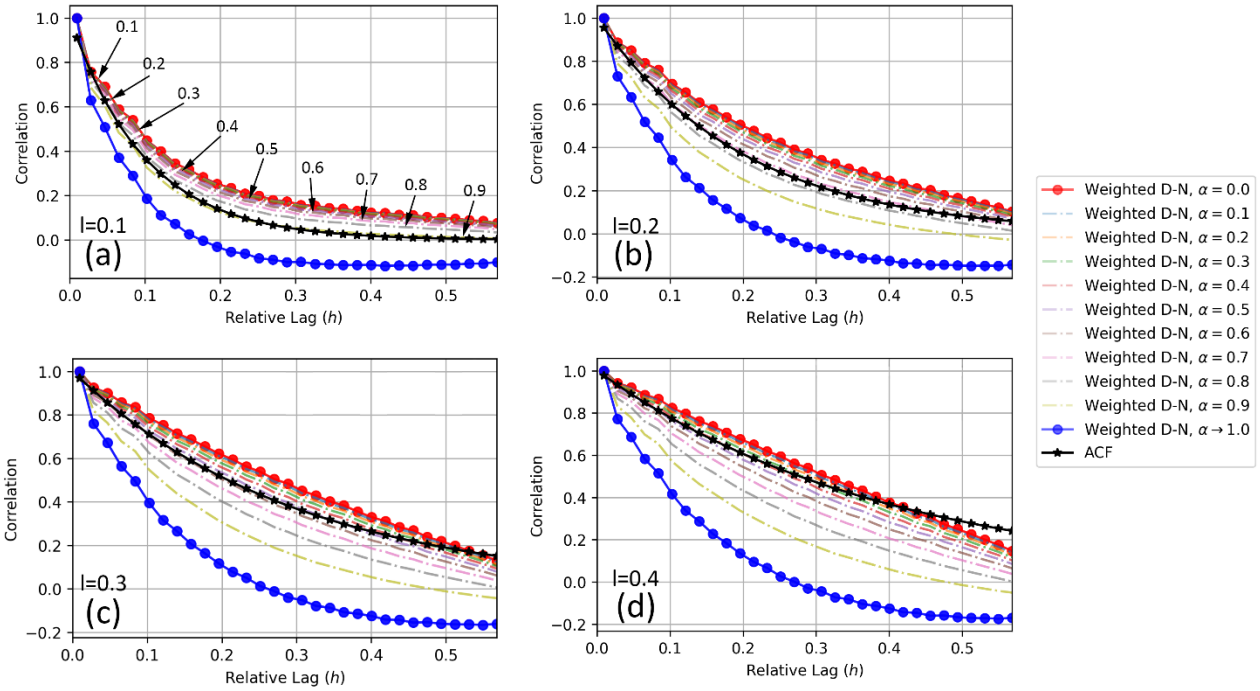

Figure 5.5: Average covariance functions over Ω for weighted D-N with $\lambda = \lambda_1$ for full range of α for l equal: (a) 0.1, (b) 0.2, (c) 0.3, and (d) 0.4

The covariance functions over Ω can also be visualised when considering $\lambda = \lambda_2$, and is shown in Figure 5.6.

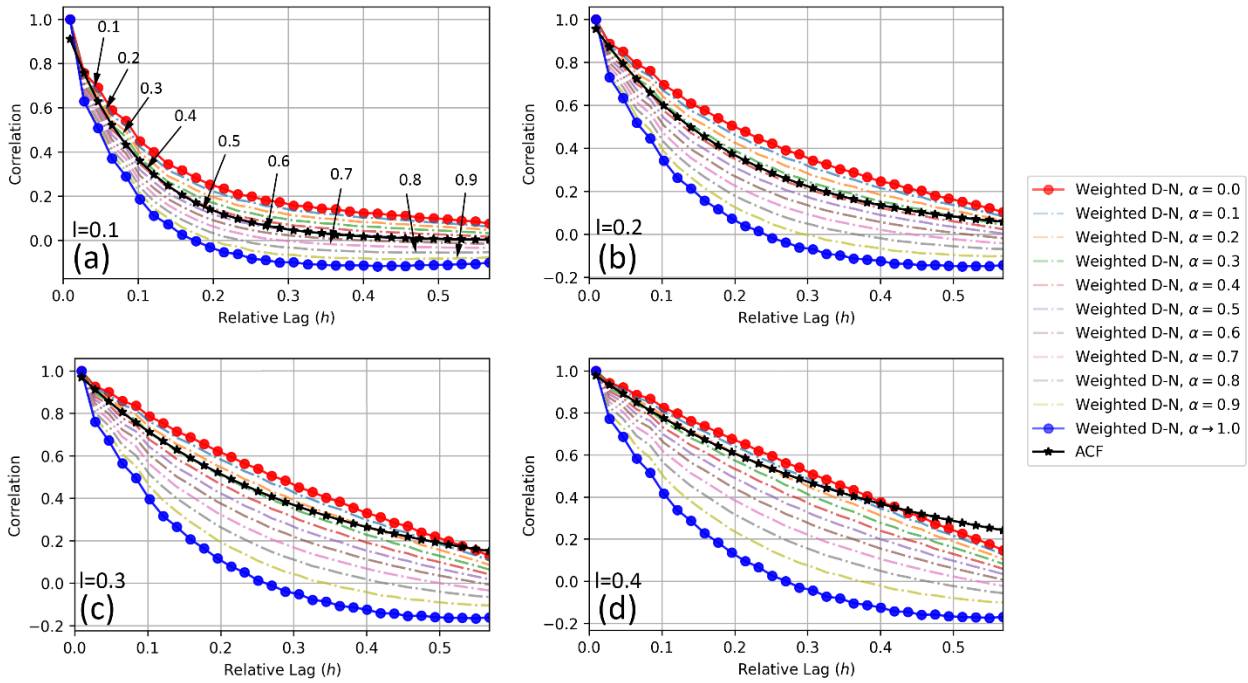

Figure 5.6: Average covariance functions over Ω for weighted D-N with $\lambda = \lambda_2$ for full range of α for l equal: (a) 0.1, (b) 0.2, (c) 0.3, and (d) 0.4

In both Figures 5.5 and 5.6, the dashed curves plotted between the maximal and minimal α values relate to linear increases in α between 0 and 0.9999.

Finally, Figure 5.7 compares the average covariance function over Ω of all considered boundary conditions with the true ACF equation (3.17), where the optimal values of α at each l have been chosen for both weighted D-N conditions. The coefficient of determination R^2 of the covariance functions and (3.17) is used to determine which α resulted in the best fit, by maximising R^2.

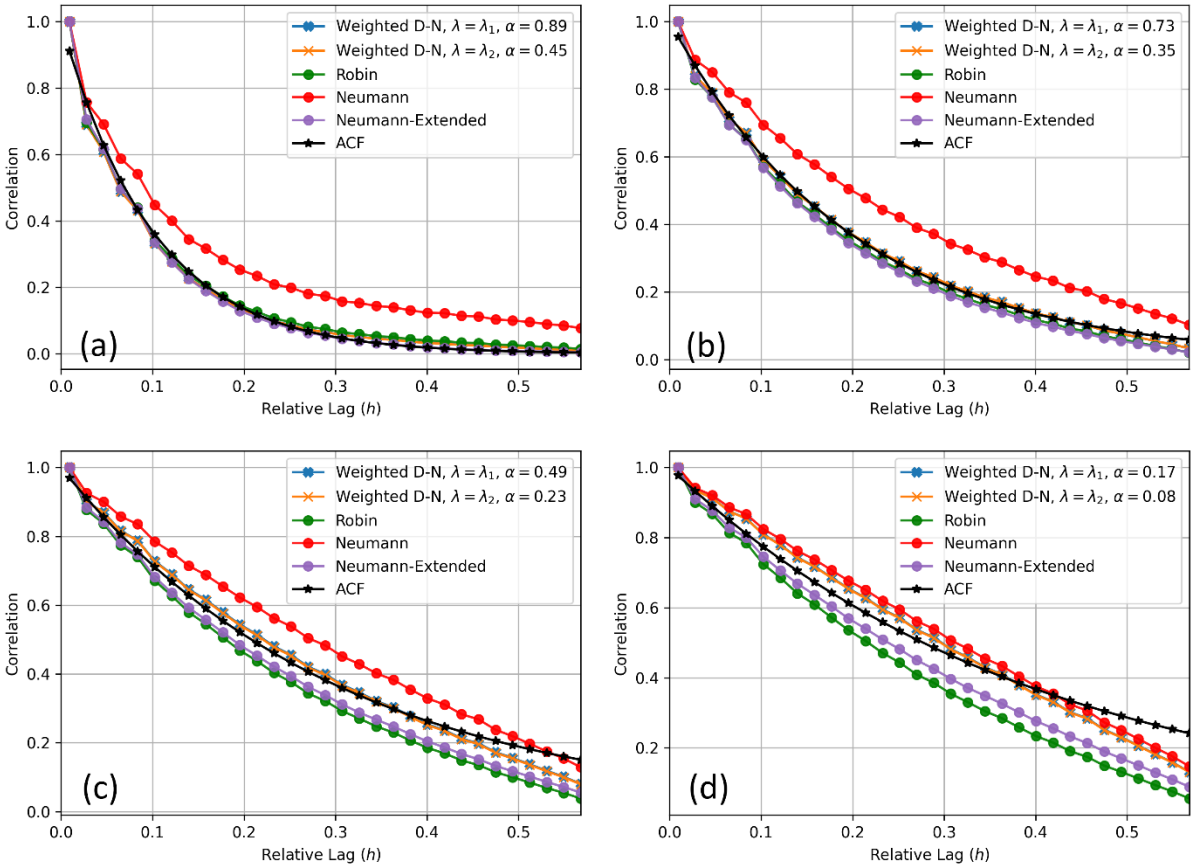

Figure 5.7: Average covariance functions comparison for weighted D-N with $\lambda = \lambda_1$ and $\lambda = \lambda_2$, Robin, Neumann and Neuman-Extended boundary conditions for full range of α for l equal: (a) 0.1, (b) 0.2, (c) 0.3, and (d) 0.4

Figure 5.5 shows that the curves converge as $\alpha \to 0$, suggesting that the optimal α values will be more variable with increasing l. What is more enlightening are the results seen in Figure 5.7, in which all tested boundary conditions are compared. In (a), almost all applied boundary conditions result in a correlation structure that matches well with the ACF, with the exception being the Neumann condition without domain extension due to more of the domain being dominated by Ω_B. As l increases, the performance of the proposed method progressively degrades due to Ω_B becoming larger, meaning that the approximation of equation (3.17) will weaken in all cases. However even though there is a reduction in accuracy, the weighted D-N with optimal α appears to give better matches to the ACF than the standard applied boundary conditions.

This can be quantified by computing the R^2 values of the curves presented in Figure 5.7 to evaluate their performance in matching the correlation structure of equation

(3.17) with increasing l. Consequently, the optimal values for α at each l used in Figure 5.7 were determined through maximising R^2 when measuring the goodness of fit between the weighted D-N covariance function curves over Ω with the ACF equation (3.17). Figure 5.8 shows the full comparison of all considered boundary conditions in terms of their R^2 value for average covariance functions computed over Ω and Ω_{B}, where the suffix "- F" and "- B" denote calculation over the full domain and near-boundary respectively.

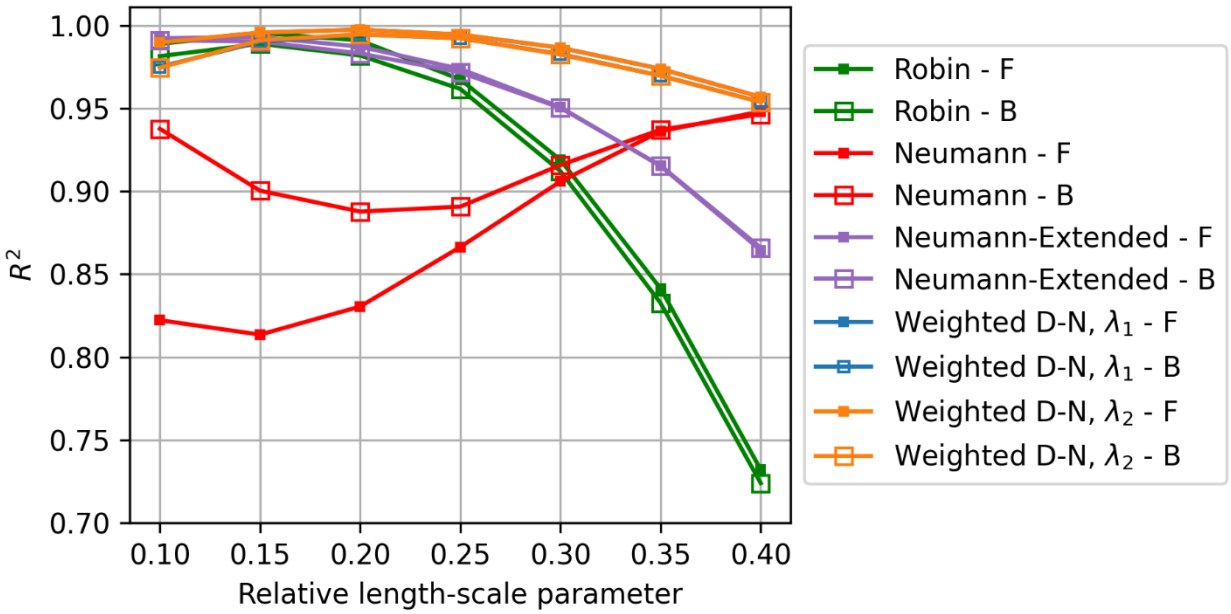

Figure 5.8: R^2 values for average covariance functions of all considered boundary conditions, where optimal α values are utilised, computed over Ω and Ω_B denoted by the suffix "- F" and "- B" respectively

It can be seen in Figure 5.8 that the weighted D-N approach yields a more consistent match to the ACF. Almost all applied boundary conditions result in fields that follow a similar pattern of a decreased wellness of fit as l increases, and similarly after a certain point as $l \to 0$. An exception is seen when the Neumann boundary condition is applied. As $l \to 0.5$, the correlation structure becomes unchanging, where further increasing l will have no effect on the static structure. By this, we can assume that the correlation structure is beginning to stabilise at $l = 0.4$, which can be seen in the difference in the covariance function of the Neumann boundary condition in Figure 5.7 (c) and (d). Thus, as l increases, the ACF will shift closer to the static Neumann covariance curve, resulting in a larger R^2 value but not necessarily a truer correlation structure. It is also worth noting that when $l = 0.5$, the domain $\Omega = \Omega_{\mathrm{B}}$, suggesting

that the error in the correlation structure at the boundary is seen throughout the whole domain regardless of the applied boundary condition. Figure 5.8 also shows that the Robin condition with $\lambda = 1.42l$ may not always be the best choice for approximating the ACF due to its sharper fall in R^2. This supports the suggestion in Roininen et al. (2014) that λ could be given as a function on the boundary.

The effect of the applied boundary condition on the level of error in Ω_{B} can also be quantified in this way, being visualised in Figure 5.8 as the separation between a given boundary condition's R^2 curves when calculated over Ω and Ω_{B} respectively. The largest level of disparity is seen when the Neumann boundary condition is applied without extension, where the covariance functions calculated over Ω_{B} appear to have a better fit. This can be further seen in Figure 5.2 (d), where the centre of the domain appears more diffuse. On the other hand, Neumann-Extended results in the least error over Ω_{B}. This is due to the computational domain being extended, and the errors seen in the near-boundary will not be carried through to the inner cube Ω where the covariance functions are calculated. The weighted D-N approach also has marginal differences in R^2 over Ω and Ω_{B}, where the choice of $\lambda = \lambda_1$ or $\lambda = \lambda_2$ has negligible effects on the level of difference. As l decreases, the near-boundary effects can be seen to reduce to the point where the curves appear identical, suggesting that an appropriate choice of α can mitigate error seen over Ω_{B}. This is in contrast to the Robin condition, whose near-boundary effects in fact begin to increase as l decreases from 0.15 to 0.1, and the Neuman-Extended condition whose near-boundary effects increase over the full domain but decrease over the near-boundary region with decreasing l in this range (see Figure 5.9). When generating fields with Neumann-Extended boundary conditions, the combination of domain extraction and a decreasing l suggests the error in the near boundary and full domain will converge due to the shrinking of near-boundary region as l reduced. After a certain point, the difference between the boundary regions of the weighted D-N conditions begins to grow as seen in Figure 5.9, and could be mitigated with slight variation in the chosen α or by using a finer mesh.

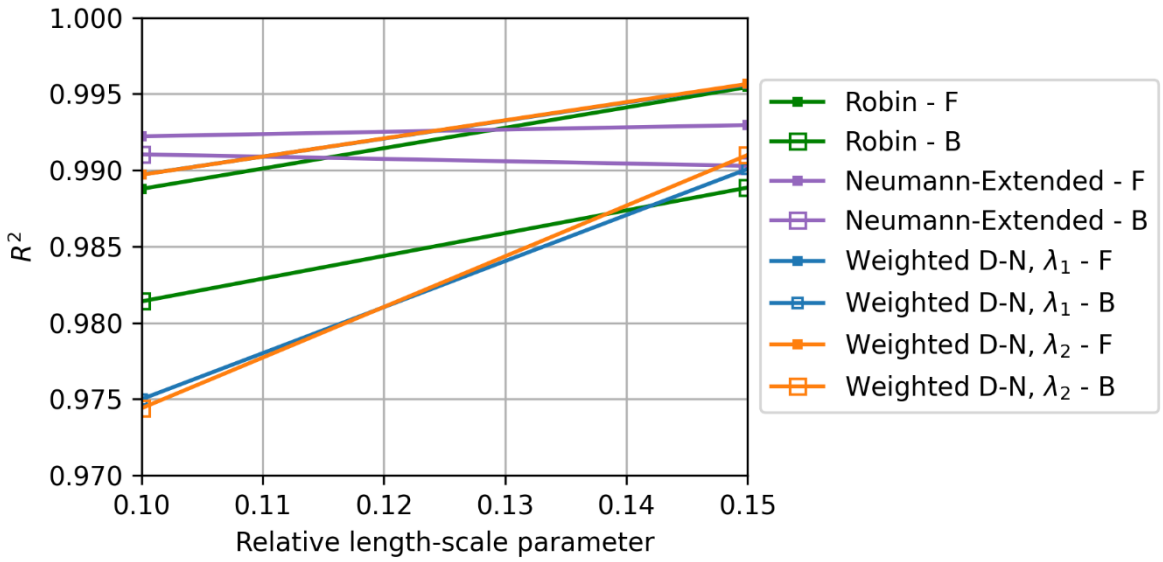

Figure 5.9: R^2 values for average covariance functions over a relative length-scale of 0.1 - 0.15 for all considered boundary conditions excluding the standard Neumann condition, where optimal α values are utilised, computed over Ω and Ω_B denoted by the suffix "- F" and "- B" respectively

Finally, the relationship between the optimal values of α with respect to l can be determined as seen in Figure 5.10, where 'Data' refers to the calculated optimal α for a given relative length-scale, and 'Fitted' are curves fit to said data.

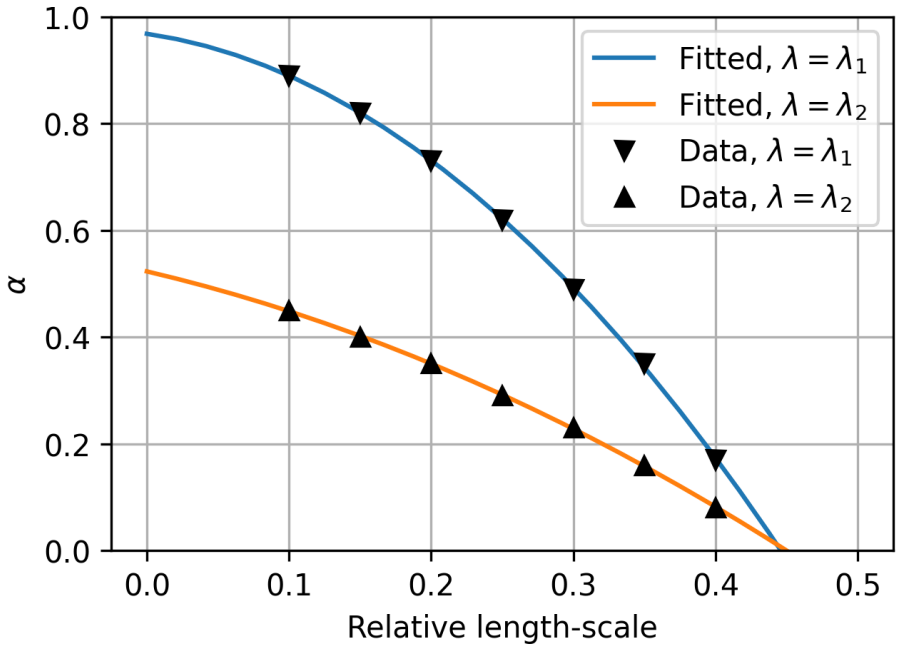

Figure 5.10: Relationship between the relative length-scale l and optimal α

The functions can be described as

$$\alpha(l) = al^2 + bl + c \tag{5.8}$$

where $a = -4$, $b = -0.3857$, and $c = 0.9679$ when $\lambda = \lambda_1$, and $a = -1.1905$, $b = -0.6262$, and $c = 0.5229$ when $\lambda = \lambda_2$. The functions were determined over l from 0.1 – 0.4, but are applicable from 0 – 0.445. Both instances of equation (5.8) are quadratic, with $\lambda = \lambda_2$ being smoother in nature. This suggests that upon implementing the weighted D-N condition, small variations in the chosen α from its optimal value will have a less detrimental effect on the resulting correlation structure when $\lambda = \lambda_2$ as opposed to $\lambda = \lambda_1$. As l increases, the optimal value of α reduces in both cases. This relates to a more dominant Neumann component in the condition. This also agrees with the increase in R^2 for the Neumann condition, suggesting that at larger l, having a larger Neumann component would result in a better matching correlation structure. It is also worth highlighting that both fitted curves converge to a common root $l = 0.445$, where the Dirichlet component of the weighted D-N condition vanishes, suggesting that the pure Neumann condition will give just as sufficient an approximation.

5.3.4 Mesh Convergence

A similar testing procedure was carried out as above for $l = 0.1$ over the same 1 m cube as in Figure 5.4 (a) for different mesh sizes to determine if the solution is mesh converged. Here, the weighted D-N boundary condition was applied with $\lambda = \lambda_2$. The mesh was divided into relative element lengths $\mathrm{L_e}$ of 0.1, 0.05, 0.03333, and 0.025 for the regular hexahedral elements. The testing range of α was chosen as 0.41 – 0.49 to assess the capabilities of the relationship between α and l given in equation (5.8) and shown in Figure 5.10, where the functions exact value gives α as 0.45. Here, the accuracy was determined by Root Mean Squared Error (RMSE) and R^2 values of the covariance function plots to the true ACF. The RMSE was used here as an additional metric as it quantifies the error as absolute values as opposed to the R^2 which is a percentage-based indicator and can be less interpretable for ill-fitting curves. The covariance functions compared with the ACF for different mesh sizes can be seen in Figure 5.11.

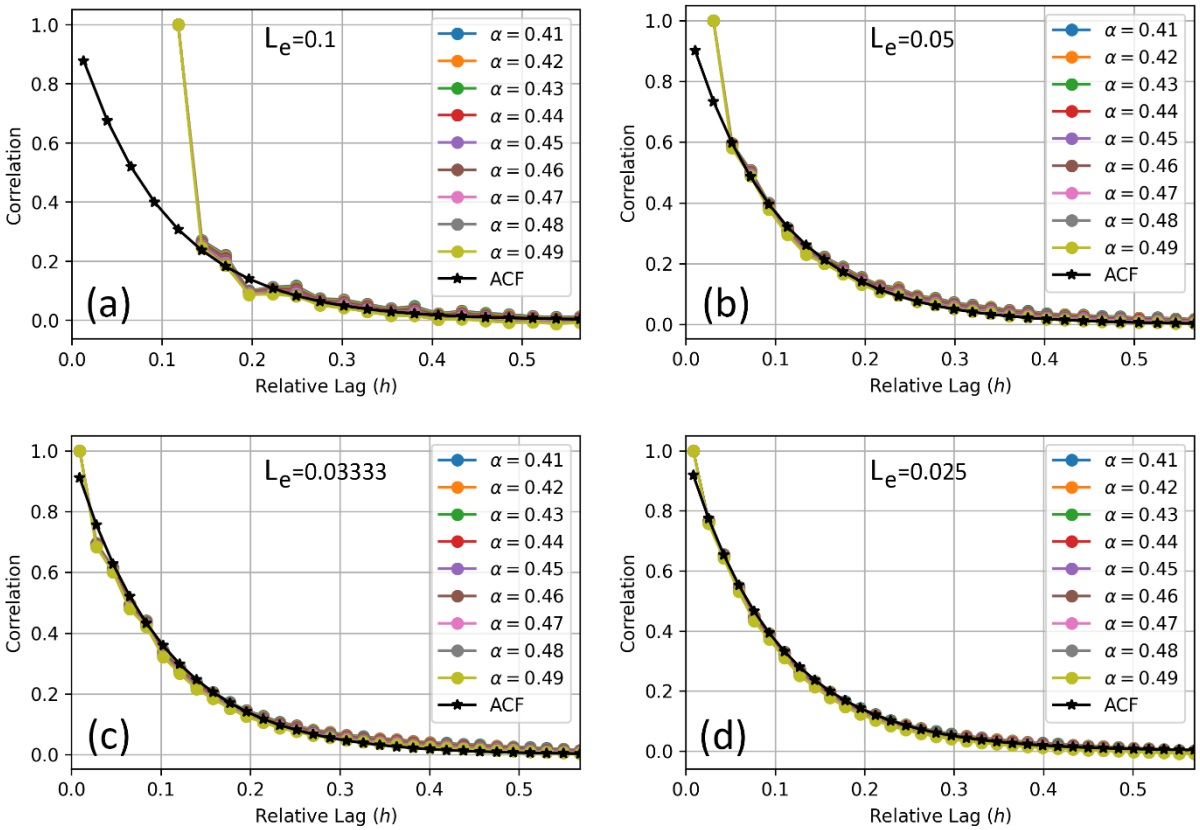

Figure 5.11: Covariance plots of cubed domain, with $l = 0.1$, over the optimal range of α for L_e of (a) 0.1, (b) 0.05, (c) 0.03333, and (d) 0.025

Apart from the element length 0.1 case (Figure 5.11 (a)), the covariance plots match well with the true function, showing that for all mesh sizes, the mesh is converged and the λ_2 relationship gives a sufficiently accurate choice of α. This can be seen further in Table 5.1, where the R^2 and RMSE values are presented for the considered mesh sizes when $\alpha = 0.45$, with the RMSE values being visualised in Figure 5.12.

Table 5.1: R^2 and RMSE for α=0.45 and $l = 0.1$ for different relative mesh sizes

L_e	R^2	RMSE
0.1	-2.60544	0.19559
0.05	0.94716	0.05224
0.03333	0.98970	0.02410
0.025	0.99522	0.01643

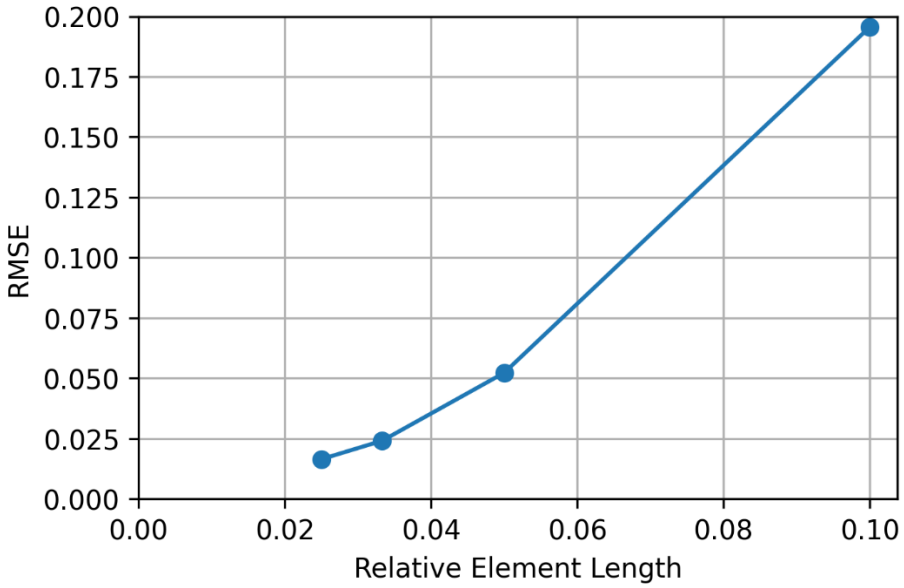

Figure 5.12: RMSE values for α=0.45 and $l = 0.1$ with different relative mesh sizes

The convergence of the mesh -as well as the confirmation of the applicability of the λ_2 relationships in equation (5.8)- suggests that the values of α fit through the parametric investigation are adequate, and were evaluated over an appropriate mesh. When considering an appropriate mesh size, it is accepted that the element length should less than $l/2$ (Huang and Griffiths, 2015), ensuring that the variation seen over length l is well represented. In practise, $L_e \approx l/5$ is more than sufficient in capturing the local variation observed within l.

It is worth noting that these results are related to the choice of covariance kernel when formulating the governing SPDE. If other kernels were chosen, then it is necessary to repeat the process as the optimal values of alpha would change.

5.3.5 Dog bone example

To further test the applicability of the weighting parameter, random fields were generated over a dog bone shaped specimen, whose shape is synonymous with the experimental determination of tensile properties of cement composites (Na et al. 2016; Krishnaraja et al. 2018; Zhu et al. 2019). The domain Ω was discretised to contain 91203 nodes, where the mesh and relative dimensions can be seen in Figure 5.13 (a).

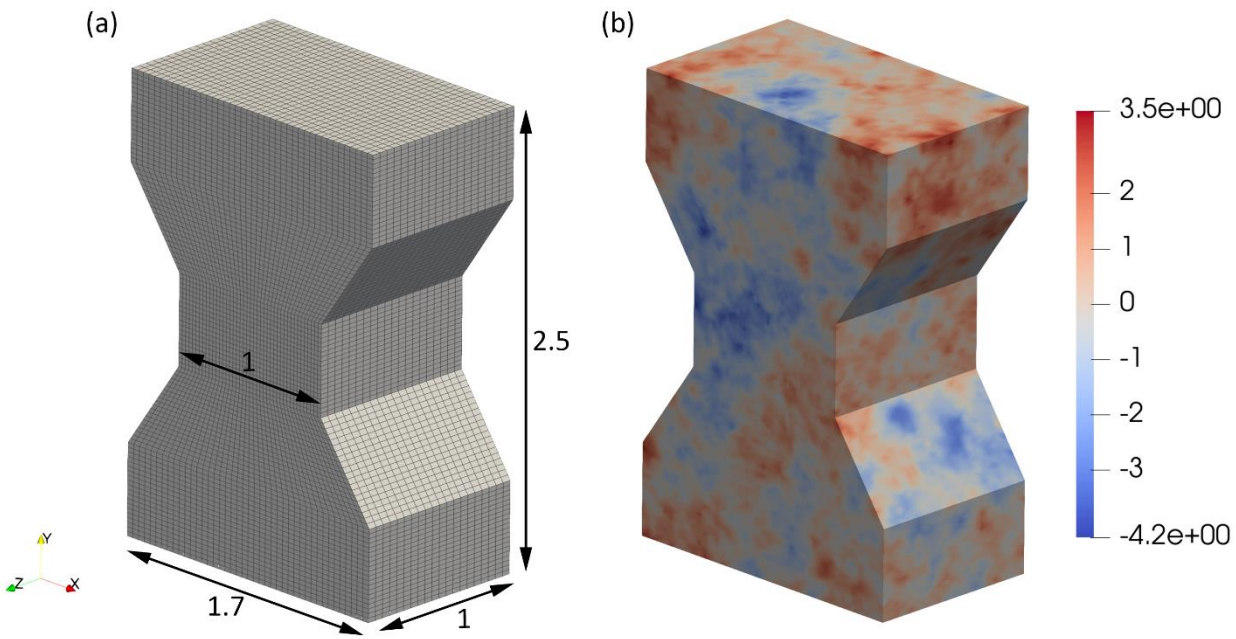

Figure 5.13: (a) Dog bone unstructured mesh consisting of hexahedral elements, (b) random field realisation when using the weighted D-N boundary conditions with $\alpha = 0.32$ *for* $l = 0.25$ *(scaled to zero mean and a standard deviation of 1)*

The length scale given is relative to the central portion of the dog bone, whose dimensions are of 1 in both the x- and z-axis. The size and shape of the domain was chosen such that the percentage of the domain which is dominated by Ω_B is relatively low. This ensured that the problem formulation is not heavily constrained due to the domain shape, and the error seen in the near-boundary region does not propagate through the whole domain. Similar to the parametric regime, 10 fields were generated with a length-scale of $l = 0.25$ -relative to the dimensions of the central portion- for each applied boundary condition, with $\alpha = 0.32$ for the weighted D-N condition with $\lambda = \lambda_2$. A sample field is shown in Figure 5.13 (b) when using the weighted D-N condition with $\alpha = 0.32$. The average covariance function for each applied boundary condition was determined, as seen in Figure 5.14.

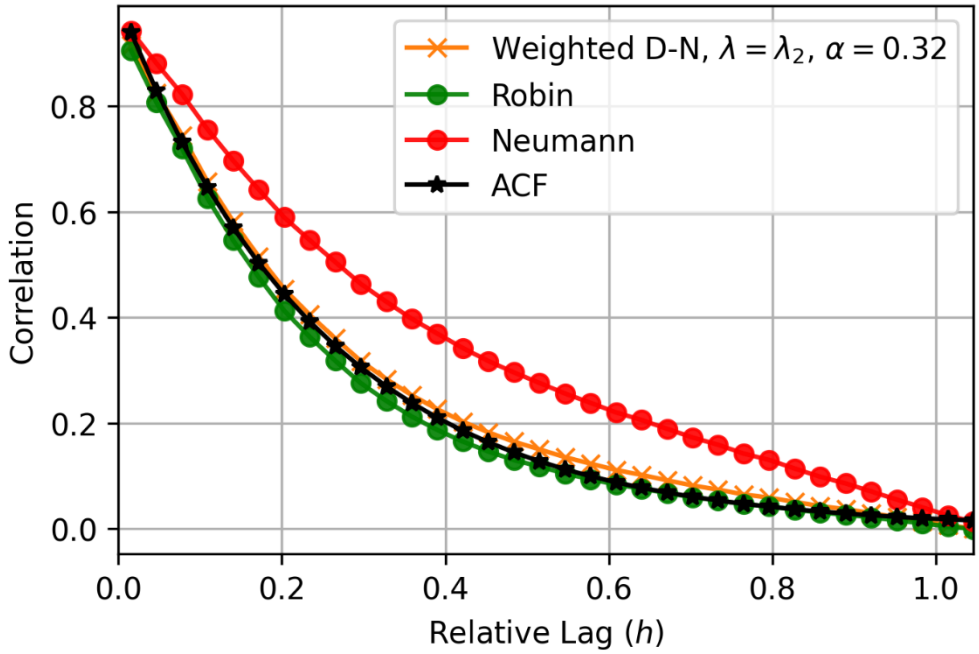

Figure 5.14: Average correlation function comparison across the dog bone domain when applying the Robin, Neumann, and Weighted D-N boundary condition with $\alpha = 0.32$

As expected, the Neumann case offers the worst fit to the function, with the Robin and weighted D-N conditions offering a marginal under and over estimation respectively. The choice of α adopted here is based on a function obtained from a domain where the relative length-scale is well defined in all directions. For the case of the dog bone, the true relative length-scale differs in each portion of the domain, where the top and tail sections in fact have a smaller associated l than that considered. This will be reflected in the chosen α, where a smaller l suggests taking a larger α. In this way, taking a larger alpha will shift the covariance function closer to the true ACF, converging to the best possible fit in terms of the error estimation for this domain and applied boundary condition. Both the Robin and weighted D-N provide an $R^2 > 0.99$ from Figure 5.14, suggesting that both are more than sufficient to apply in this case. The benefit of employing the weighted D-N condition is the ability to tune α by small perturbations to further reduce the error based on the chosen relative length-scale and domain geometry.

The near-boundary error associated with complex geometries is related to the size of the near-boundary region relative to the full domain, as well as the distinct portions that it may encompass. Having complex geometry could lead to regions of the

domain that are entirely made up by the near-boundary region due to its size being dependent on the length-scale. Having a smaller relative length scale value would suggest a reduction of the near-boundary region, so the chance of having zones that are purely made up of the near-boundary region would decrease. However, it is possible that small relative length-scales will not be sufficient to reduce this as there could be thin sections of domain that contain points that are always close enough to the boundary to be considered inside the near-boundary region.

5.4 Conclusions

This chapter presents an optimised boundary condition applied to the formulation of the stochastic PDEs solved to generate correlated Gaussian random fields. The condition aims at reducing spurious values in the near-boundary region, and has been shown to perform well inside and outside of the range of the parametric analysis that followed. It was found that the near-boundary error of the weighted D-N approach reduced with decreasing l when employing optimal values of α, and is more consistent with the correlation structure of the full domain. Similarly, the weighted D-N approach provides an overall better match to the autocorrelation function when compared with all other applied boundary conditions. This was also tested for a more complex geometry, and was found to perform well. The functions for α based on the parametric study enable its optimal value to be determined for other domains and desired length-scales.

5.5 References

Bachmaier, M., & Backes, M. (2011). Variogram or Semivariogram? Variance or Semivariance? Allan Variance or Introducing a New Term? Mathematical Geosciences, 43(6), 735–740. https://doi.org/10.1007/s11004-011-9348-3

Biswas, A., & Cheng, B. (2013). Model Averaging for Semivariogram Model Parameters. In Advances in Agrophysical Research. InTech. https://doi.org/10.5772/52339

Calvetti, D., Hadwin, P. J., Huttunen, J. M. J., Isaacson, D., Kaipio, J. P., McGivney, D., Somersalo, E., & Volzer, J. (2015). Artificial boundary conditions and domain truncation in electrical impedance tomography. Part I: Theory and preliminary results. Inverse Problems and Imaging, 9(3), 749–766. https://doi.org/10.3934/ipi.2015.9.749

Daon, Y., & Stadler, G. (2018). Mitigating the influence of the boundary on PDE-based covariance operators. Inverse Problems & Imaging, 12(5), 1083–1102. https://doi.org/10.3934/ipi.2018045

J. Huang, & D.V. Griffiths, (2015). Determining an appropriate finite element size for modelling the strength of undrained random soils. Computers and Geotechnics, 69, 504-513. https://doi.org/10.1016/j.compgeo.2015.06.020

Khristenko, U., Scarabosio, L., Swierczynski, P., Ullmann, E., & Wohlmuth, B. (2019). Analysis of Boundary Effects on PDE-Based Sampling of Whittle--Matérn Random Fields. SIAM/ASA Journal on Uncertainty Quantification, 7(3), 948–974. https://doi.org/10.1137/18M1215700

Krishnaraja, A. R., Kandasamy, S., & Kowsalya, M. (2018). Influence of polymeric and non-polymeric fibers in hybrid engineered cementitious composites. Revista Română de Materiale / Romanian Journal of Materials, 48(4), 507–513.

Na, N. /, View, N. A., Moradian, M., Moradian, M., & Shekarchi, M. (2016). Durability and dimensional stability of steel fiber reinforced cementitious mortar in comparison to high performance concrete. Asian Journal of Civil Engineering (BHRC), 17(4).

Roininen, L., Huttunen, J. M. J., & Lasanen, S. (2014). Whittle-matérn priors for Bayesian statistical inversion with applications in electrical impedance tomography. Inverse Problems and Imaging, 8(2), 561–586. https://doi.org/10.3934/ipi.2014.8.561

Zhao, Y., & Wall, M. M. (2004). Investigating the Use of the Variogram for Lattice Data. Journal of Computational and Graphical Statistics, 13(3), 719–738. https://doi.org/10.1198/106186004X2444

Zhu, B., Pan, J., Nematollahi, B., Zhou, Z., Zhang, Y., & Sanjayan, J. (2019). Development of 3D printable engineered cementitious composites with ultra-high tensile ductility for digital construction. Materials & Design, 181, 108088. https://doi.org/10.1016/j.matdes.2019.108088

Chapter 6

Three-dimensional unsaturated flow in heterogeneous soil through tractable Gaussian random fields

6.1 Introduction

The variability present in a given material can have a large influence over its behaviour and performance. Unlike homogenous materials that exhibit consistent properties throughout their volume, heterogeneous materials possess spatial variations in their characteristics, be it in terms of composition, micro-structure, or mechanical properties. Whilst heterogeneity can be a desired trait, such as in composite materials, it can also introduce uncertainty in predictability, quality control, and long-term durability. This variability should be accounted for during design, testing, and manufacturing of engineering systems, where robust methods of quantifying the resulting uncertainty must also be employed.

Fingered flow in soils is one of many examples of how heterogeneity influences fluid flow in unsaturated soils. When water infiltrates into soils that are spatially variable in their properties, a uniform wetting front is not often observed. Instead, due to differences in soil composition, texture, or compaction, water may flow through certain preferential flow pathways, creating channels or "fingers" of more rapid moisture movement (see Figure 6.1).

Figure 6.1: A slice obtained from MRI imaging of a 15 x 15 x 15 cm^3 sand sample showing a fingered profile after having 600ml of water introduced over 3 minutes to the top surface (after Posadas Ay et al. (1996)*)*

Understanding and predicting fingered flow is crucial in many geotechnical engineering related fields where water and soils are components, affecting processes such as water availability, nutrient transport, and slope stability.

In this chapter, a coupled FE model for analysing fingered flow in unsaturated soils is presented, where correlated Gaussian random fields are used to represent the heterogeneity of soil transport properties. The random field, from which the stochastic properties are computed, is generated by solving a set of partial differential equations (PDEs) derived from Whittle-Matérn's autocorrelation function (Lindgren et al. 2011; Roininen et al. 2014), as detailed in Chapter 3. The approach is applicable to very large data sets (>10^6) because the sparsity of the matrices in the discretised PDE allow for extremely efficient treatment. By contrast, classical geostatistical methods often struggle to solve such problems (Vergara et al. 2018). For further discussion on the SPDE approach versus kernel-based methods, see Simpson et al. (2012). Since the PDEs have the same structure as those of the transport problem, the same FE framework may be used for their solution, thereby removing the need for potentially complex dual implementations (Jiang et al., 2022).

This proposed technique has not previously been applied to the simulation of fingered flow in two or three dimensional domains. The novel approach presented here is applied to the representation of unstable fingered flow and compared to

experimentally observed in situ behaviour (Wang et al. 2003). Similarly, a new approach to account for spatially varying boundary conditions is presented. The method considers the spatial variation in material properties on the boundary, and weights the applied boundary condition such that there is more infiltration in some areas than in others.

Section 6.2 presents the application of random fields for representing material heterogeneity; Section 6.3 considers a novel way to apply boundary conditions whilst accounting for surface heterogeneity; Section 6.4 presents the results of the simulations; Section 6.5 deals with the uncertainty of the presented results; and Section 6.6 concludes on the investigation and modelling approach.

6.2 Random field application

The discretised stochastic PDE (4.30) is solved as a pre-process to the moisture transfer problem, resulting in a normalised array with field values for each nodal position. It was implemented to be modular, such that the model is not dependent on running the field generation algorithm with every simulation if it is not necessary for the analysis. The generated array is scaled using experimentally determined mean and standard deviation values of the transport parameter being considered to compute the required parameter values for the spatial domain. Relevant parameters could, for example, include the grain size, porosity, initial moisture content and hydraulic conductivity. The chosen parameters have a correlated structure based on the Whittle-Matérn autocorrelation function. When the model is run, a stochastic input file determines the stochastic components of the model to execute, including which parameters to represent by random fields, whether they are correlated to each other, and the specific statistical properties that they must hold.

In the present work, the fields are scaled using mean and standard deviation values from experiments. In addition, to ensure that the values remain physically meaningful, the distributions were capped at 3 standard deviations from the associated mean values. This accounts for over 99.7% of the overall distribution. In all of the cases considered in the present work, this was sufficient to ensure that the values remained physically meaningful. If problems arise for which this is not the case, then, either the standard deviation can be reduced, or the distribution capped to ensure only physically meaningful values are considered.

Figure 6.2 presents a flow chart of how the variability propagates throughout the analyses, specifically in terms of the constitutive components of the model that govern the hydraulic response. By introducing the random field initially, the spatial variability propagates through the constitutive components of the model, resulting in explicit and implicit variability of model parameters. The computational non-linearity can grow quickly due to the relations between model parameters.

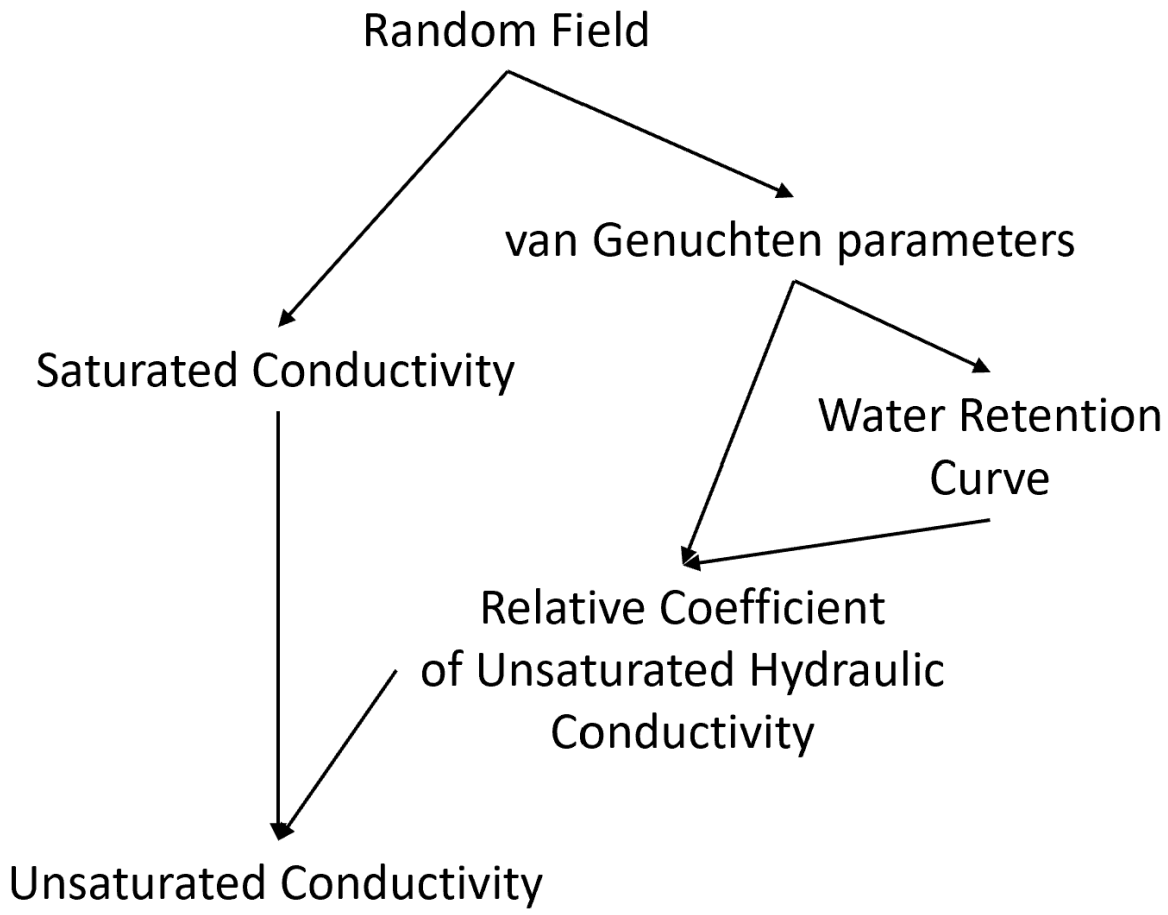

Figure 6.2: A flow chart of the propagation of variability throughout the model (see Section 6.4 for details of the specific terms)

6.3 Heterogeneity within boundary conditions

When considering rainfall on a soil surface, the resulting infiltration fluxes on a region of more permeable soil -typically associated with the larger pores along the soil surface- would be expected to be greater than those in nearby less-permeable regions. As infiltration progresses, the nearby pores will receive less water due to the highly conductive neighbouring regions, further reducing the available water for the rest of the surface. This results in water entering the soil in the most conductive

regions of the soil first, and then pluming outwards as the degree of saturation and conductivity of the medium increase. Similarly, the movement of water into the soil will be much more concentrated initially to the most conductive areas, and then smooth over the whole domain with increasing saturation of the near surface. Physically, this can be thought of as allowing for the water to track to the paths of least resistance.

Surface fluxes are typically represented as a uniformly distributed flux applied to the boundary surface. This assumes that water applied to the surface of the domain will enter the soil body at equal rates for any given position on the boundary, suggesting that surface conductivity and other physical parameters such as pore-size must be uniform across the surface. This also implies that the soil body is solely responsible for driving unstable flow, and that the surface has little influence. In reality, this is not the case, as variability at the surface interface can influence the behaviour of the invading fluid phase. If a material body is assumed heterogeneous, as in the current investigation, then the same assumption of variability should logically be extended to its boundaries. It follows that the boundary condition applied at the infiltration surface, be it a Neumann or Dirichlet condition, should be weighted to account for spatial variations in surface conditions.

Here, a convenient and novel approach is proposed that introduces spatial variation at the domain surface. This is accomplished by weighting the applied flux in localised regions of a Kernal function, referred to as “blocks”, such that the total applied flux is preserved. The surface variation used to weight the flux is taken directly from the variation in material properties obtained through the generated Gaussian random fields. In this way, variation in surface penetration can be coupled or decoupled from the correlated structure present in the spatially varying material properties of the soil body.

In 2-D, each block is associated with a collection of nodes from the surface. Figure 6.3 shows a schematic of how this is applied in 2-D. A schematic of the approach in 3-D is seen in Figure 6.4 (a), where the block under consideration is the highlighted centre, and the shape functions of each axis are in red.

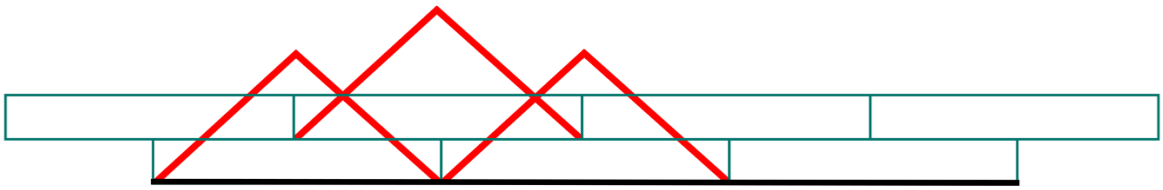

Figure 6.3: Schematic for the localised distribution of flux. The black line represents the surface, the green blocks are the regions for distribution, and the red lines are the linear hat shape functions relating to a given block

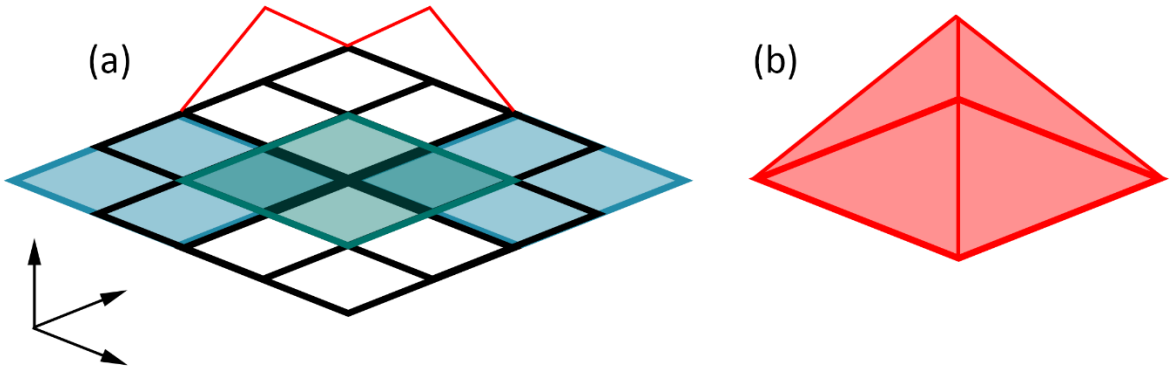

Figure 6.4: Schematic of varying surface flux application. (a) Green centre is the problem domain, with 8 over lapping squares, and the linear shape functions in red, where (b) shows their combination as a square based pyramid surface

In 3-D, the flux is scaled by the linear combination of hat shape functions. The blocks overlap so as to preserve the partition of unity at all positions in the domain, such that the flux is preserved and the effects of nearby variations are accounted for. For a given node of index i, this is calculated as

$$q_i = N_x N_z \frac{\sum q}{\sum K_s} \mathbf{X}_i \qquad (6.1)$$

where q_i is the scaled flux at the i-th node, N_x and N_z are the linear shape functions in the x- and z-axis respectively, $\mathbf{X}_i$ is the random field value of K_s for the i-th node, and $\sum q$ and $\sum K_s$ are the sums of the applied flux and saturated conductivity of the considered infiltration surface nodes. Due to the overlapping Kernel functions, the i-th node value will be incrementally updated, such that the shape functions prevent over-scaling.

The blocks discretise the domain into so-called “macro elements”, such that the applied flux is weighted over each block. In both 2-D and 3-D, it is assumed that the macro element length is defined by the length-scale parameter of the main field. Algorithmically, the model scans over each overlapping macro element, and interpolates the flux based on the generated field values of K_s. This approach could also be done for other physical parameters, such as the unsaturated conductivity, or variation in pore size. By applying the boundary flux in this way, as opposed to a uniform distribution, it is possible to simulate water infiltration into regions where it would naturally track due to the higher conductivity of the material.

6.4 Application: unstable preferential flow

Having described the theoretical and numerical details of the model in Chapters 3 and 4, as well as its implementation, it is now applied to consider infiltration into a heterogeneous soil mass. Specifically, a set of field experiments undertaken by Wang et al. (2003) is considered. In their study, Wang et al. (2003) reported infiltration profiles within an in-situ layer of Hanford Sandy Loam (HSL) at the University of California Kearney Research Centre in Parlier, California. A detailed description of the soil material properties with depth is given in the study, with the particle size distribution being illustrated in Figure 6.5. The figure illustrates the percentage of particles that are smaller than a given particle diameter.

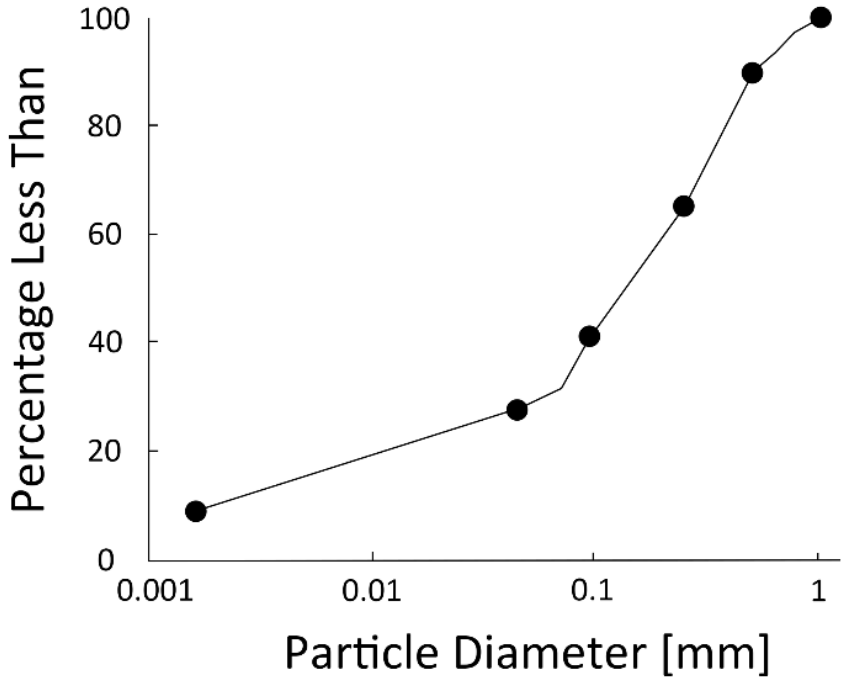

Figure 6.5: Particle size distribution (log scaled) for Hanford Sandy Loam (after Wang et al. (2003)*), where the y-axis indicates the percentage of particles that are smaller than a given particle diameter*

At the start of the experiment, a simulated rainfall condition was applied continuously to a soil surface area of 1 m x 1.2 m using a moving spraying system, originally designed by Ghodrati et al. (1990), for 6 hours at a rate of 1.5 cm h^{-1}. Once 9 cm of water had been applied, the system was turned off and the water was given time to redistribute within the body of soil. At 12, 15, 18 and 22 hours, the soil was excavated to a 1 m depth to reveal the flow patterns. As the wetting front was not visible, a water-soluble anionic brilliant blue dye was applied as an initial high concentration pulse (2-5%) for detection. However, signs of dye retardation led to a pH indicator method being applied (Wang et al. 2002). The pH was elevated using a 2.5% water solution of ammonium carbonate, enabling a pH indicator comprising thymol blue and cresol red (dye contents ~95%) dissolved in methanol (95% pure) to highlight the carbonate-affected areas.

In this example analysis, the heterogeneity of the domain is represented by variations in the saturated conductivity K_s and the van Genuchten parameters α_{vg} and n_{vg}. These directly affect the soil water retention curve (SWRC) and the

unsaturated hydraulic conductivity (Mualem 1976; van Genuchten 1980). The following form of the SWRC is adopted

$$S_l = \left(1 + \left(\alpha_{vg} u_l\right)^{n_{vg}}\right)^{\frac{1-n_{vg}}{n_{vg}}} \tag{6.2}$$

and the standard van Genuchten – Mualem model is used to represent the relative permeability

$$K_r = \sqrt{S_l}\left[1 - \left(1 - S_l^{\frac{1}{m_{vg}}}\right)^{m_{vg}}\right]^2 \tag{6.3}$$

where S_l is the degree of saturation, and $m_{vg} = 1 - 1/n_{vg}$. Equation (6.3) is combined with the nodal field values of K_s to attain the unsaturated conductivity at each node as

$$K_l = K_r K_s. \tag{6.4}$$

The primary material parameters used in the model were taken directly from the experimental data presented in Wang et al. (2003), and can be seen in Table 6.1 along with other the key model parameters. The mean value of saturated conductivity was taken as the average of those reported by Wang et al. (2003) and the standard deviation was calculated based on the values reported with depth across the sample. The van Genuchten parameters and their variations were calculated using the same procedure; these being estimated from the reported water entry pressures. The initial conditions were such that a hydrostatic hydraulic gradient was imposed, resulting in a variation of saturation having a mean value of 5 % and standard deviation of 1.5 %.

Table 6.1: Model parameters

	Saturated Conductivity, m/s	α_{vg}, Pa^-1	n_{vg}	Porosity	l (vertical) m	Density of Water kg/m^3
Mean Value	7.14 x 10^{-6}	0.00051	3	0.35	0.3	1000
Standard Deviation	2.3 x 10^{-6}	0.0001	0.1	-	-	-

The van Genuchten parameters are assumed to vary according to a Gaussian distribution with the parameters in Table 1, and result in the banded water retention and unsaturated conductivity curves shown in Figure 6.6 and Figure 6.7 respectively, with each point in the domain having an independent curve.

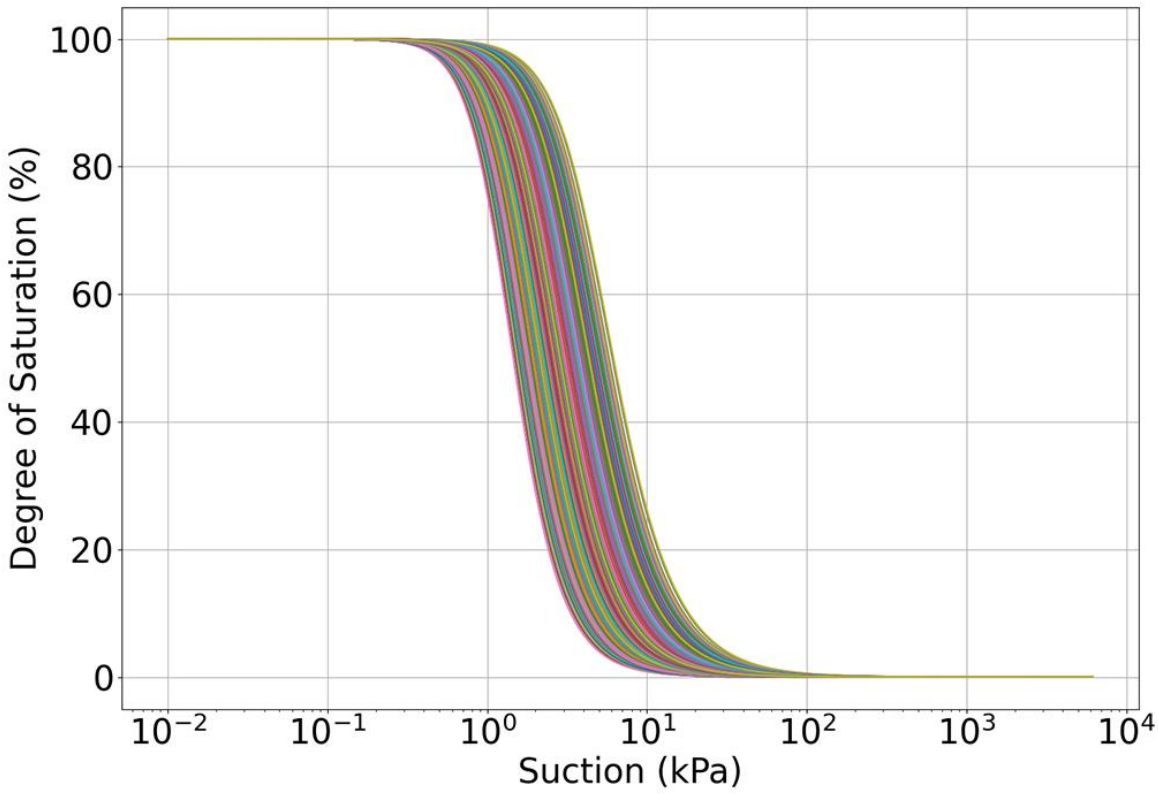

Figure 6.6: Soil water retention curves for R1, showing the banding as a result of variation in the saturated conductivity and van Genuchten parameters. Each curve relates to a node in the discretised domain

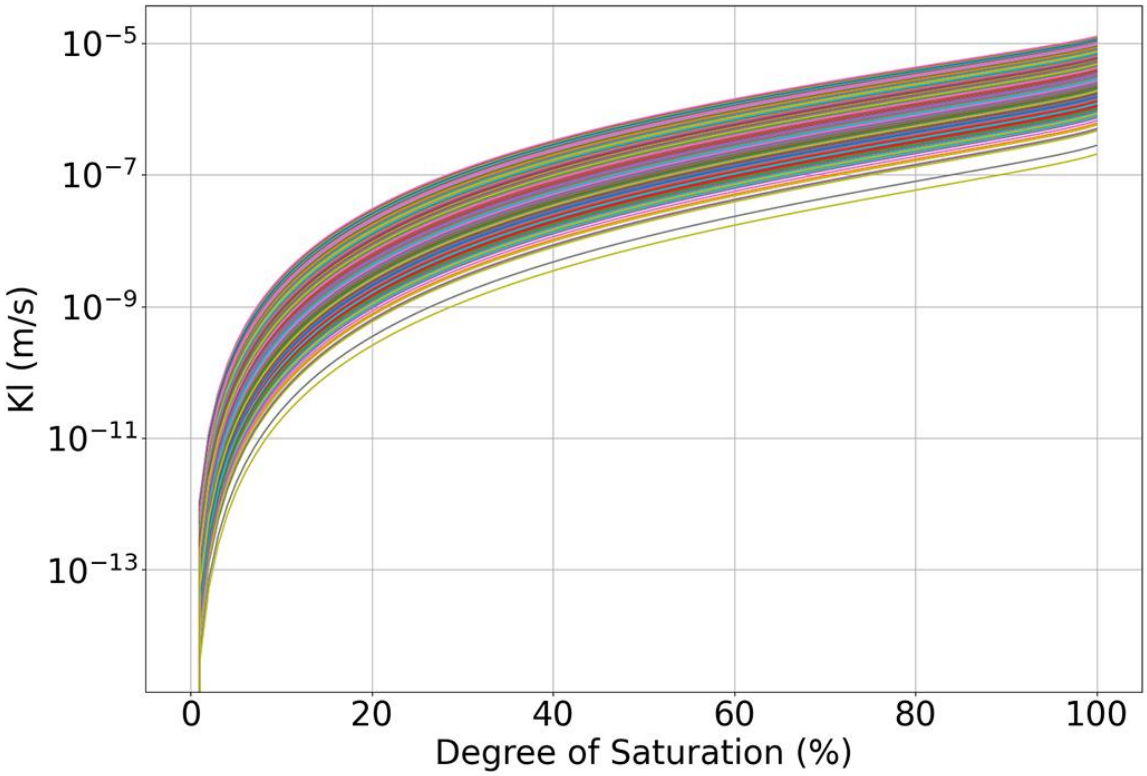

Figure 6.7: Unsaturated conductivity curves for R1, showing the banding as a result of variation in the saturated conductivity and van Genuchten parameters. Each curve relates to a node in the discretised domain

The numerical domain is defined as a three-dimensional soil mass with dimensions 1 m x 1.2 m x 1 m. Regular hexahedral elements with an element length of 25 mm were used to discretise the domain (with appropriate convergence checks undertaken), as seen in Figure 6.8. The boundary conditions, scaled using the method outlined above, are also illustrated in Figure 6.8. A constant timestep of 100 seconds was used for the simulation and was found to yield converged results.

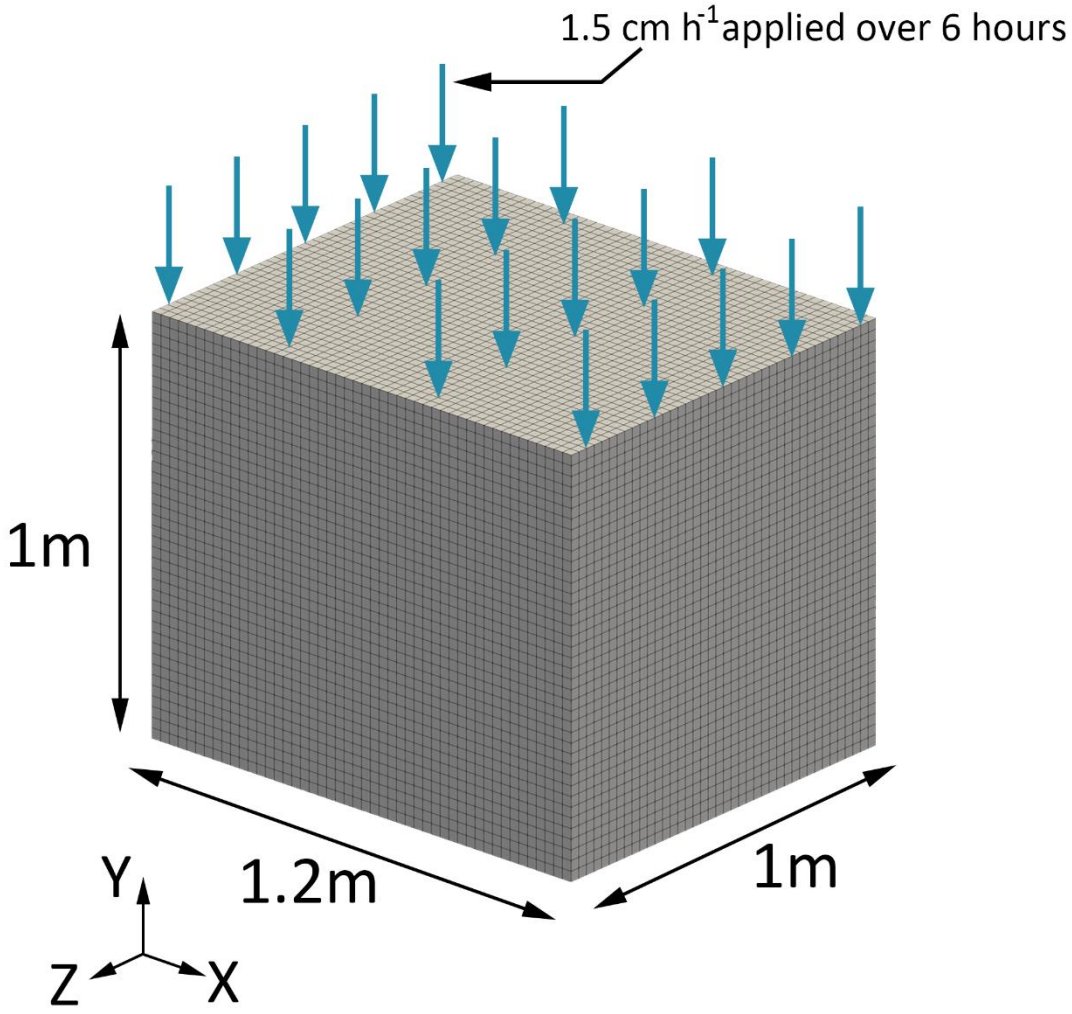

Figure 6.8: Schematic to show the simulation domain, its discretisation, and the boundary condition applied to the surface (as indicated by the arrows)

The boundary condition for the upper surface of the domain was taken directly from the field study data, with the first six hours of infiltration at a rate of 1.5 cm h^{-1} being considered. The applied boundary condition was scales using the method described in Section 6.3, based on variations in saturated conductivity on the surface. The analysis was undertaken for 28 hours to match the time over which moisture changes were measured in the experiment. As is standard with stochastic modelling, a number of numerical simulations were conducted, each with a different realisation of the problem. In the present study, the variation between these realisations relates to the field of saturated hydraulic conductivity and van Genuchten parameters. In total, 12 simulations were conducted. Here, the results of 3 typical realisations R1,

R2 and R3 are presented out of the total of 12. Convergence of the results in terms of confidence intervals of mean, maximum and minimum finger depths is considered in Section 6.5.

The length-scale parameters were assumed to be 0.1 m in the horizontal direction and 0.3 m in the vertical direction. These values were chosen to reflect the nature of the soil body, the way it has been tended and the flora it previously hosted. In particular, the soil was planted with nectarine trees until three years prior to the start of the experiment. Fruit trees are known to grow taproots which are characterised by their strong downward growth (Akin and Rottke 2011; Eshel and Beeckman 2013), and can decrease bulk density which leads to increased hydraulic conductivity (Carminati et al. 2009; Mubarak et al. 2009). Similarly, the presence of former root channels can lead to increased vertical hydraulic conductivity (Bengough et al. 2006). The soil body also received annual tillage as a means of weed control, leading to higher rates of hydraulic conductivity in both horizontal and vertical directions (Alletto and Coquet 2009; Kool et al. 2019). Specifically, the choice of the two length-scale parameters reflects the characteristic tillage dimension and the spacings of the vertical taproots, such that the reduction of soil bulk density will lead to a more conductive soil in the vertical direction.

Figure 6.9 shows the generated fields of saturated conductivity considered for the given stochastic parameters. The areas in red are more conductive, so the water will encounter less resistance travelling through these zones. Figure 6.10 shows the wetting front profile of R1 (at 0.5, 6 and 22 hours) during the simulation. Both R2 and R3 had a similar response.

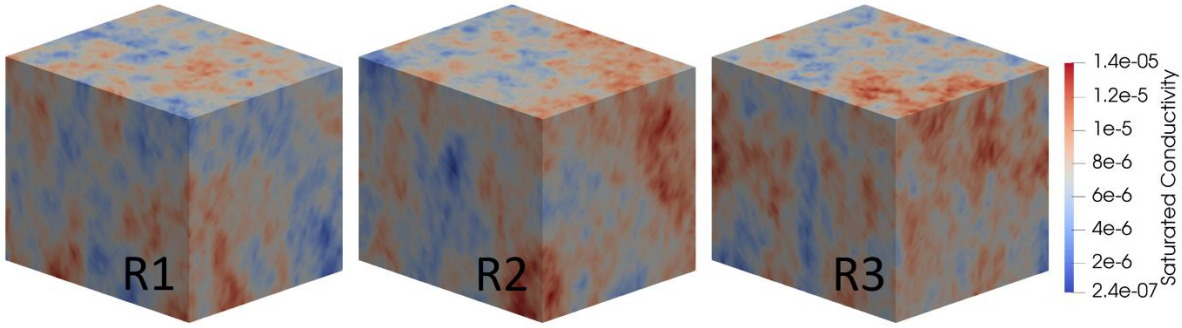

Figure 6.9: Generated 3-D fields for simulations R1, R2 and R3

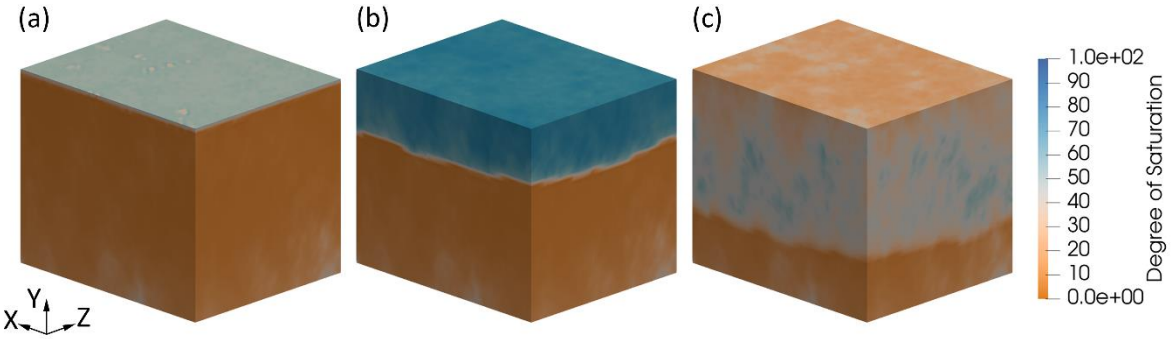

Figure 6.10: Wetting front movement of R1 over time (a) 0.5 hours, (b) 6 hours when surface application is stopped, and (c) 28 hours

As described above, a tracer was applied to the surface to allow for the front position to be more visible when excavating. The degree of saturation necessary for the tracer to be activated was not reported, so here it is assumed to be 85 %. In doing so, the positions for which the tracer was activated were able to be plotted by tracking the degree of saturation of each node. Figure 6.11 shows the simulated patterns of tracer activation at 28 hours. The top row of Figure 6.11 shows the positions of tracer activation in blue for R1, R2 and R3, where the bottom row shows the tracer activation as a translucent layer to visualise the variability in the full domain. It is clear that the presence of heterogeneity in the soil has resulted in non-uniform flow within the soil mass. Finally, Figure 6.12 shows a comparison between the experiment and simulations for a set of 2-D slices of the domain, highlighting the fingered nature of water movement. Additional slices and full tracer plots can be found in Appendix A. The given cross-sections are from selected planes chosen to illustrate the typical behaviour observed within the three-dimensional domain. Figure

6.12 illustrates the ability of the model to match the unstable flow behaviour seen experimentally in terms of the finger shapes and distribution. For all three cases, the range of simulated values lie inside the experimental range, showing a good estimation of tracer activation depth. For all realisations in Figures 6.12, it can be seen that the front has penetrated slightly less into the domain than is experimentally observed. This is a result of the stochastic nature of the model and highlights the need for multiple simulations. As the generated fields are random, it is entirely possible to attain results from both ends of the spectrum. It is possible that tuning of the model would have led to resulting depths that have a closer fit, but this would require straying away from the values reported in the literature. It is more important to match the finger characteristics, such as their distribution, which the model is able to demonstrate well. Table 6.2 contains further details related to Figure 6.12, indicating a good fit between the experimental and numerical maximum, minimum and average tracer activation depths.

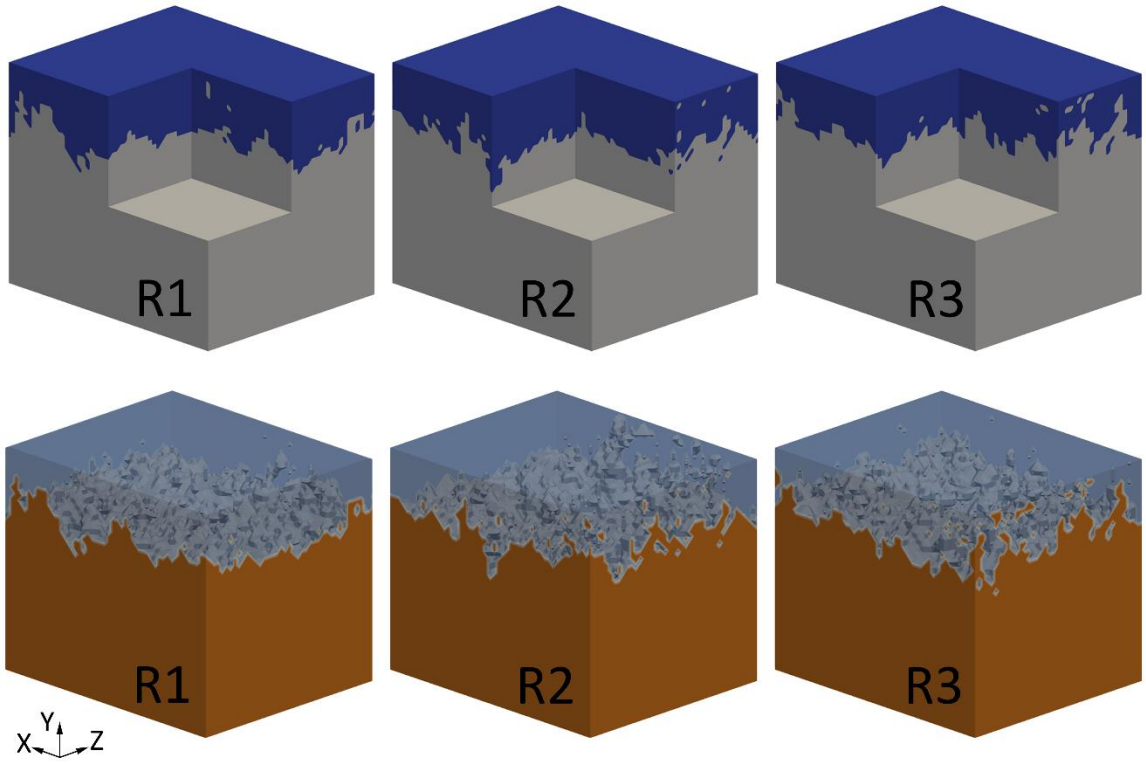

Figure 6.11: (Top row) Tracer activation at 85 % degree of saturation for R1, R2, and R3. (Bottom row) Translucent tracer activation to see variability in activation position and fingered shapes

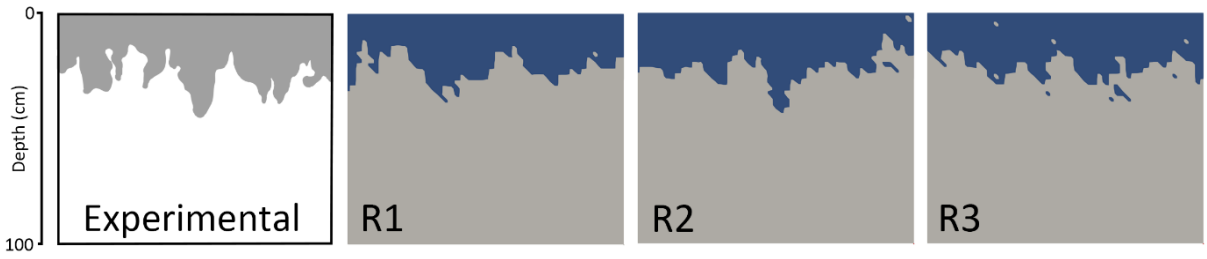

Figure 6.12: Comparison between experimental and numerical results in terms of slices for R1, R2 and R3

It is clear that the model is able to show the observed preferential movement of water through more permeable regions of the soil. The fields shown in Figure 6.9 portray these regions and, as would be expected, their morphology matches that of the faster draining regions shown Figure 6.10 (c). Due to the localised distribution of flux, it is observed that -initially- the water penetrates the soil where the conductivity is highest, forming fingered flow along paths of least resistance. The driest area on the surface in Figure 6.10 (a) is a result of the conductivity being low as seen in the

field of R1 in Figure 6.9. As such, a lower flux is applied and it remains dry for longer. Similarly, the same area will drain much more slowly due to the decreased ability of water to move through the medium. This is confirmed by Figure 6.10 (c), where the same region has the highest degree of saturation on the surface at the end of the simulation. An alternate analysis was run without the inclusion of locally distributed flux, showing that it affected only the short-term variation in the response, with the long-term response not being significantly impacted. This is seen in Figure 6.13, where the left hand column shows the application of uniform flux, the right hand column shows the application of flux following Section 6.3, and (a-c) represent 0.2, 1.4, and 5.5 hours respectively. As highlighted by the surfaces in (a-c), applying the flux in this manner allows for the local effects of surface variability to be accounted for, whereas the uniform application only accounts for the global variations in material heterogeneity.

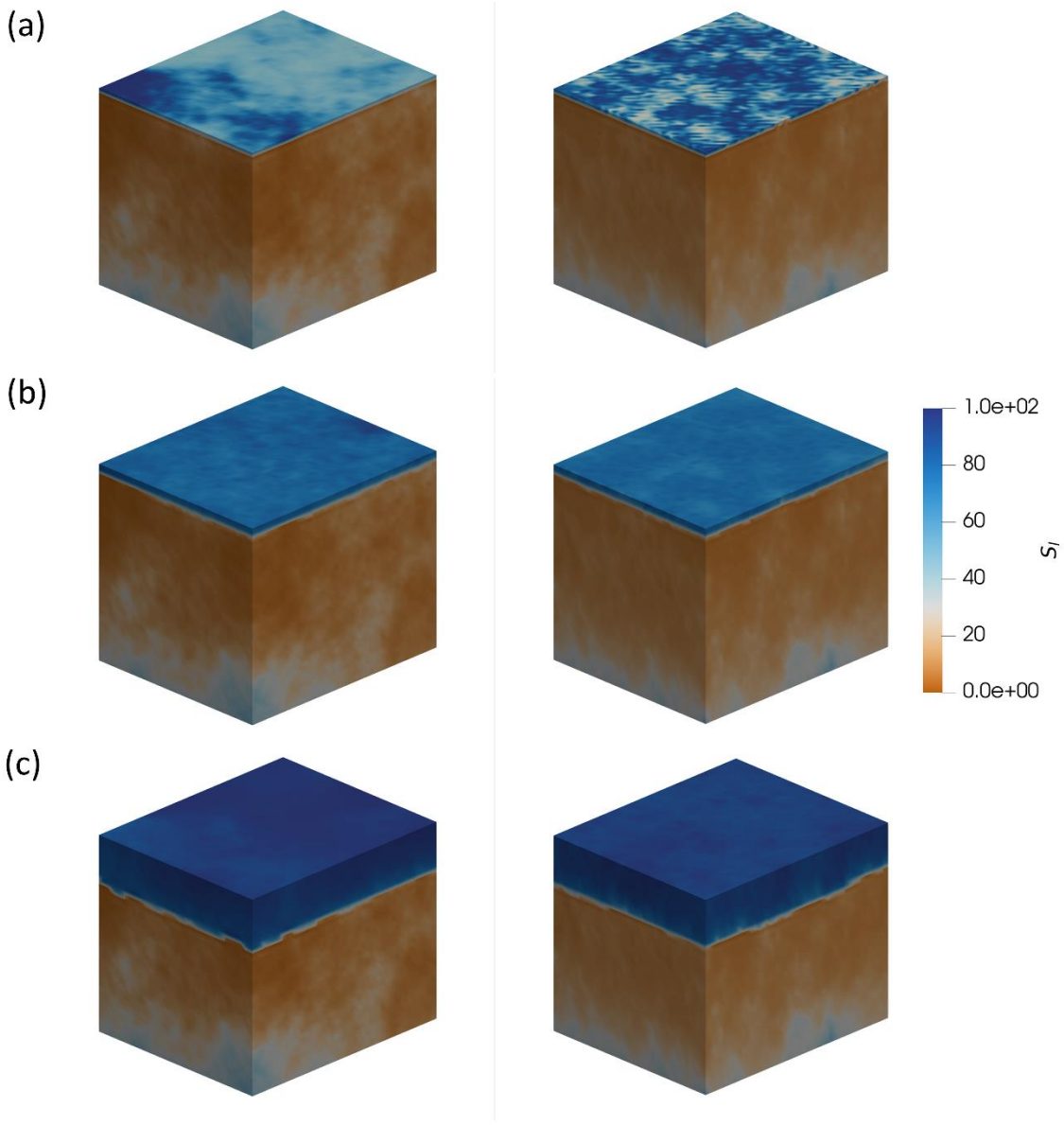

Figure 6.13: Illustration of variable flux application where the left hand column is the results of a uniformly applied flux, the right hand column results from the variable application of flux, and (a-c) are the times 0.2, 1.4, and 5.5 hours respectively

Table 6.2: Maximum, minimum and mean tracer activation depth for experimental and numerical results

	Max Depth m	Min Depth m	Mean Depth m
Experimental	0.4634	0.1286	0.2852
R1	0.3857	0.1128	0.2417
R2	0.3745	0.1226	0.2529
R3	0.3865	0.1625	0.2531

To highlight the fully 3-D nature of the presented analyses, profiles of flux were computed laterally and vertically at 7 hours. Figure 6.14 shows the computation of the lateral flux for a slice at depth 0.2 m within the advancing wetting front, highlighting that the movement of the advancing wetting front is influenced by the lateral conductivities of the medium. This is further seen in Figure 6.15, which shows the computation of the flux over a vertical slice at z = 0.5 m. The orientation of the arrows near to the wetting front interface are not regular, and show that the invading fluid phase is not propagating uniformly in the vertical direction. Whilst the order of magnitude of the lateral fluxes is smaller than that seen vertically, they do affect the motion of the fluid phase, requiring a fully 3-D analysis to gain a richer description of the problem.

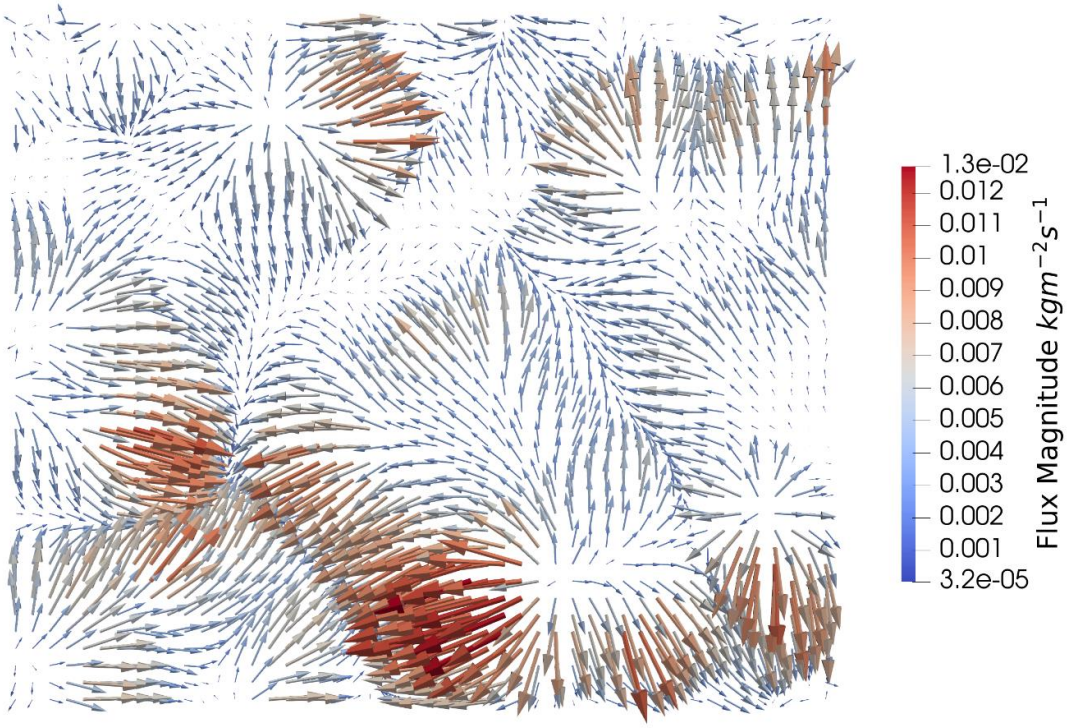

Figure 6.14: Computation of lateral flux over a slice of the domain within the advancing wetting front 7 hours into the simulation

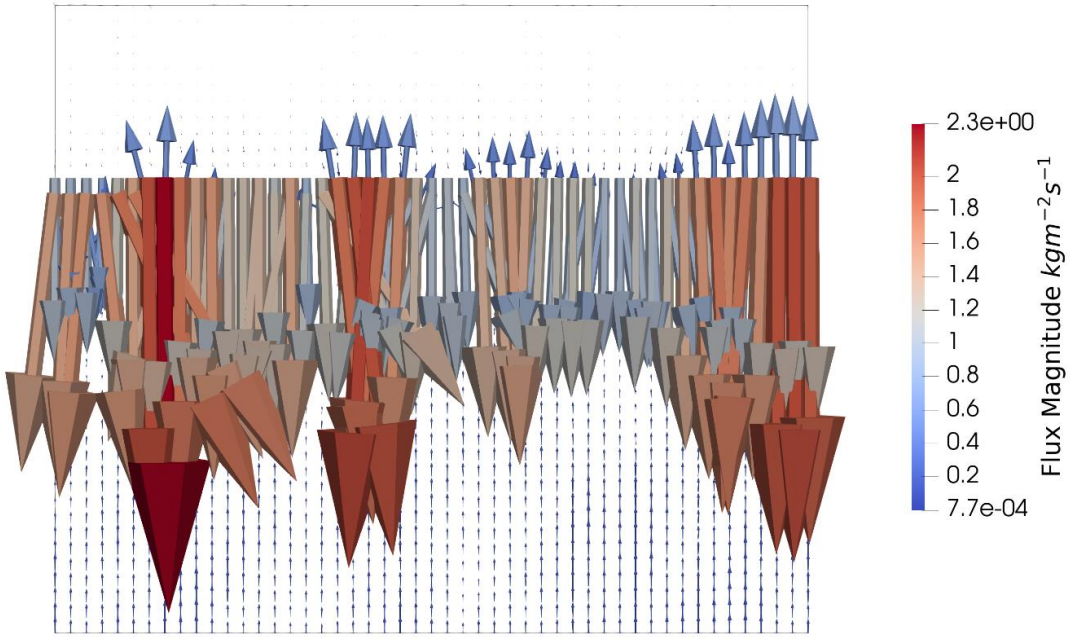

Figure 6.15: Computation of vertical flux over a slice of the domain within the advancing wetting front 7 hours into the simulation

Whilst the overall front movement appears quite regular in Figure 6.10, the build-up and movement of water in certain zones behind the wetting front is what distinguishes the model from those which portray uniform flow. It is noted that regions of soil which are less permeable see a greater build-up of water as the movement of the wetting front is retarded due to the lower conductivity. These areas correspond to higher degrees of saturation and relate to regions at which the assumed tracer activation value is more likely to be satisfied. Similarly, the vertical fluxes computed in Figure 6.15 show the strong preferential nature of the flow due to the stronger intensity of the wetting front movement in certain regions.

6.5 Uncertainty analysis of finger depths

Monte Carlo (MC) approaches are frequently used to calculate statistical and associated convergence metrics. These methods usually employ relatively large numbers of realisations (hundreds) and, as such, are computationally expensive (Jiang et al., 2014; Nikolaidis et al., 2013; Seçgin & Kara, 2019). It is challenging to determine, a priori, the number of simulations required to achieve convergence of a particular statistical variable to a desired tolerance. Whilst some investigators have considered such methods (Lerche and Mudford 2005), they generally require an undetermined number of runs to establish the required statistical values. An advantage of the correlated Whittle-Matérn method used for the present work is that far fewer simulations are required to reach convergence of stochastic measures than for MC analyses. This is demonstrated below, where the mean, maximum, and minimum finger depths obtained from increasing numbers of analyses are considered. The procedure used to compute the statistical values of these parameters is described in the following section, and can also be found in a recent paper presented by the author and colleagues (Ricketts et al. 2023). The parameters of interest are assumed to follow a normal distribution, such that confidence intervals for the given parameters can be calculated. This is the confidence level that the population mean of the mean, maximum, and minimum finger depths lie within a range of calculated values.

The confidence interval (CI) can be calculated as follows

$$\mathrm{CI} = \bar{x} \pm \bar{t}\frac{\sigma}{\sqrt{n_s}} = \bar{x} \pm \bar{t}\mathrm{SE} \tag{6.5}$$

where $\bar{x}$, σ and n_s indicate the sample mean, sample standard deviation and sample size respectively, and SE is the standard error. The parameter $\bar{t}$ is the t-score which is used as a correction for the sample size (Campbell 2021). Thus, CI is determined and this gives the level of certainty that the population mean $\bar{x}^P$ lies within the following range

$$\bar{x} - t_1 \mathrm{SE} \leq \bar{x}^P \leq \bar{x} + t_2 \mathrm{SE} \tag{6.6}$$

where t_1, t_2 are the lower and upper t-scores respectively. The calculated sample mean values, standard deviations, mean normalised standard deviations, SE, and t-scores t_1 and t_2 are given in Table 6.3 for each investigated parameter in the 12 simulations. The final calculated ranges are given in Table 6.4.

Table 6.3: Sample mean, standard deviation, mean normalised standard deviation, t-scores t_1 and t_2, and standard error SE for the mean, minimum, and maximum finger depths of the 12 simulations

	Mean (m)	Standard deviation (m)	Mean normalised standard deviation (m)	SE	t1	t2
Mean finger depth	0.25315	0.00558	0.02205	0.00167	6.78633	5.34001
Minimum finger depth	0.15657	0.02127	0.13586	0.00619	6.82084	4.67182
Maximum finger depth	0.35249	0.02518	0.07144	0.00730	5.24333	4.86392

Table 6.4: Final calculated ranges of the 12 simulations

	Lower bound (m)	Upper bound (m)
Mean finger depth	0.24182	0.26206
Minimum finger depth	0.11436	0.18549
Maximum finger depth	0.31424	0.38521

For each individual parameter, the certainty in the calculated intervals was calculated as $\geq$ 99.7% with 12 simulations or more. When comparing the experimental depths given in Table 6.2 against those Table 6.4, it is clear that the calculated ranges are within the tolerance of the experimental data. The convergence of the confidence intervals can be seen in Figure 6.16, where a sufficiently high level of confidence is achieved for each of the investigated metrics. This study suggests the number of realisations required to achieve statistical significance may be determined by conducting successive analyses until the required confidence level is achieved. Finally, it is also possible to show the evolution of the confidence interval for a desired level of confidence. Here, 95% confidence was chosen, and the confidence interval was calculated as the number of simulations increased. This is seen in Figure 6.17, which shows that the interval stabilises as the number of observations is increased. In addition, we infer that the number of simulations required to achieve relatively high confidence levels is much fewer than required by the comparable MC process. Figure 6.18 shows box and whisker plots of tracer activation depth for the experimental profile and the 12 simulations, further highlighting the ability of the model to represent the physical problem and lie within the experimental range.

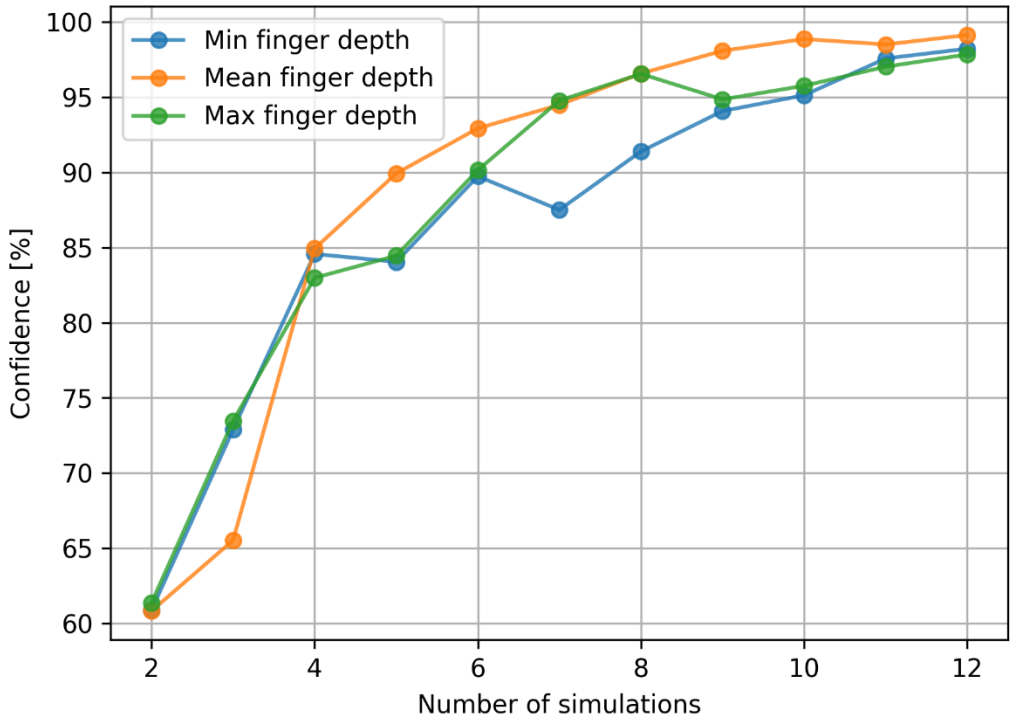

Figure 6.16: Confidence in the calculated intervals of the investigated parameters of finger depth

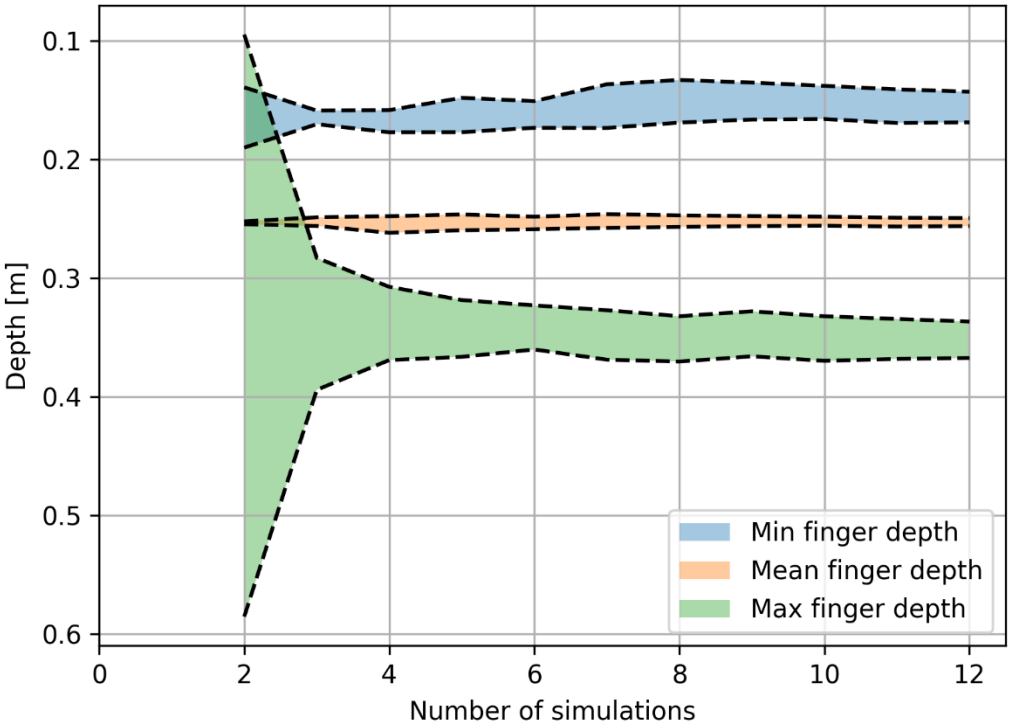

Figure 6.17: Convergence of confidence intervals for finger characteristics at 95% confidence

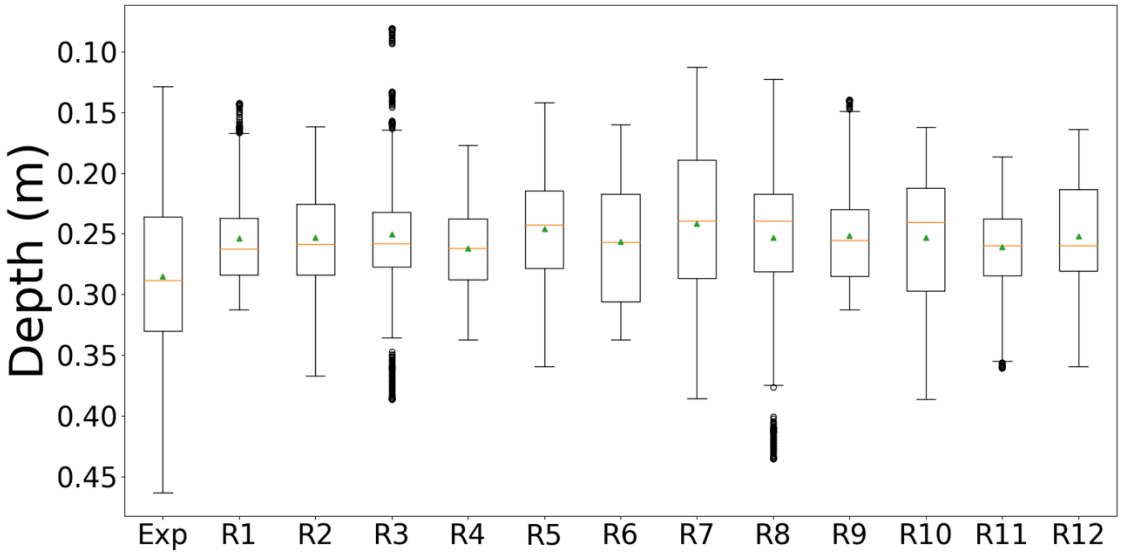

Figure 6.18 Box and whisker diagrams of tracer activation depth for the experimental data and 12 simulations conducted. The green triangle represents the mean value of tracer activation depth

In situations where numerical results may vary considerably between different stochastic realisations (e.g. finger penetration depths and patterns), it may be beneficial to be able to determine a range of values for the relevant parameter with a high, and quantifiable, degree of certainty. For complex field scale analyses, such as 3-D slope stability problems, the presented approach would enable the quantification of risk of failure to a defined degree of certainty.

6.6 Conclusions

The heterogenous nature of soils has a strong influence on hydrological flow processes. In order to describe non-uniform moisture flow in soils using the finite element approach, it is necessary to represent spatial variations in the material properties that govern flow behaviour. The random field from which such properties are derived should have an intrinsic correlation length, otherwise the associated simulations are not objective with respect to mesh grading. The Gaussian random field approach provides an effective means of representing a field of material properties for a body of soil. A proper simulation of the soil transport processes also requires spatial variations of boundary infiltration properties to be considered. The new method proposed of using overlapping kernel functions covering the infiltration boundary provides an effective means of simulating non-uniform inflow into a domain

whilst maintaining mass balance at all times. This allows for the material heterogeneity seen at the surface of the domain to have influence over the applied boundary condition, as would be the case in real life systems.

Incorporating the new field generation algorithm into a 3-D finite element model for moisture transport allows non-uniform flow behaviour within soil bodies to be simulated in a realistic manner. A set of validation analyses that considered moisture infiltration into a layer of sandy loam showed that the new proposed model is able to represent the characteristics of non-uniform moisture flow into and through a heterogeneous body of soil with good accuracy. The method achieves relatively high confidence levels for characteristic stochastic variables with relatively few simulations (e.g. a 99.7% CI with 12 realisations). In addition, the method allows a required level of confidence -for a set of stochastic variables- to be determined by undertaking successive analyses until the desired value is achieved. Due to its inherent computational convenience and efficiency, the proposed technique is suitable for large field-scale problems, where the statistical significance can be determined with a comparatively low number of simulations.

6.7 References

Akin, C., & Rottke, L. (2011). The Home Orchard Handbook: A Complete Guide to Growing Your Own Fruit Trees Anywhere.

Alletto, L., & Coquet, Y. (2009). Temporal and spatial variability of soil bulk density and near-saturated hydraulic conductivity under two contrasted tillage management systems. Geoderma, 152(1–2), 85–94. https://doi.org/10.1016/j.geoderma.2009.05.023

Campbell, M. J. (2021). Statistics at Square One (12th ed.). John Wiley & Sons.

Carminati, A., Vetterlein, D., Weller, U., Vogel, H.-J., & Oswald, S. E. (2009). When Roots Lose Contact. Vadose Zone Journal, 8(3), 805–809. https://doi.org/10.2136/vzj2008.0147

Eshel, A., & Beeckman, T. (2013). Plant Roots: The Hidden Half (A. Eshel & T. Beeckman, Eds.). CRC Press. https://doi.org/10.1201/b14550

Ghodrati, M., Ernst, F. F., & Jury, W. A. (1990). Automated Spray System for Application of Solutes to Small Field Plots. Soil Science Society of America Journal, 54(1), 287–290. https://doi.org/10.2136/sssaj1990.03615995005400010046x

Jiang, S. H., Huang, J., Griffiths, D. V., & Deng, Z. P. (2022). Advances in reliability and risk analyses of slopes in spatially variable soils: A state-of-the-art review. Computers and Geotechnics, 141. https://doi.org/10.1016/j.compgeo.2021.104498

Jiang, S. H., Li, D.-Q., Asce, M., Zi, ;, Cao, J., Chuang, ;, Zhou, B., Phoon, K.-K., & Asce, F. (2014). Efficient System Reliability Analysis of Slope Stability in Spatially Variable Soils Using Monte Carlo Simulation. https://doi.org/10.1061/(ASCE)GT.1943

Kool, D., Tong, B., Tian, Z., Heitman, J. L., Sauer, T. J., & Horton, R. (2019). Soil water retention and hydraulic conductivity dynamics following tillage. Soil and Tillage Research, 193, 95–100. https://doi.org/10.1016/j.still.2019.05.020

Lang, A., & Potthoff, J. (2011). Fast simulation of Gaussian random fields. https://doi.org/10.1515/MCMA.2011.009

Lerche, I., & Mudford, B. S. (2005). How Many Monte Carlo Simulations Does one Need to do? ENERGY EXPLORATION & EXPLOITATION ·, 23, 405–427.

Li, D.-Q., Xiao, T., Zhang, L.-M., & Cao, Z.-J. (2019). Stepwise covariance matrix decomposition for efficient simulation of multivariate large-scale three-dimensional random fields. Applied Mathematical Modelling, 68, 169–181. https://doi.org/10.1016/j.apm.2018.11.011

Liu, Y., Li, J., Sun, S., & Yu, B. (2019). Advances in Gaussian random field generation: a review. In Computational Geosciences (Vol. 23, Issue 5, pp. 1011–1047). Springer International Publishing. https://doi.org/10.1007/s10596-019-09867-y

Mualem, Y. (1976). A new model for predicting the hydraulic conductivity of unsaturated porous media. Water Resources Research, 12(3), 513–522. https://doi.org/10.1029/WR012i003p00513

Mubarak, I., Mailhol, J. C., Angulo-Jaramillo, R., Ruelle, P., Boivin, P., & Khaledian, M. (2009). Temporal variability in soil hydraulic properties under drip irrigation. Geoderma, 150(1–2), 158–165. https://doi.org/10.1016/j.geoderma.2009.01.022

Nikolaidis, E., Norouzi, M., Mourelatos, Z., & Pandey, V. (2013). Managing the Computational Cost of Monte Carlo Simulation with Importance Sampling by Considering the Value of Information. SAE International Journal of Materials and Manufacturing, 6(3), 2013-01–0943. https://doi.org/10.4271/2013-01-0943

Posadas Ay, D. A. N., Tannh, A., Panepucci, H., & Crestana, S. (1996). Computers and electronics in agriculture Magnetic resonance imaging as a non-invasive technique for investigating 3-D preferential flow occurring within stratified soil samples. In Computers and Electronics in Agriculture (Vol. 14).

Ricketts, E. J., Freeman, B. L., Cleall, P. J., Jefferson, A., & Kerfriden, P. (2023). A Statistical Finite Element Method Integrating a Plurigaussian Random Field Generator for Multi-scale Modelling of Solute Transport in Concrete. Transport in Porous Media. https://doi.org/10.1007/s11242-023-01930-8

Roininen, L., Huttunen, J. M. J., & Lasanen, S. (2014). Whittle-matérn priors for Bayesian statistical inversion with applications in electrical impedance tomography. Inverse Problems and Imaging, 8(2), 561–586. https://doi.org/10.3934/ipi.2014.8.561

Seçgin, A., & Kara, M. (2019). Stochastic Vibration Analyses of Laminated Composite Plates via a Statistical Moments-Based Methodology. Journal of Vibration Engineering & Technologies, 7(1), 73–82. https://doi.org/10.1007/s42417-018-0077-5

Simpson, D., Lindgren, F., & Rue, H. (2012). In order to make spatial statistics computationally feasible, we need to forget about the covariance function. Environmetrics, 23(1), 65–74. https://doi.org/10.1002/env.1137

van Genuchten, M. Th. (1980). A Closed-form Equation for Predicting the Hydraulic Conductivity of Unsaturated Soils. Soil Science Society of America Journal, 44(5), 892–898. https://doi.org/10.2136/sssaj1980.03615995004400050002x

Vergara, R. C., Allard, D., & Desassis, N. (2018). A general framework for SPDE-based stationary random fields. http://arxiv.org/abs/1806.04999

Wang, Z., Lu, J., Wu, L., Harter, T., & Jury, W. A. (2002). Visualizing Preferential Flow Paths using Ammonium Carbonate and a pH Indicator. Soil Science Society of America Journal, 66(2), 347–351. https://doi.org/10.2136/sssaj2002.3470

Wang, Z., Wu, L., Harter, T., Lu, J., & Jury, W. A. (2003). A field study of unstable preferential flow during soil water redistribution. Water Resources Research, 39(4). https://doi.org/10.1029/2001WR000903

Chapter 7

Three-dimensional unsaturated flow in heterogeneous water repellent soil

7.1 Introduction

It has been established that material variability can lead to distinct unstable hydraulic behaviour, and that it is prominent in soils due to their largely varied display of spatial heterogeneity. This behaviour is amplified when the wettability of the medium is non-uniform, specifically if the soil becomes hydrophobic. When soil is naturally water repellent (WR), there is often spatial variability of wettability (Woods et al. 2007), such that a network of preferential flow paths is created. As water infiltrates, the water repellent regions will impede flow, resulting in preferential pathways in regions where the soil is wettable. This leads to highly preferential fingered flow, and can result in rapid movement of contaminants, or induce localised erosion due to the fingered behaviour of the flow. The WR properties of soil can be induced artificially through addition of chemicals, via contamination, and as the consequence of natural processes such as wildfire, which can lead to events such as flash flooding. With the risk of extreme weather events increasing, and associated rise in wildfire induced water repellency, the need to model and predict the behaviour of soil transport processes is ever more necessary.

Many modelling approaches for soil typically consider the soil to be fully wettable, making it challenging to have a representation of the material that is consistent with non-wettable behaviour. Similarly, even with constitutive components that can represent hydrophobicity, the heterogeneity of the soil properties need to be accounted for. Previous modelling studies of fingered flow in water repellent soils have considered hysteresis as a driving factor for the flow dynamics (Nieber 1996; Nieber et al. 2003). The effects of hysteresis were brought into the solution of the mass balance equation, based on Richard's equation, and was seen to be the cause of persistence in fingered flow. The heterogeneity of the medium was also considered by Ritsema et al. (1998), where the formation and recurrence of fingers were simulated based on a numerical solution comprising coupled water and air flow

in a 2-D domain. The authors claimed that the spatial variability of wettability, inferred by a non-homogenous medium, will cause fingers to become permanent preferential pathways. In many cases, it is seen that the heterogeneity of the medium is an influential factor in flow related process as in soil, suggesting that -in addition to the material variability- the wettability of the medium should also vary spatially.

In this chapter, an investigation into the modelling of hydrophobic soil is presented. As in the previous chapter, local spatial variations in material parameters are accounted for using Gaussian random fields. The development of the model is first discussed, and then applied to replicate a field scale experiment carried out by Lipsius & Mooney (2006). A key component is the relationship used to represent the saturation-capillary pressure relationship responsible for defining water entry pressures. For wettable soil, as in Chapter 6, this can be done with the standard van Genuchten relation (van Genuchten 1980). For hydrophobic soil, this is not applicable; thus, an alternative and its use with random fields is employed (Foroughi et al. 2022). Results from 3 representative simulations are presented based on the provided experimental data, and quantified using confidence interval calculations as in the previous chapter.

Section 7.2 presents the numerical developments of the model from that of Chapter 6; Section 7.3 presents the simulated tracer tests and quantifies the observed infiltration profiles based on the dye coverage percentage; and Section 7.4 gives the main conclusions of the chapter.

7.2 Modelling considerations

7.2.1 Constitutive relations to account for hydrophobicity

In the previous chapter, the saturation-capillary pressure relationship used was the standard van Genuchten relation. Whilst this is suitable for considering wettable unsaturated soil, the behaviour of hydrophobic soil may not be so well represented. The difficulty in representing the relationship between suction and degree of saturation lies in the water entry pressure (WEP) needed for a fluid to enter into the soil. If the soil is not WR, then the WEP is in the positive suction range. On the other hand, for hydrophobic soil, the WEPs needed for infiltration can be in the positive pore-water pressure range (i.e. negative suction). This can be seen in Figure 7.1 (after Zheng et al., (2021)), where conceptual illustrations of soil water retention

curves for fine and coarse grained soils, as well as WR soils, are shown. The van Genuchten relation cannot account for the positive pore-water pressures that are characteristic of WR soil, suggesting that the approach of Chapter 6 will need to be modified for these layers.

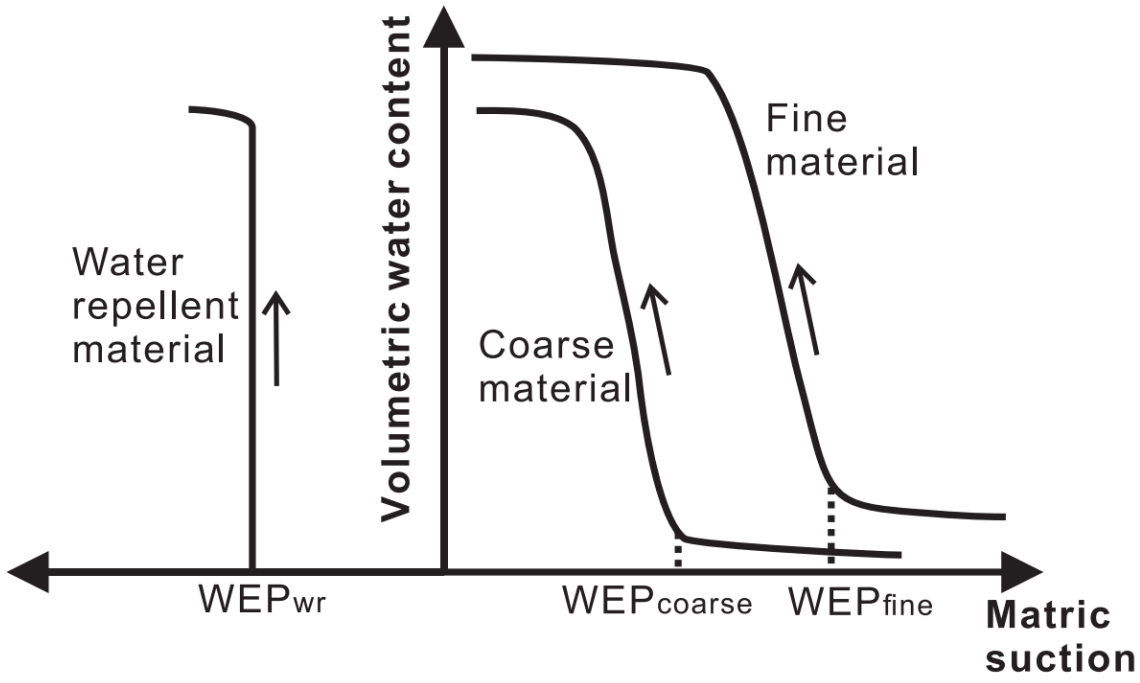

Figure 7.1: Illustrative example of the soil water retention curves resulting from soils with differing unsaturated hydraulic properties (reproduced from Zheng et al., (2021)*)*

Recently, Foroughi et al., (2022) proposed a new saturation-capillary pressure relationship for porous media of varying wettabilities, which proved to be more flexible and accurate than existing relationships. The relationship matched well against a wide range of experimental data, measured from rocks, soil, bead and sand packs, and manufactured fibrous materials. This relationship can be written as

$$S_l = \left(\frac{1}{\pi}\left(\frac{\pi}{2} - \tan^{-1}\left(\frac{s-A}{B}\right)\right)\right)^{\frac{1}{C}} \quad (7.1)$$

where A is an indicator of wettability, B is the curvature index, and C is the saturation exponent. Whilst there is no fundamental basis for the functional form, the given parameters of the function can be interpreted physically. The most important in this study is A, where $A > 0$ indicates a wettable or hydrophilic medium, $A < 0$ indicates hydrophobicity, and $A \approx 0$ suggests a mixed-wettable medium where locally the

medium could be hydrophobic or hydrophilic. The effects of changing the non-dimensional equivalent of parameters A, B, and C can be seen in Figure 7.2. The given relation (7.1) is adopted in the current study based on its ability to represent the saturation-pressure relationship observed in a wide range of mixed wettable media.

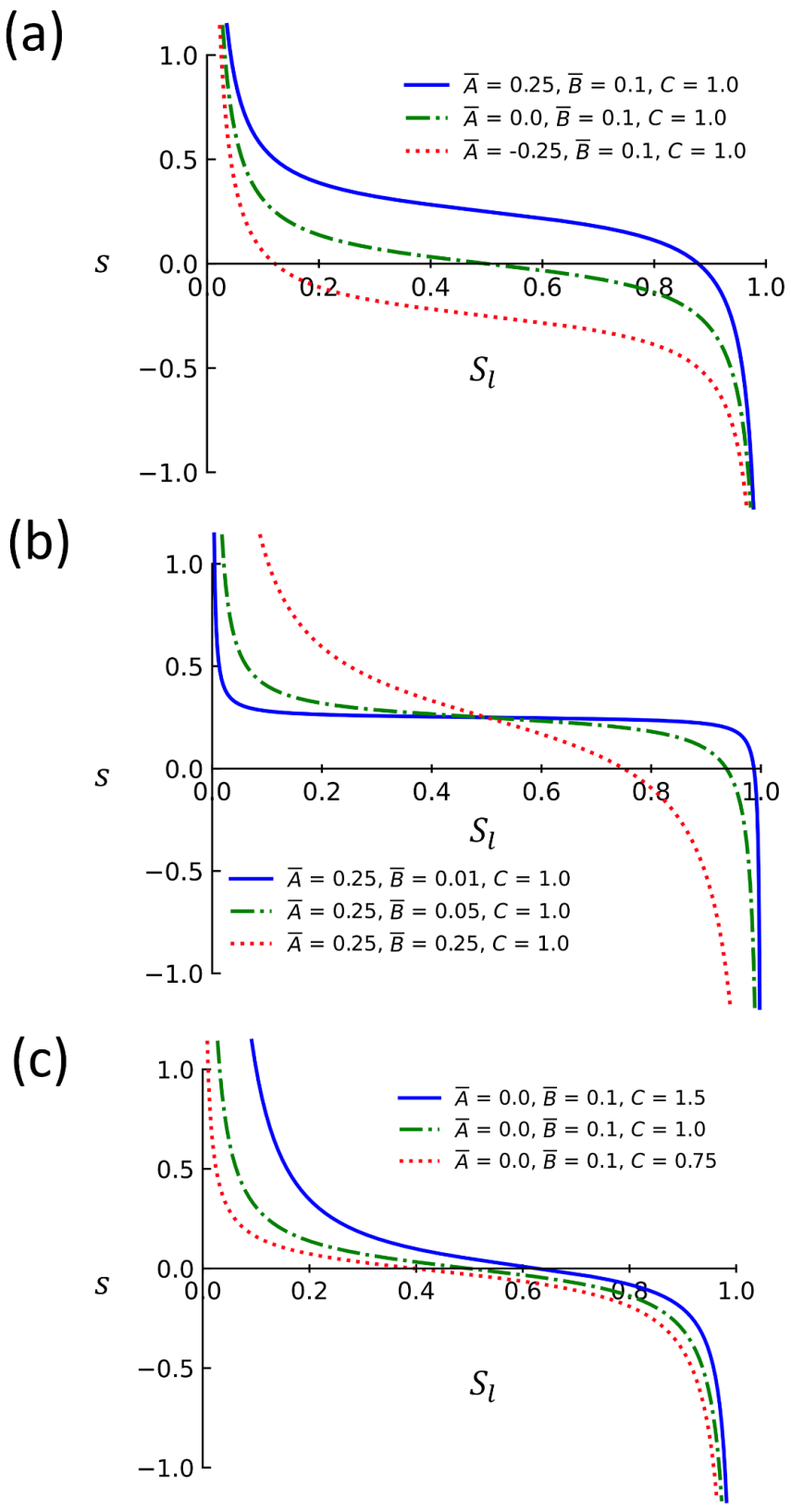

Figure 7.2: Effects of fluctuation in parameters: (a) $\bar{A}$, (b) $\bar{B}$, and (c) C, where the dimensionless form was attained using Leverett J-function scaling (Leverett 1941) *(reproduced from* Foroughi et al., (2022)*)*

7.2.2 Random field application

As in the previous chapter, random fields generated through the solution of equation (4.30) are applied to represent material heterogeneity. A key difference here is that the domain is now considered as a layered domain, where layers can be defined by material type. The layers could be used to define soil types, such as sand or clay, or levels of wettability. It is noted that the model is capable of accounting for different soil types coupled with differing wettabilities. However, here the focus is on the description of layers defining levels of wettability for a given soil type as this is the case for the practical example that follows in Section 7.3. To describe the application of correlated random fields under this configuration, the domain given in Figure 7.3 is considered, where a soil mass is illustrated with a water repellent top layer (a) and a wettable sublayer (b).

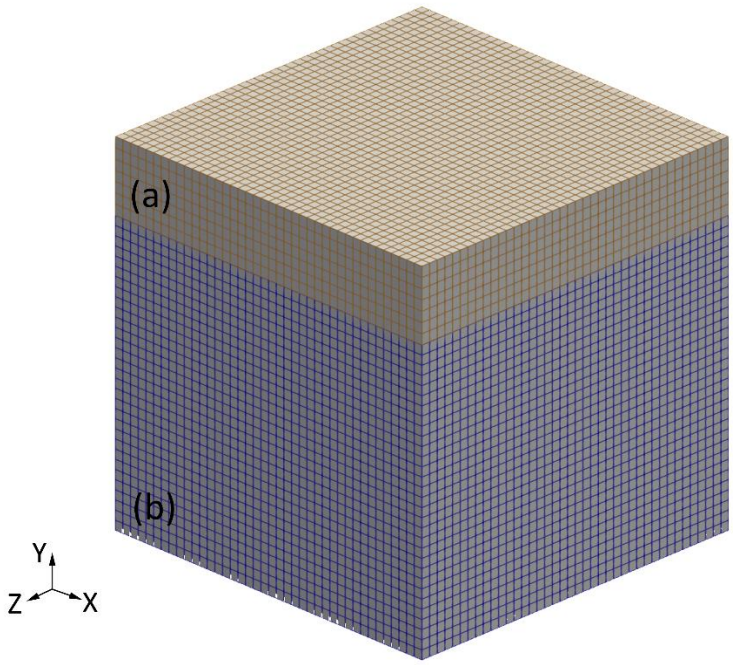

Figure 7.3: Illustrative domain for layered hydrophobic soil, composed of a water repellent layer (a), and a wettable layer (b)

In Chapter 6, the generated Gaussian random fields were chosen to directly represent the saturated conductivity K_s, and the van Genuchten parameters α_{vg} and n_{vg}, leading to spatial variation in the SWRC and conductivity relations amongst other constitutive components. In wettable regions, such as Figure 7.3 (b), the model behaves in the same way as that described in the previous chapter. However, for the

hydrophobic layer, Foroughi et al.'s, (2022) relationship is adopted and spatial variation in the water retention function is accounted for by varying the parameters of equation (7.1), namely A, B, and C, throughout the layer.

Along with these parameters, K_s is also varied as in the wettable layers, which allows the unsaturated conductivity to vary spatially as before. The relative coefficient of unsaturated hydraulic conductivity K_r for the WR layer is calculated as in the previous chapter -equation (6.4)- and is parameterised using the particle size terms d_{60} and d_{10}, the grain sizes for which 60% and 10% are finer respectively. This is related through n_{vg} in the relationship for K_r, such that

$$n_{vg} = \frac{C_1}{\log_{10} C_u} + 1 \tag{7.2}$$

where C_1 is a model constant suggested as 1.07, and C_u is the coefficient of uniformity, defined as

$$C_u = \frac{d_{60}}{d_{10}}. \tag{7.3}$$

Thus, in addition to K_s, A, B, and C, the terms d_{60} and d_{10} are varied spatially, such that n_{vg} can be calculated for each spatial position.

The model is set up so that an arbitrary number of random fields can be generated with different spatial distributions assigned to material parameters. Here, the correlation structure of the particle size data is assumed to follow that of K_s, meaning that larger particle sizes relate to more conductive regions, where the contrary is also true.

7.2.3 Transition region

Often when modelling layered materials, the interface between layers is assumed to be uniform, such that the material is not mixed (Romano et al. 1998; Liu et al. 2015; Ahmadi et al. 2016). In many cases, it is not representative of the problem to have such idealised transitions between phases (Heilig et al. 2003), especially when the layers represent the same material. For naturally induced WR, be it through wildfire or contamination, the level of repellency is generally very high near the surface and decays with depth (Woods et al. 2007). One approach to represent this is to assume a localised mixture of wettable and WR regions being present within a representative elementary volume, with the ratio of each fraction varying with depth. As the model

considers discrete water retention functions in each layer, by interpolating between them based on the depth in a predefined transition zone, a combined water retention function can be calculated. This, for example, could be based on an assumption that the ratios of each fraction within a transition layer varies with depth. Similarly, other material parameters can be varied that are shared between the zones, such as K_s and n_{vg}.

To illustrate this, consider a 10 cm soil column composed of two layers of 5 cm length whose saturated conductivity varies between layers. A large transition zone of 8 cm is assumed to illustrate the effects, starting at $x_{\text{tmin}} = 1$ cm depth, and ending at $x_{\text{tmax}} = 9$ cm depth. Initially, two random fields f_1, f_2 are generated for the full domain, and scaled based on the desired material properties of each layer. The interpolated field is then calculated as

$$f_I = (1 - \vartheta) f_1 + \vartheta f_2 \tag{7.4}$$

where ϑ is the sigmoid function, calculated as

$$\vartheta = \frac{1}{1+e^{\omega \epsilon(x)}} \tag{7.5}$$

where ω is a smoothness coefficient of the sigmoid function, and ϵ varies with a given depth x. By varying the value of ω, the smoothness of the sigmoid function can be changed, such that sharp or slow transitions between f_1 and f_2 can be achieved. The sigmoid function is chosen to allow a smooth transition between layers, an assumption which is addressed at the end of this section. Equation (7.5) is largely dependent on ϵ, and is calculated using a simple linear interpolation based on the beginning and end of the transition zone as

$$\epsilon(x) = \frac{(x - x_{\text{tmin}})(\epsilon_{\text{max}} - \epsilon_{\text{min}})}{x_{\text{tmax}} - x_{\text{tmin}}} + \epsilon_{\text{min}} \tag{7.6}$$

where ϵ_{max}, ϵ_{min} define the range of the sigmoid function which is used for interpolation. This is illustrated in Figure 7.4, where (a) shows the sigmoid function, and (b) gives f_1, f_2, and the interpolated field f_I. Here, $\omega = 0.5$ and ϵ_{max}, ϵ_{min} are defined as 10 and -10 respectively, which ensures an initially smooth transition between the fields to avoid sharp jumps in the interpolated parameter. This is done with the intention of the region being easier to visualise, purely for illustrative purposes. In reality, this region could be much smaller (Heilig et al. 2003).

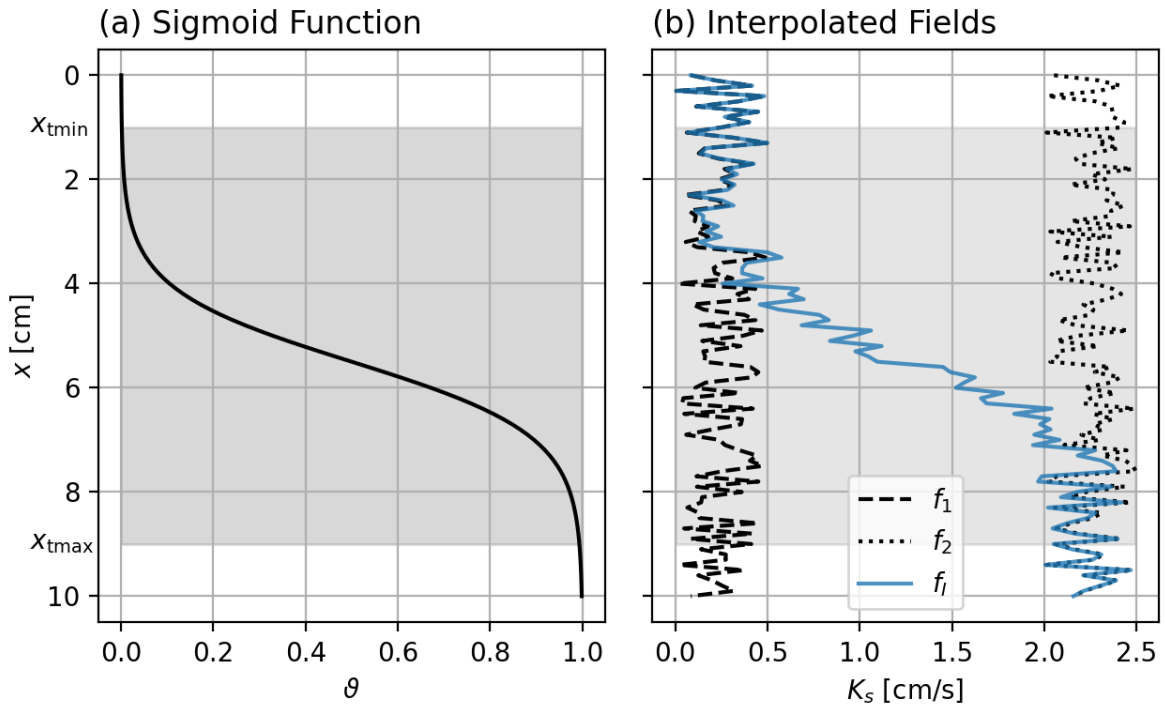

Figure 7.4: Field interpolation regime where (a) gives the change in ϑ with depth, and (b) shows the interpolation between the two fields f_1, f_2 based on ϑ. The fields are transitioned over the grey region of x_{tmin} to x_{tmax}

The same procedure can be carried out for interpolation between the SWRCs for each layer, and is demonstrated in the following section.

Through this method, the transition region and its smoothness can be defined in an intuitive manner, such that the transition between layers with depth follows the path of a sigmoid function. However, this does assume that the transition will be smooth between layers, with uncertainty not been accounted for. In reality, it is likely that the transition from one layer to another does not happen at the same rate across the domain. This would be better represented by gaussian processes to define the region of depths of the transition zone.

7.3 Application: field infiltration experiment

With the details of the model's developments relative to Chapter 6 having been discussed, it is applied to a heterogeneous soil mass. The main difference here, as compared to the example considered in Chapter 6, is the representation of distinct flow behaviour due to the presence of water repellency.

Specifically, the field experiment carried out by Lipsius & Mooney (2006) is considered, where field infiltration experiments were carried out to investigate the influence of water repellency on flow patterns. The soil considered was contaminated with heavy metals (Chromium and Arsenic) due to the leaching of wood preservatives from impregnated wood located at an industrial site in Bavaria, Germany. Also, it was observed that polycyclic aromatic hydrocarbons had entered the topsoil from tar-oils (Hopp et al. 2006). Both result in alterations of chemical and physical soil properties, and resulted in strong water repellency and the prevention of plant growth. The soil physical properties, including bulk density, particle size data, and the saturated conductivity, are given in Table 7.1.

Table 7.1: Soil properties of the experimental site, where n_O is the number of observations (Lipsius and Mooney 2006)

Depth (cm)	n_O	Bulk density (g cm^-3)	>2mm (%)	630 μm-2mm (%)	200-630 μm (%)	63-200 μm (%)	<63 μm (%)	K_s (cm d^-1)
1 - 10	18	1.51	0.4	40.6	48.6	9.9	0.6	500
10 - 19	20	1.56	0.5	37.4	53.5	8.1	0.4	664
19 - 22	4	1.55	0.7	30.9	58.7	8.9	0.5	745
22 - 50	1	1.71	0.2	26.2	62.6	10.6	0.4	2500
>50	20	1.6	0.1	23.5	65.5	10.7	0.4	850

In both the spring and summer, dye tracer infiltration experiments were conducted such that the effects of seasonal variability could be quantified. 2 m^2 plots were chosen based on the absence of vegetation and a non-sloped surface, as it was thought that the level of contamination should be higher in these regions. Brilliant Blue FCF (C.I. 42090) of concentration 2 g L^{-1} was irrigated manually on two plots, using a watering can, with different irrigation rates applied to each: (i) 10 mm/h, and (ii) 14.3 mm/h. The rate of application varied due to ponding and surface runoff. The following day, the plots were excavated to a depth of 1 m, and the profiles were photographed for later image analysis. Ten profiles were sampled in roughly 40 cm intervals for each plot. As the seasonal variability was found to be negligible between

the spring and summer (Lipsius and Mooney 2006), the following analysis considers the case of 10 mm/hr irrigation rate in the summer period.

As stated in Section 7.2, random fields are employed to represent variation in K_s, A, B, C, α_{vg}, n_{vg}, d_{60}, and d_{10}, where the variability of the given parameters propagate throughout the relations used in calculating the constitutive components of the model, similar to that seen in Figure 6.2. The mean and standard deviations of the given parameters are based on the experimental data reported in Lipsius & Mooney (2006) where available, with their values being presented in Table 7.2. To avoid non-physical scaling of the fields, the assumed normal distributions of the parameters are capped at 3σ from the mean. As the correlated structure of the soil was not given, l was assumed to be 0.2 m vertically, and 0.1 m in both horizontal directions to account for local variations in material properties.

Table 7.2: Random field mean and standard deviation values

		K_s	α_{vG}	n_{vG}	d_{60}	d_{10}	A	B	C
WR	*Mean*	6.74E-05	-	-	0.3471	0.1215	-50	500	1
	Standard Deviation	1.34E-05	-	-	0.0062	0.0008	750	3	0.05
Wettable	*Mean*	1.58E-04	4.513E-04	3.2278	-	-	-	-	-
	Standard Deviation	5E-05	7.00E-05	0.0732	-	-	-	-	-

The most influential spatially varying parameter for the WR layer is A, as this is what largely controls the WEP and the level of water repellency that a given position in the domain has. Larger variations in A across the domain will lead to more unstable flow, with strongly pronounced fingering behaviour. It also allows for positive pore-water pressures to be assigned as WEPs, as suggested by Figure 7.1.

The simulation domain is defined as a 1 m cube, discretised by regular hexahedral elements of element length 2 cm (with appropriate convergence checks undertaken), and can be seen in Figure 7.5 (a) along with the applied boundary conditions. The rainfall flux boundary condition was applied using the variable application method outlined in the previous chapter. Based on the numerical formulation, the remaining boundaries are assumed insulated. An initial timestep of 10 seconds was used,

which was then increased to 100 seconds when the wetting front became less sharp, this approach was found to yield convergent results. The layered configuration of the soil is seen in Figure 7.5 (b), where the transition zone spans 15 cm of the domain, labelled in red.

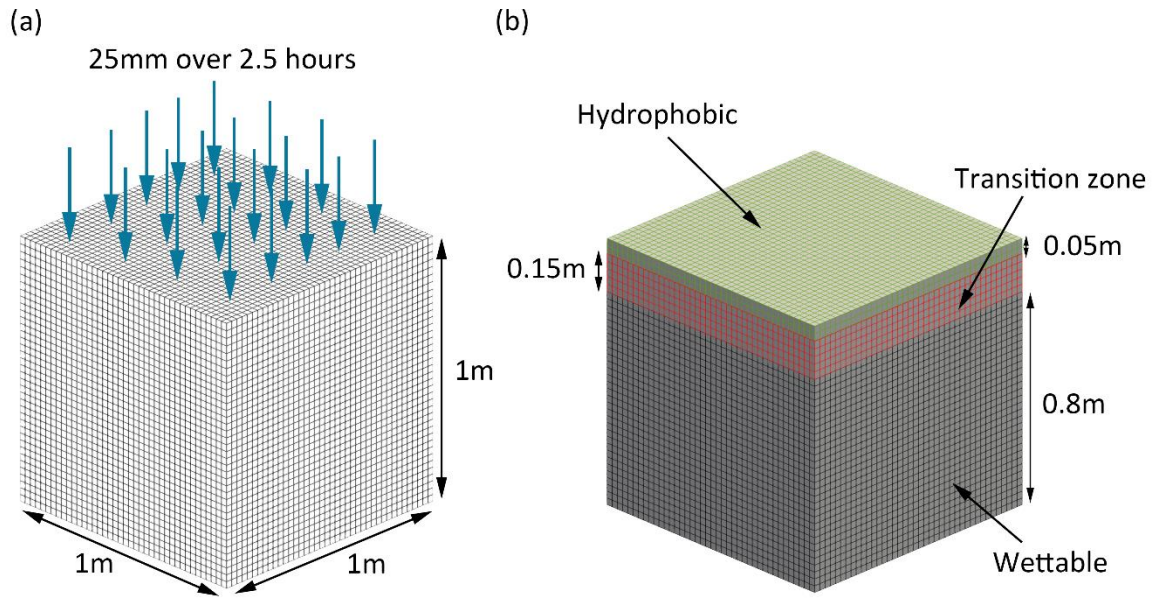

Figure 7.5: Numerical domains showing (a) the mesh and applied boundary conditions, and (b) the size and type of soil layers

The top part of the soil is assumed fully hydrophobic, and the bottom section assumed wettable. The size of the water repellent and transition layers were based on the top 10 cm of the experimental plots displaying signs of heterogeneous water repellency (Lipsius and Mooney 2006). The heterogeneity in the level of WR is due to the way that the solutes would have infiltrated the soil over time, permeating in a non-uniform manner. As they move preferentially though the soil, this renders certain regions as more WR than others, with the overall level decreasing from the surface with depth. By assuming a sigmoidal variation with depth in the fractions of wettable and WR soil at any particular location, the variation in WR with depth is represented. Similarly, coupling this with the random fields for local spatial variations in the hydraulic behaviour allows for the heterogeneity of both the material and level of hydrophobicity to be represented. Figure 7.6 gives example fields based on the values given in Table 7.2 for K_s and n_{vg}, where the variations in the mean values reflect the changing properties in the transition zone between layers.

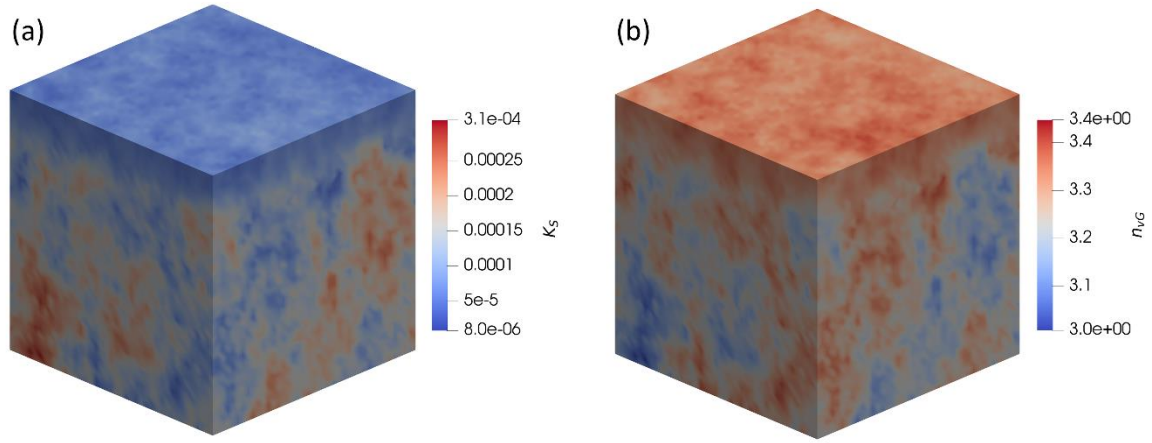

Figure 7.6: Random field realisations to highlight the transitional behaviour for (a) K_s and (b) n_{vg}

As mentioned above, the SWRC for the transition region is calculated as an interpolation between the respective layers' constitutive relation. At a depth of 0.05 m, the WR relationship is used to compute the degree of saturation, as highlighted in Figure 7.7 (a). As the depth increases through the transition zone to 0.2 m, the curve is interpolated, finally being fully WR as the depth reaches 0.2 m. The curves presented in Figure 7.7 (a) are the SWRCs based on the mean values given in Table 7.1, where in the model, the presented curves for a given depth will strongly vary as in Figure 7.7 (b) (for a depth of 0.0125 m). In Figure 7.7 (b), curves were plotted based on the full variation of parameters given in Table 7.1 to show the banding of the SWRC that is present in the model for a specific depth in the transition zone. It is seen that the WR section exhibits more variability compared to the wettable section.

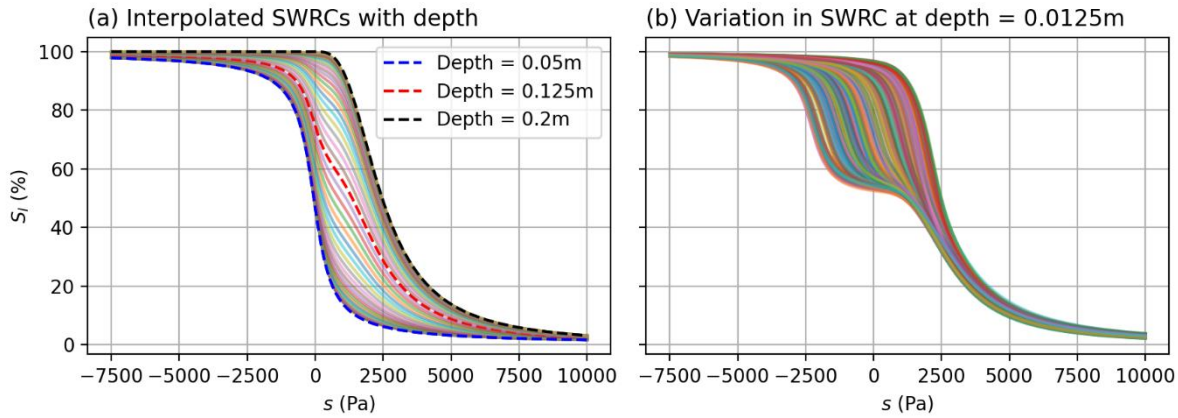

Figure 7.7: Illustration of (a) Average interpolated SWRCs between the wettable and water repellent soil, where the dashed line at a depth of 0.125 m is the middle of the transition zone; and (b) the variation in the interpolated SWRC at depth of 0.125 m

7.3.1 Tracer simulation results

Three representative simulations R1, R2, and R3 are presented from a set of 20 analyses. These are illustrative of the full behaviour that the model can represent, which is then quantified in Section 7.4.2 based on the dye coverage. For further results from the simulations conducted, see Appendix B. Figure 7.8 shows the wetting front movement at 1000, 6000, 10000, and 98000 seconds for R2, where both R1 and R3 had similar responses.

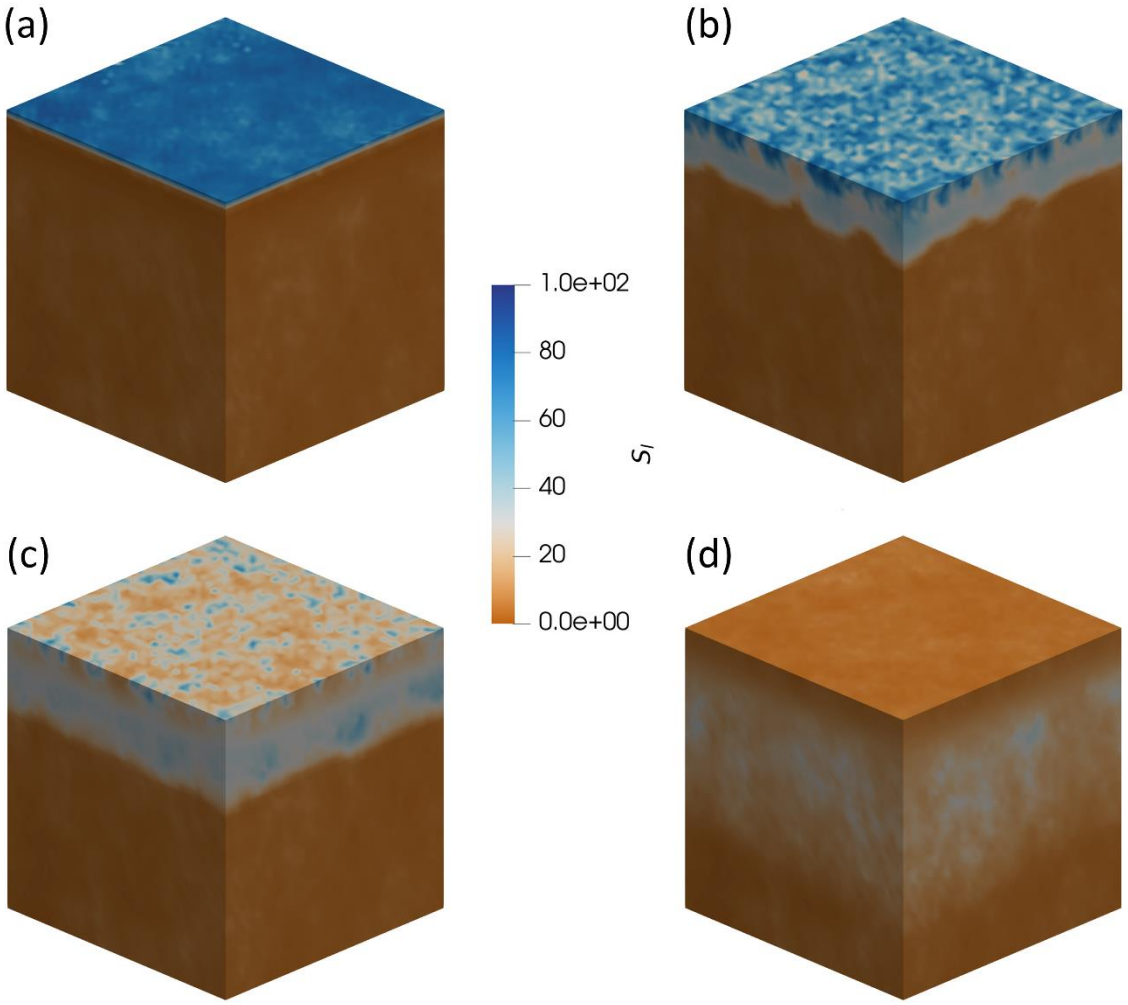

Figure 7.8: Wetting front movement in terms of the degree of saturation S_l of R2 at (a) 1000, (b) 6000, (c) 10000, and (d) 98000 seconds

As described above, a tracer applied to the surface allowed for imaging of the infiltration profiles. The degree of saturation necessary for the tracer to be visualised was assumed to be 35%, and this allowed the tracer position to be tracked at each node throughout the simulations. In the previous chapter, the degree of saturation required for the tracer to be visible was much higher. Wang et al. (2003) had difficulties visualising the applied tracer, hence a higher value was chosen to reflect this difficulty. When conducting similar experiments for WR soil, Lipsius & Mooney (2006) reported no difficulties in the tracer being observed, and as such, it can be assumed that a lower degree of saturation was necessary for it to be seen.

Figure 7.9 shows the tracer activation regions for R1, R2, and R3 at the final timestep of 26.5 hours, where the top layer shows this in blue. The bottom layer

shows this same area as a translucent layer to visualise the non-uniform nature of the tracer regions.

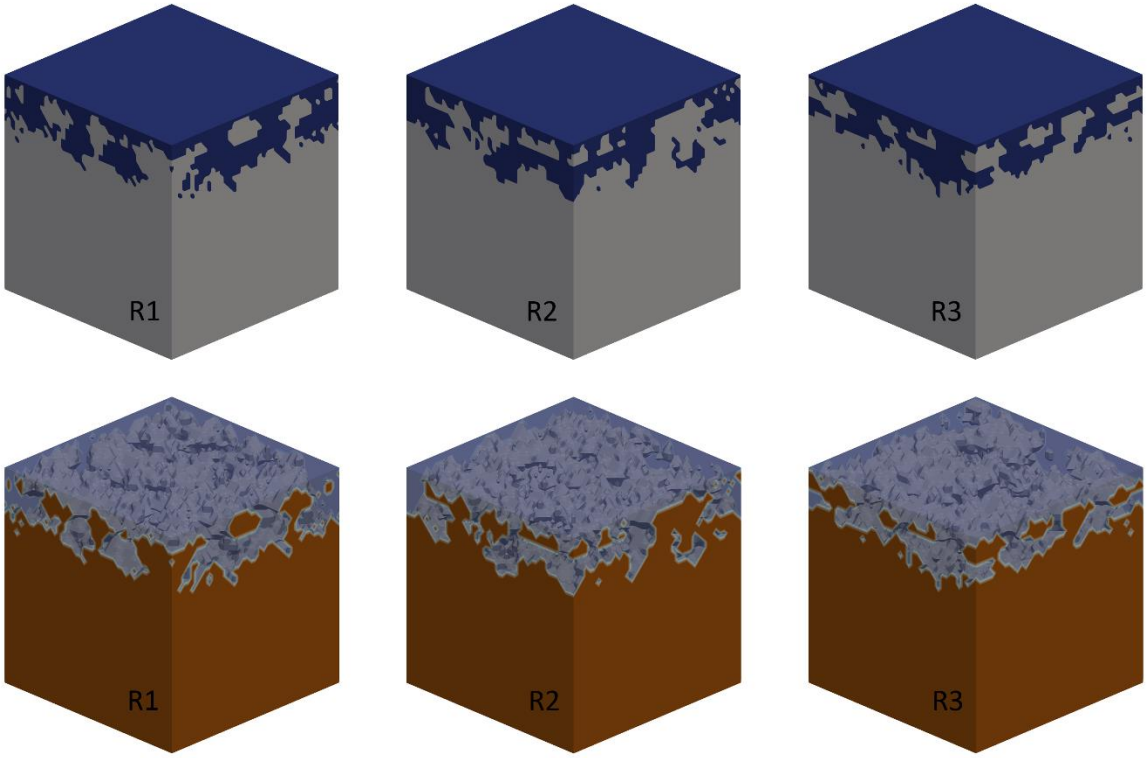

Figure 7.9: Tracer activation regions at 35% S_l for R1, R2, and R3, where the top row shows the tracer in blue, and the bottom shows the same as a translucent layer

Finally, slices were taken from the three presented simulations to compare with the experimental images based on the dye coverage percentage and the spatial distribution of the fingered shapes. These can be seen in Figure 7.10, were (a), (b), and (c) are the experimental images, and (d), (e), and (f) are the numerical slices taken from R1, R2, and R3 respectively. The specific slices that are presented were chosen based on their ability to match well with the limited experimental data, whilst also being representative of the overall model response. Further slices can be seen in Appendix B. The percentage of dye coverage can be used to compare the results of the numerical simulations against the experimental observations, indicating the ability of the model to represent the overall wetting front response.

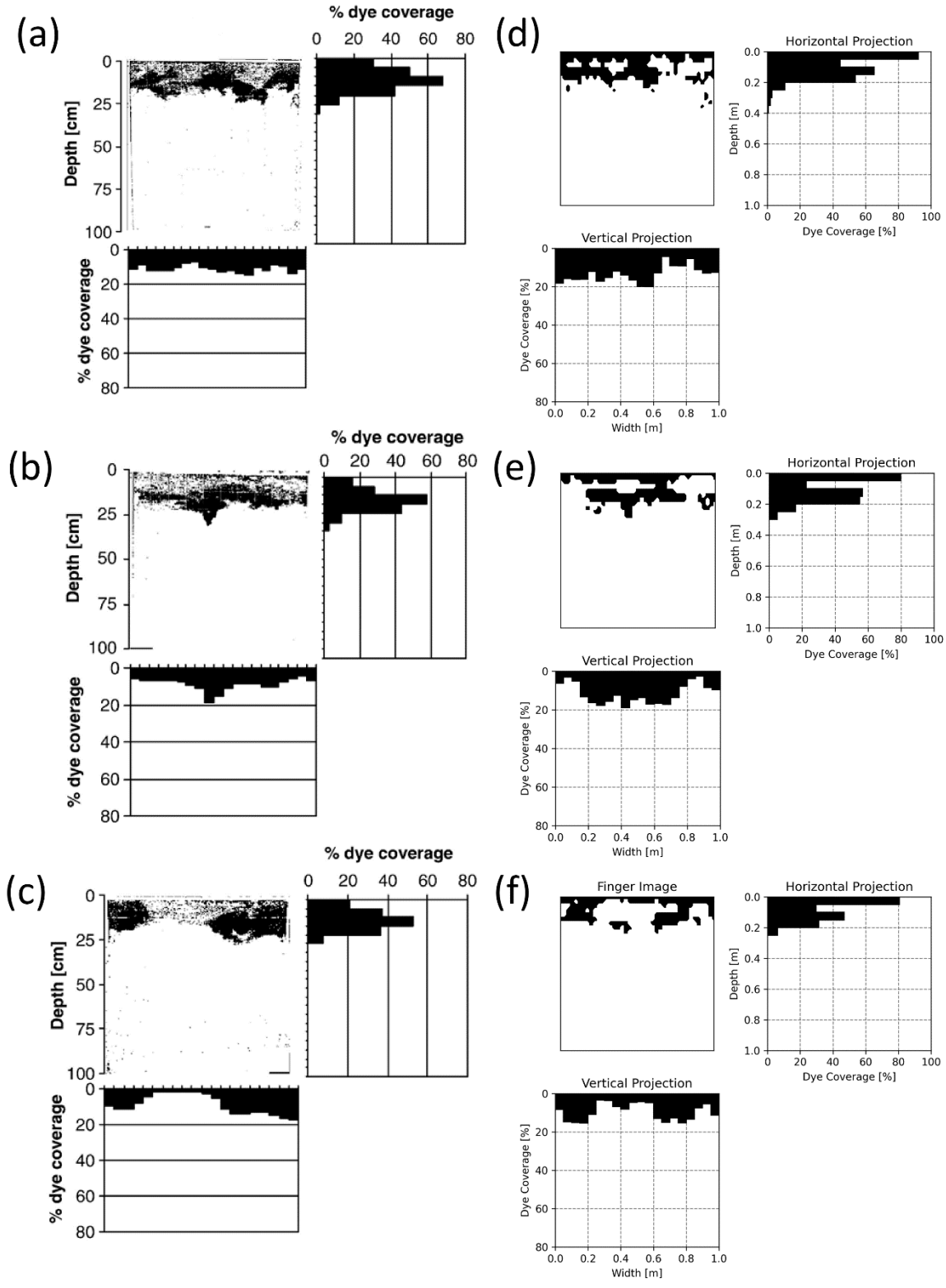

Figure 7.10: Tracer activation regions and their respective dye coverages for vertical and horizonal projections, where: (a-c) are the experimental observations (Lipsius and Mooney 2006)*, and (d-f) are slices of R1, R2, and R3 respectively*

It is clear that the range of responses seen in Figure 7.10 (a-c) are well represented by the numerical results (d-f). This is in terms of the spatial distribution of tracer activation and dye coverage percentages. One aspect that does not compare well is the large dye coverage in the first bar of the horizontal projection of (d-f), relating to tracer activation in the surface elements. This is a result of the fluid being forced into the body based on the numerical process of applying a flux. In reality, and as stated in the original study, water would infiltrate at a variable rate, where runoff and ponding were observed. To account for this in the model, additional layers of elements could be introduced to the surface acting as a region for pressure to build up to represent a ponding layer. In this way, water would infiltrate at a pace directly dictated by the material, as opposed to the numerical scheme. On the other hand, the dye coverage of the later regions is well within the experimental range, showing an adequate match with the test data. Importantly, the model exhibits infiltration patterns that have the same characteristics as those observed in the experiments. To further improve the results, the model could be tuned to selected input material properties. The presented results are based on the available experimental material data, but with careful parameter tuning, it is possible that a better fit could be achieved in terms of the tracer profiles. This could allow for uncertainty in experimental readings to be taken into account, rather than assuming there is no associated error.

As the model will behave similarly to that of Chapter 6 in wettable regions, similar conclusions on the water movement can also be made. Namely that less conductive regions see a larger build-up of water as it struggles to pass through, suggesting the increased chance that the tracer will be active in said region. Conversely, the more conductive regions allow for faster passage of the wetting front, taking the tracer with it. Similarly, Figure 7.8 (b) illustrates the change in hydraulic response through the domain as the transition region is reached. The flow becomes more diffuse due to the smaller variation in the SWRC for the wettable regions. This is in agreement with the assumed behaviour of the medium, such that the water repellency should induce highly unstable flow that becomes more stable as it transitions into the wettable layer.

Due to the water repellency in the top layer, there is a period of time in the simulation for which the pore water pressure builds up at the surface. This lasts until the WEP is

achieved for a given position, after which the water enters the soil body in a preferential manner. This can be seen in Figure 7.11, where (a) shows the build-up of fluid at the surface, (b) shows a time after the WEP has been surpassed, and (c) gives a point further into the simulation to show the water passing through the hydrophobic layer in a fingered fashion.

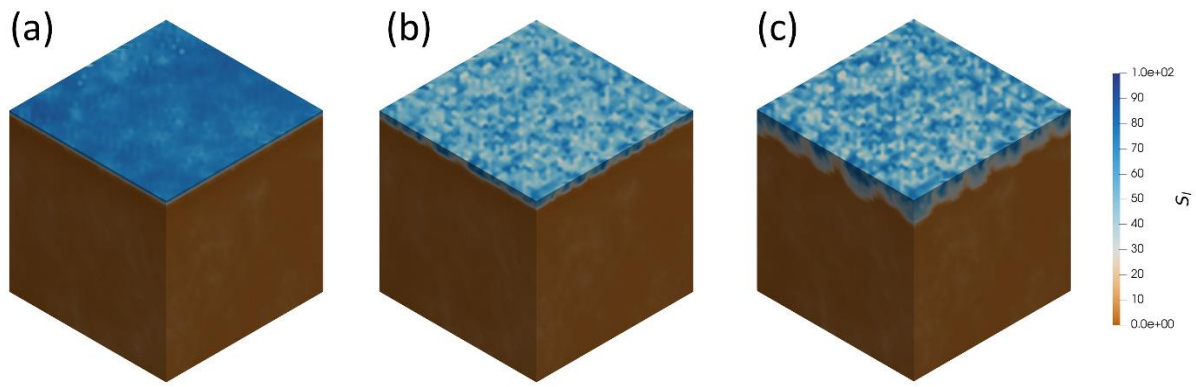

Figure 7.11: Illustration of (a) a build-up of degree of saturation on the surface due to hydrophobicity at 16 minutes, (b) the fluid phase infiltrating after the pore water pressure has surpassed the water entry pressure at 33 minutes, and (c) a later stage to show the resulting fingered nature of the flow at 1 hour

The results given in (a-c) are at times 16 minutes, 33 minutes, and 1 hour respectively. It is clear that in (a), the degree of saturation -and therefore porewater pressure- is much higher than that of the later plots. As the WEP is dependent on the SWRC at the given position on the surface, which vary based on the material variability, the water begins the infiltrate at different times causing highly unstable behaviour. The flux is still being applied in (a-c), showing that once the WEP has been surpassed, the applied fluid will infiltrate into the soil body with less resistance.

To further illustrate the unstable flow patterns that result from the material variability, the flux of the invading fluid was computed for slices within the wetting front. These are seen in Figure 7.12, where (a) is the lateral flux within the wetting front at depth 0.2 m, and (b-c) shows the flux for perpendicular vertical slices at z = 0.5 m and x = 0.5 m for 2.5 hours into the simulation. As in the previous chapter, the fully 3-D nature of the flow is observed, where strong lateral fluxes are highly influential over the movement of the fluid phase.

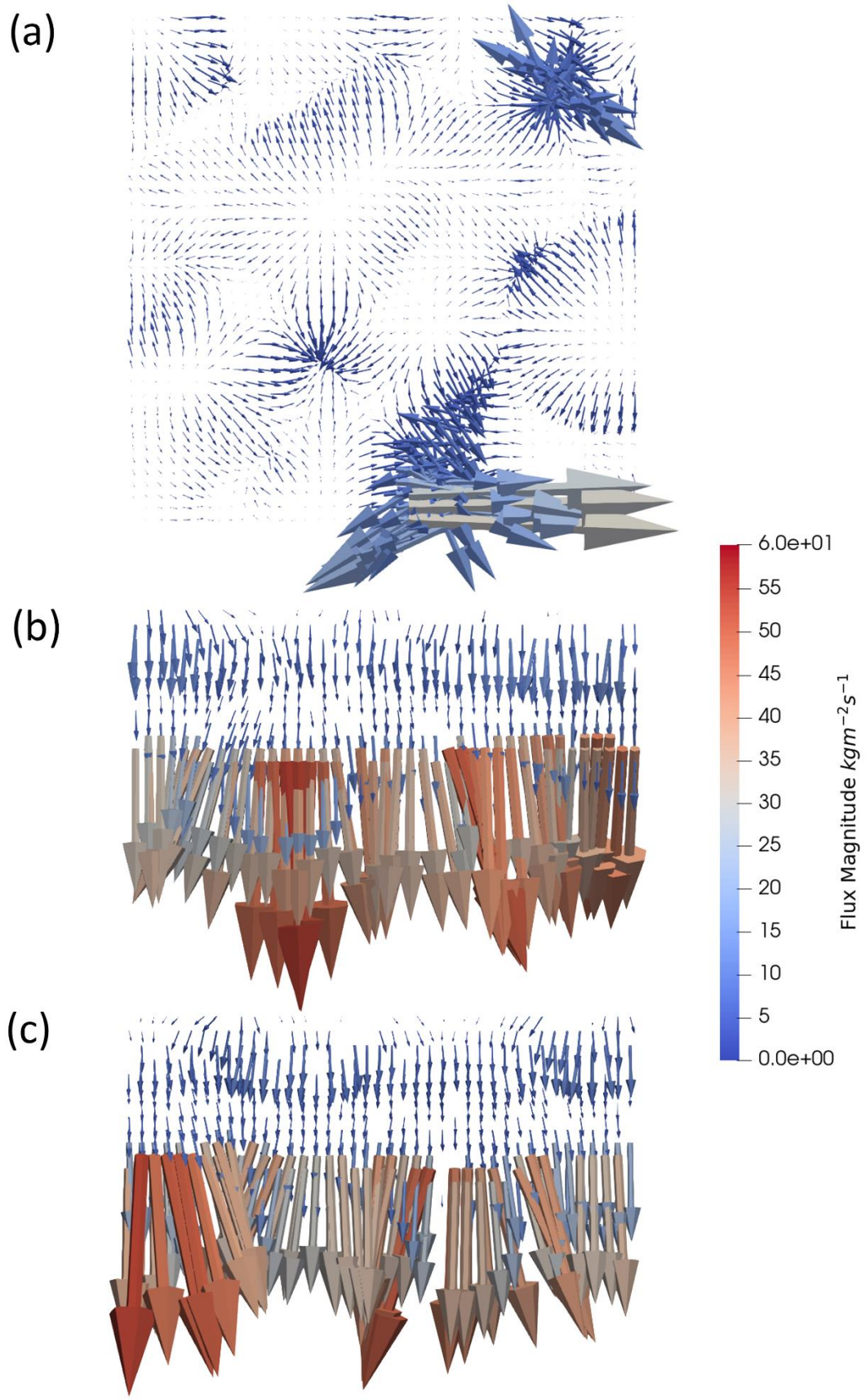

Figure 7.12: Computation of the (a) lateral and (b-c) vertical flux profiles at 2.5 hours, where (b) and (c) are perpendicular

7.3.2 Uncertainty analysis of dye coverage

To quantify the how representative the presented simulations are in terms of the global behaviour of the model, the same approach as in Chapter 6 is applied here, taken from Ricketts et al. (2023). In Chapter 6, the finger depths were characterised in terms of their confidence intervals, showing that for a very low number of simulations, a high confidence can be attained for a certain calculated range. The evolution of the confidence interval for a given level of confidence was then also shown. Here, the dye coverage is quantified in both the horizontal and vertical projections as this can be directly compared with the experimental data. In total, 20 simulations were conducted to assess the level of confidence. For each simulation, slices from each element layer in the x and z plane were taken of the tracer activation solution such that the maximum, minimum and mean dye coverage of the histograms could be collected for each slice. For a given simulation, this resulted in 80 slices due to the chosen element size. Once collected, the mean value of the maximum, minimum and mean dye coverage of all slices of a given simulation was taken. Finally, the confidence intervals were calculated over the mean of the maximum, minimum and mean dye coverage, resulting in 3 values of confidence and their respective ranges for each of the 20 sequential simulations.

The dye coverage reported in Lipsius & Mooney (2006) suggested that between 8 and 40 % of the domain was dyed. This is accounting for both 25 mm and 50 mm applied head, as well as both spring and summer results. Both the 50 mm and spring results showed a much larger coverage, leading to the wide range of dye coverage. For the case of 25 mm in the summer period, as seen in Figure 7.10 (a-c), these percentages are much lower.

Table 7.3 shows the mean, and upper and lower bounds for the maximum, minimum and mean dye coverage for both the horizontal and vertical projections calculated using data from all 20 simulations. It can be seen that the range of the values vary, but are small enough to show model consistency, suggesting that the response of the model is consistent whilst allowing for highly varied infiltration patterns. The percentage values given for the maximum dye coverage are typically larger than the experimental equivalent, but as suggested previously, this can be attributed to the numerical application of flux. Similarly the percentage values match well with those given in the histograms of Figure 7.10 (a-c). The confidence in the confidence

intervals of the observed quantities is ≥ 99% for the horizontal projection, and ≥ 99% for the vertical projection.

Table 7.3: Calculated ranges of dye coverage based on all 20 simulations for the maximum, minimum and mean dye coverage in both horizontal and vertical projections

Projection	Dye Coverage	Lower Bound (%)	Mean (%)	Upper Bound (%)
Horizontal	*Minimum*	2.34	2.94	3.98
	Mean	12.26	13.03	13.89
	Maximum	81.85	85.11	88.73
Vertical	*Minimum*	3.46	4.23	5.01
	Mean	12.26	13.03	13.89
	Maximum	20.10	21.58	22.79

The convergence of the confidence in the calculated intervals can be seen in Figure 7.13 (a) and (b). As the number of simulations increases, the confidence in the calculated interval converges to above 95%, as seen in Figure 7.13 (a). Similarly, as in Chapter 6, the evolution of the confidence intervals for a given level of confidence was also calculated. This is shown in Figure 7.13 (b), where the convergence of the confidence intervals for an assumed confidence of 95% is observed. Figure 7.13 (a) and (b) relate to the horizontal dye coverage statistics, but the same observations and conclusions are seen for the vertical projection also, as in Figure 7.14 (a) and (b). As is expected, there is more uncertainty in the vertical dye coverages due to the larger variations in the vertical histograms in Figure 7.10 and the additional plots in Appendix B.

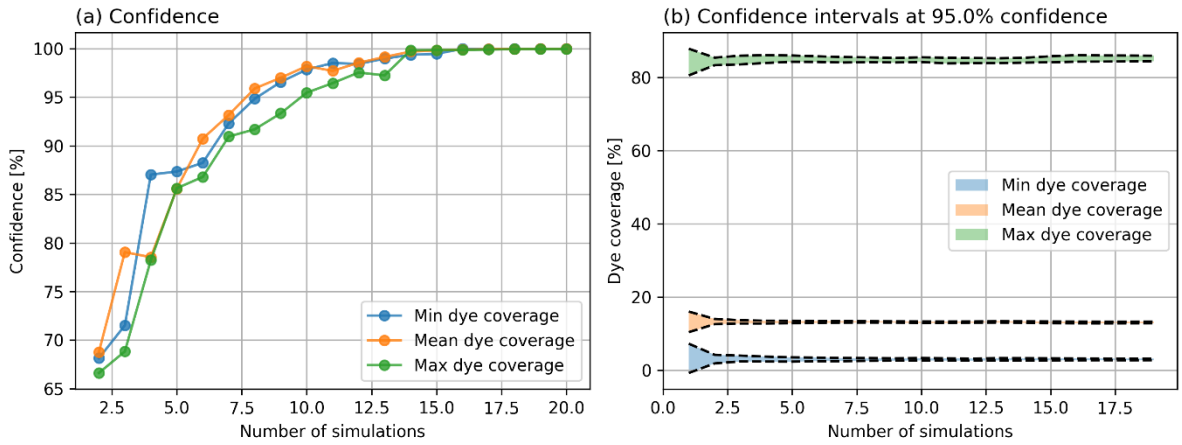

Figure 7.13: (a) Confidence in the calculated intervals of the investigated parameters of dye coverage in the horizontal projection, and (b) the convergence of confidence intervals for dye characteristics at 95% confidence

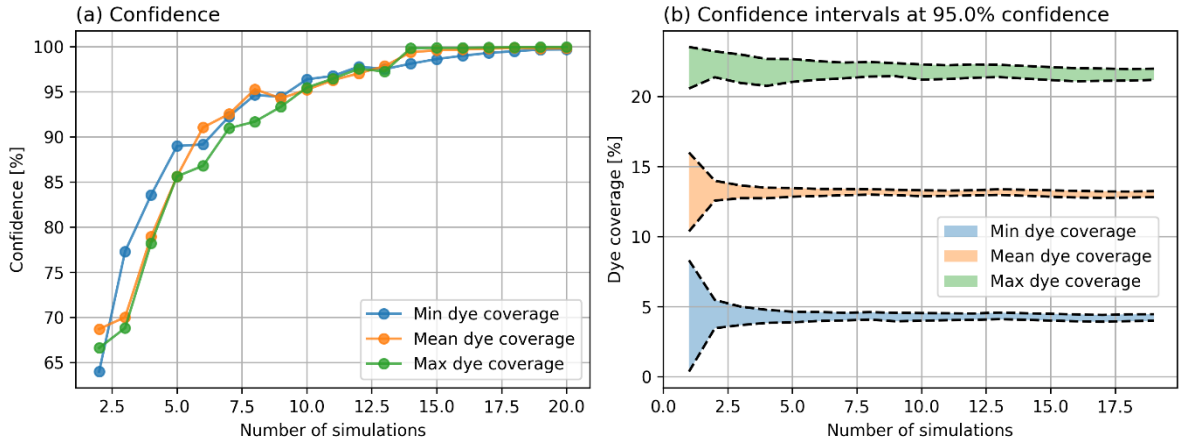

Figure 7.14: (a) Confidence in the calculated intervals of the investigated parameters of dye coverage in the vertical projection, and (b) the convergence of confidence intervals for dye characteristics at 95% confidence

7.3.3 Effects of field anisotropy

In the previous sections of this chapter, the fields were assumed to have larger correlation lengths in the vertical direction, as seen in Figure 7.6 (a). To highlight the relative effects of this scaling, the 20th simulation was carried out again for an isotropic field, and another anisotropic field where l was assumed to be 0.4 m in the horizontal direction. In all cases, l in the vertical direction was kept consistent as 0.2 m. To illustrate this, the fields of K_s are given in Figure 7.17 (a-c), where it is clear how the correlation structure changes based on the scaling. The resulting tracer

activation plots are given in (d-f). It can be seen that this level of variation in anisotropy is not high enough to cause large differences in the flow paths, and resulting tracer activation regions. The behaviour is much the same regardless of this level of anisotropy, and can be attributed to the fields representing localised variations in material parameters.

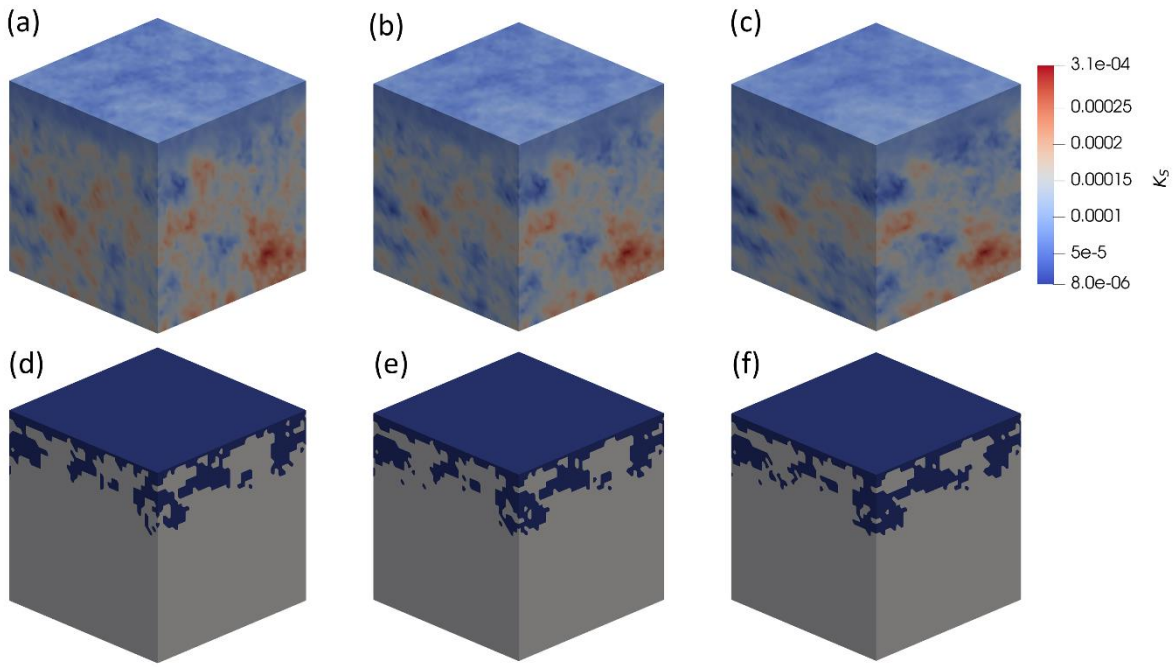

Figure 7.17: The effects of field anisotropy of material properties on tracer distribution patterns, where the horizontal and vertical correlation lengths are: 0.1 and 0.2 m (a)(d), 0.2 and 0.2 m (b)(e), and 0.4 and 0.2 m (c)(f) respectively. Shown are the random fields (a-c) and resulting tracer profiles (d-f)

7.4 Conclusions

This chapter has presented a detailed look into model development for the representation of hydrophobic soils, as well as the fingered flow they induce. The considerations presented in Section 7.3 are the key components that allow the model to account for water repellency and layered soils. One such component was the adoption of an alternative SWRC which allowed for the soil to have water entry pressures that are characteristic of water repellent soil. In this way, the pore water pressure can build up on the surface where the boundary condition is applied, mimicking the resistance to infiltration that WR soils exhibit. The variability of the WEP also has influence over the flow in the soil body. Once the fluid phase has

entered the media, the variation in WEP leads to highly unstable fingered flow in the water repellent and transition regions, becoming more diffuse when reaching the wettable layers.

The flow patterns observed in the non-wettable layers are synonymous with the hydraulic behaviour of water repellent soils, highlighting the model's ability to represent complex flow phenomena under the given material type. The dye coverage of the soil profiles, as in the experiments, was used to quantify the model response, and is seen to match well with the experimental observations. The calculation of strong confidence values suggests the presented results are representative of overall model behaviour. Similarly, the image analysis conducted on the numerical slices indicate that the model behaviour is representative of the experimental behaviour.

Consideration was also given to the transition region between soil layers. By assuming a variation of mixture between the interfacing layers with depth, the naturally non-unform transition between soil layers is represented. In addition, the SWRC follows the same variation with depth, and can account for the combination of the two material SWRCs for the given representative elementary volume of soil. The combination of both wettability types for a given element, as well as the resulting SWRC, allows the model to predict highly unstable fingered behaviour.

Finally, as in the previous chapter, the necessity of conducting the analyses in 3-D is also shown. Strong lateral fluxes are observed in the region of hydrophobicity, both within the fully WR layer and transition zone, suggesting that a 1- or 2-D analysis would not capture the full effects, leading to much more conservative hydraulic behaviour. The computations also reiterate the non-unform wetting front movement due to strong localise fluxes.

7.5 References

Ahmadi, H., Namin, M.M. and Kilanehei, F. 2016. Development a numerical model of flow and contaminant transport in layered soils. Advances in environmental research 5(4), pp. 263–282. doi: 10.12989/aer.2016.5.4.263.

Foroughi, S., Bijeljic, B. and Blunt, M.J. 2022. A Closed-Form Equation for Capillary Pressure in Porous Media for All Wettabilities. Transport in Porous Media. doi: 10.1007/s11242-022-01868-3.

van Genuchten, M.Th. 1980. A Closed-form Equation for Predicting the Hydraulic Conductivity of Unsaturated Soils. Soil Science Society of America Journal 44(5), pp. 892–898. doi: 10.2136/sssaj1980.03615995004400050002x.

Heilig, A., Steenhuis, T.S., Walter, M.T. and Herbert, S.J. 2003. Funneled flow mechanisms in layered soil: field investigations. Journal of Hydrology 279(1–4), pp. 210–223. doi: 10.1016/S0022-1694(03)00179-3.

Hopp, L., Peiffer, S. and Durner, W. 2006. Spatial variability of arsenic and chromium in the soil water at a former wood preserving site. Journal of Contaminant Hydrology 85(3–4), pp. 159–178. doi: 10.1016/j.jconhyd.2006.01.005.

Leverett, M.C. 1941. Capillary Behavior in Porous Solids. Transactions of the AIME 142(01), pp. 152–169. doi: 10.2118/941152-G.

Lipsius, K. and Mooney, S.J. 2006. Using image analysis of tracer staining to examine the infiltration patterns in a water repellent contaminated sandy soil. Geoderma 136(3–4), pp. 865–875. doi: 10.1016/j.geoderma.2006.06.005.

Liu, C.-Y., Ku, C.-Y., Huang, C.-C., Lin, D.-G. and Yeih, W.-C. 2015. Numerical Solutions for Groundwater Flow in Unsaturated Layered Soil with Extreme Physical Property Contrasts. International Journal of Nonlinear Sciences and Numerical Simulation 16(7–8), pp. 325–335. doi: 10.1515/ijnsns-2015-0060.

Nieber, J., Sheshukov, A., Egorov, A. and Dautov, R. 2003. Non-equilibrium model for gravity-driven fingering in water repellent soils: Formulation and 2D simulations. In: Soil Water Repellency. Elsevier, pp. 245–257. Available at: https://linkinghub.elsevier.com/retrieve/pii/B9780444512697500254.

Nieber, J.L. 1996. Modeling finger development and persistence in initially dry porous media. Geoderma 70(2–4), pp. 207–229. Available at: https://linkinghub.elsevier.com/retrieve/pii/0016706195000860.

Ricketts, E.J., Freeman, B.L., Cleall, P.J., Jefferson, A. and Kerfriden, P. 2023. A Statistical Finite Element Method Integrating a Plurigaussian Random Field Generator for Multi-scale Modelling of Solute Transport in Concrete. Transport in Porous Media. doi: 10.1007/s11242-023-01930-8.

Ritsema, C.J., Dekker, L.W., Nieber, J.L. and Steenhuis, T.S. 1998. Modeling and field evidence of finger formation and finger recurrence in a water repellent sandy soil. Water Resources Research 34(4), pp. 555–567. doi: 10.1029/97WR02407.

Romano, N., Brunone, B. and Santini, A. 1998. Numerical analysis of one-dimensional unsaturated flow in layered soils. Advances in Water Resources 21(4), pp. 315–324. doi: 10.1016/S0309-1708(96)00059-0.

Wang, J.P., Zhuang, P.Z., Luan, J.Y., Liu, T.H., Tan, Y.R. and Zhang, J. 2019. Estimation of unsaturated hydraulic conductivity of granular soils from particle size parameters. Water (Switzerland) 11(9). doi: 10.3390/w11091826.

Wang, Z., Wu, L., Harter, T., Lu, J. and Jury, W.A. 2003. A field study of unstable preferential flow during soil water redistribution. Water Resources Research 39(4). Available at: http://doi.wiley.com/10.1029/2001WR000903.

Woods, S.W., Birkas, A. and Ahl, R. 2007. Spatial variability of soil hydrophobicity after wildfires in Montana and Colorado. Geomorphology 86(3–4), pp. 465–479. doi: 10.1016/j.geomorph.2006.09.015.

Zheng, S., Xing, X., Lourenço, S.D.N. and Cleall, P.J. 2021. Cover systems with synthetic water-repellent soils. Vadose Zone Journal 20(1). Available at: https://onlinelibrary.wiley.com/doi/10.1002/vzj2.20093.

Chapter 8

Conclusions and further work

8.1 Introduction

This chapter provides a summary of the work presented in this thesis, gives the principal conclusions from the research, and provides suggestions for further work.

In Chapter 2, a review of topics relating to the modelling of heterogeneous unsaturated soil for both hydrophilic and hydrophobic soils was presented. The following areas were addressed; the modelling of transport processes in saturated and unsaturated soil; the effects of heterogeneity on soil hydraulic behaviour; soil modelling through stochastic methods; an introduction to random field generation methods; an overview of soil hydrophobicity; the modelling of water repellent soils.

Chapters 3 and 4 presents the theoretical and numerical formulations for the process of moisture transfer and random field generation. These techniques are used in the work described in the subsequent three chapters, and their main conclusions are given in Section 8.2

Section 8.3 reviews and presents the main conclusions from Chapter 5, which considered the reduction of error in the near-boundary when generating correlated random fields through the SPDE approach; Section 8.4 reviews and draws conclusions on the contents of Chapter 6 in which unstable preferential flow was modelled; Section 8.5 reviews and concludes on Chapter 7 where the complex flow observed in water repellent soil was considered.

Finally, Section 8.6 presents the overall conclusions, and suggestions for further research are made in Section 8.7.

8.2 Theoretical and numerical formulation

In Chapters 3 and 4, the theoretical and numerical formulations were derived for moisture transfer in unsaturated soils and Gaussian random field generation based on the solutions of SPDEs. Chapter 3 focused on the theoretical components, where the governing equations were derived based on mass balance and Darcian flow over representative elementary volumes of soil. This approach is well-established for

coupled models and has been effective for representing hydraulic flow processes in homogeneous soils. However, it does not inherently account for the impacts of heterogeneity.

Similarly, the random field generation method presented indicates its adequacy as a tractable and computationally efficient approach for producing correlated random fields. The problem formulation is also based on a PDE, as in the case for the theoretical formulation, meaning that their solutions can be approached in similar ways. This is in fact the case, where finite elements (FE) are used to solve the given PDEs numerically. As well as seeing vast amount of development over the past few decades, the use of FE means that further model development is not impeded. It is known that certain physical processes are better represented by different numerical methods, but by using FE, a wide range of dynamic processes may be considered with the present approach. Similarly, more advanced FE approaches can be used to expand the model for different scenarios, such as unfitted methods. It also allows for well documented optimisation techniques to be implemented, such as adaptive meshing and time-stepping, or simple parallelisation in matrix assembly.

Another significant benefit comes from similarities in the model architecture in terms of solving both the moisture transfer and random field generation problems. In both cases, the matrices are very similar, so routines for matrix assembly -as well as solving the matrix equations- can be used interchangeably, allowing the problems to be solved over the same domain topology.

8.3 Error reduction in SPDE based random field generation

In Chapter 5, a new approach to mitigate error in the near-boundary region of random fields generated through SPDEs was presented. The method considered a reframing of the standard Robin boundary condition as a weighting between its Dirichlet and Neumann components, denoted the weighted D-N approach. In this way, the weighting between them could be tuned to alter the correlation structure near the boundary with the aim of reducing error.

Systematic assessment of the optimal weighting parameter α through autocorrelation function evaluation showed that this approach has a better overall match than all other applied boundary conditions, also matching well on more complex geometries.

The functions for α based on the parametric study enables its optimal value to be determined for other domains and desired length-scales.

As such, the weighted D-N approach is recommended as being the applied boundary condition when formulating the stochastic PDEs to be solved. Whilst both proposed choices of the Robin coefficient λ perform equally well, $\lambda = \lambda_2$ is a more practical choice. When $\lambda = \lambda_2$, the resulting covariance functions show that changing the weighting parameter α leads to more uniform variation in resulting covariance structure, providing a more linear relationship than if $\lambda = \lambda_1$. This suggests that choosing an α with small variations from its fitted value will have less of an impact on the final correlation structure than if $\lambda = \lambda_1$, making it more consistent when applying the condition outside of the tested range or on less regular domains. The other main advantage, as opposed to the Neumann boundary condition with extension, is the lack of dependence on an extended domain. In this case, the computational domain was chosen as a cube with relatively low numbers of elements, so computational expense did not need to be considered when solving over an extended domain. If the field generation method was conducted over a finer mesh, as in the subsequent chapters, then this dependence could cause complications. Finally, the weighted D-N approach was shown to be significantly more accurate for larger values of l as opposed to the Robin condition with $\lambda = 1.42l$, thus providing better control over the resulting correlation structure where the formulation begins to break down.

The relationships presented are given in relative terms, so are applicable to a wider range of domains and engineering problems. The proposed boundary condition is aimed at giving a more sufficient approximation of the correlation structure of said parameters, allowing for a more robust quantification of uncertainty through numerical analyses.

8.4 Simulation of unstable flow in unsaturated soils

Chapter 6 described the use of Gaussian random fields in representing material heterogeneity to model non-uniform flow in unsaturated soil. Similarly, a new way to apply boundary conditions in a heterogeneous manner was presented, this being based on the material's inherent spatial variability at its surface. The model was then validated by simulating field-based tracer experiments to replicate the vertical infiltration profiles observed. Finally, the presented results were quantified in terms of

the finger characteristic uncertainty to show that the presented results were representative.

The Gaussian random field approach provides an effective means of representing a field of material properties for a body of soil. Conventional methods for computing correlated fields that rely on the formation and inversion of covariance matrices are computationally expensive and unsuitable for large 3-D simulations. The alternative method proposed, which requires the solution of a system of discretised partial differential equations derived from a Whittle-Matérn prior, is far more computationally efficient. This method has the added advantage that the resulting system of finite element equations has essentially the same structure as those used to solve the transport problem. A proper simulation of the soil transport processes also requires spatial variations of boundary infiltration properties to be considered. The new method proposed of using overlapping kernel functions covering the infiltration boundary provides an effective means of simulating non-uniform inflow into a domain whilst maintaining mass balance at all times.

Incorporating the new field generation algorithm into a 3-D FE model for moisture transport allows non-uniform flow behaviour within soil bodies to be simulated in a realistic manner. A set of validation analyses that considered moisture infiltration into a layer of sandy loam showed that the new proposed model is able to represent the characteristics of non-uniform moisture flow into and through a heterogeneous body of soil with good accuracy. The method achieves relatively high confidence levels for characteristic stochastic variables with relatively few simulations (e.g. a 99.7% CI with 12 realisations). The proposed technique, given its computational ease, is suitable for larger field-scale problems, where the statistical significance can be determined using a relatively low number of simulations.

8.5 Simulation of unstable flow in hydrophobic unsaturated soil

Chapter 7 presented the extension of the model such that it is able to simulate layered soils of mixed wettabilities. The constitutive components of the model were modified to account for increasing levels of water repellency in low wettability layers as current relations struggle to represent appropriate water entry pressures. Similarly, the transition region between layers was considered, with the proposed method accounting for an averaged level of mixture of the material with depth. The

model was then applied in representing field tracer experiments to match with the observed vertical profiles. Finally, the uncertainty in the results was quantified based on the dye coverage of the numerical domain, and the effects on tracer activation regions due to variations in field anisotropy were given.

Once more, the inclusion of correlated random fields was proven to be sufficient in introducing material heterogeneity, leading to highly unstable flow. By using the alternative saturation-capillary pressure relation and spatially varying its parameters, the local variations lead to fingered vertical profiles which matched well with the experimental observations. Similarly, the proposed method to account for the transition between material layers allowed for a more realistic response in the wetting front when passing through said region. By assuming an averaged mixing of the adjacent layers in terms of their level of wettability with depth, this depicted a more realistic representation of the domain in this area. Its implementation is highly flexible, and allows for arbitrarily sized transition zones whose smoothness can also be defined.

As before, the use of confidence interval calculations was seen to be suitable in determining convergence criteria for multi-simulation regimes. This allows one to run a very low number of simulations, whilst also ensuring that the results that have been obtained are representative of the population response of the model. With only 13 simulations, the population ranges of the maximum, minimum and mean dye coverages were calculated to 95% confidence. This number of simulations is orders of magnitude less than what would be required in a traditional Monte Carlo approach. Quantifying model responses in this way gives a good descriptor of the typical behaviour a model can portray, but is dependent on the indicators used for its quantification.

8.6 Overall conclusions

An overarching theme from conducting an extensive literature review is that many studies adopt a 2-D idealisation of flow problems in soil. As is shown in both Chapters 6 and 7 for the case of fingered flow problems, the nature of the resulting flow is fully 3-D, meaning that to represent the problem fully, a 3-D analysis is required. Whilst fingered flow is an exaggerated case of a general flow problem, the

conclusion on the necessary dimensions of the simulation remain valid as this distinct behaviour amplifies the difference between 2-D and 3-D representations.

Similarly, material heterogeneity is a strong cause of non-linear responses, which is especially true in soil hydraulic responses. Many modelling approaches assume a homogeneous domain, but this is not the case in physical systems, especially in porous or particulate media. In the presented model, the heterogeneity of the material is the driving factor in the non-uniform wetting response, as is the case in real life, highlighting its importance in numerical analyses. Heterogeneity of boundary conditions should also be accounted for. Their application allowed for the local variations in material properties at the surface to dictate the influx of water into the domain based on the conductivity. Whilst this is largely a short-term response, the flow paths that are generated based on the local variations supply water into the media in a much more non-uniform manner, and lead to more discrete fingered behaviour.

The inclusion of Gaussian random fields generated through the SPDE approach allows highly flexible integration with FE based codes, and is more than suitable for representing spatially varying material properties. Based on the numerical approach of FE, the solution of the SPDE and moisture transfer matrix equation are carried out in a similar fashion, reducing algorithmic complexity. Even if FE was not employed, the solution of the SPDE is agnostic to the choice of solution method, making it a suitable method of random field generation for many different numerical approaches. Algorithmic flexibility, nodal based solutions, as well as its highly sparse matrix representation makes it an attractive option in introduction random fields to existing code bases.

Similarly, the reassurance that the correlation structure in the near-boundary region will be representative of the assumed covariance function due to the proposed boundary conditions in Chapter 5 is advantageous. The problem formulation relies on bounding a problem defined over three dimensional real space to a discrete domain, introducing errors in the near-boundary. This is common in a number of numerical approaches for many different problems as the domain must be defined. The boundary conditions proposed in Chapter 5 present an attractive alternative based on rigorous testing, such that the correlation structure in the near-boundary

region can be well defined, whilst also taking advantage of the efficient generation method for the correlated fields.

When considering the objectives of the present study laid out in Chapter 1, it can be seen that all four objectives have been achieved. They largely focused around the development of a stochastic model that can represent fingered flow for soils of wettability. The ability of the model to represent this type of unstable flow has been demonstrated in Chapters 6 and 7, fulfilling the first and third objectives. Similarly, through the development of a novel approach to deal with the associated error of random field generation in the SPDE approach, the second objective has also been met. This revolved around finding a tractable way to use random fields to represent material heterogeneity whilst maintaining a consistent correlation structure across the numerical domain. Lastly, the final objective was to validate the model against experimental results. Coupling heterogeneous flux application with the material variability allows physical flow processes to be represented with a high level of fidelity, and for both the unsaturated hydrophilic and hydrophobic cases, the model response was shown to produce infiltration patterns that are representative of complex field observations.

8.7 Suggestions for further work

An attractive extension of the model would be the use of a constitutive relation for the saturation-capillary pressure that could account for the level of mixing directly in the transition region. This would remove the need to interpolate between relationships, and would allow for a more flexible representation depending on the closed form. Generally, this would require a multimodal SWRC, and numerical testing could be conducted using the model to perform standard testing for the determination of SWRCs. Similarly, the transition zone convention could be easily extended with Gaussian processes (GPs). The interface between the two layers, be it a change in material or wettability, could be represented by a GP such that the interface becomes non-uniform as it would be physically. From this, the transition region would still vary with depth as you go from one layer to the other in the vertical direction, but laterally, the level of mixing would vary spatially. Overall, this would give a more realistic representation of the interfaces between soils layers as to assume they are perfectly horizontal with no variation is an oversimplification.

Another extension would be the addition of a coupled chemical phase that can explicitly represent the applied tracer. For many infiltration experiments, it is necessary to apply a tracer, so having an explicit representation of its movement with the moisture phase through advection-diffusion processes would give more representative profiles. This could be done simply through coupling with the non-uniform moisture phase, but the presence of random fields means it would be desirable to add spatial variability to the underlying advection-diffusion process.

Further extension would be the parallelisation of the code base. Currently it runs in a serial fashion, but extension to multi-core or multi-processor execution would give a significant decrease in computational time. In the first instance, the matrix assembly routines should be re-written to account for this. Following this, current high performance computing solutions should be explored, such as domain decomposition techniques or distributed-memory solvers.

It is clear from the literature that hysteresis in the hydraulic behaviour of soils should be considered more widely. It is often difficult when modelling to know when the response changes from drying to wetting, and vice versa, which in turn makes it difficult to know whether to use the drying or wetting curve of the associated medium. They are often quite different in terms of their characteristics, so knowing which to use at a given point in a simulation is important choice. Similarly as important is the hysteretic response of water repellent media. More work needs to be done to understand these effects and how they can be represented numerically.

The presented work has considered solely numerical development, but experimental investigation into the variability of soil material properties is just as important. It is accepted that soil material parameters follow a Gaussian distribution across the domain, but this could warrant further investigation for different material parameters. Similarly, the distribution of naturally induced water repellency -depending on the method of induction- should be investigated. The process over which hydrophobicity is induced could impact the spatial variability of wettability present in the soil. For example, chemicals invading the soil will do so non-uniformly, so at different points the depth of water repellency will vary. This is also true for wildfire affected soil, as the superheating of the soil will reduce with depth, leading to non-homogenous

wettability. Based on the experimental investigations, the model can be further developed to reflect the findings, making it more representative of the wider problem.

In a similar fashion, the representation of material heterogeneity through random fields is applicable to any materials where heterogeneity is present. The presented work is merely applied to soil mechanics problems as a way to illustrate the effects of material heterogeneity on flow related processes, and is equally applicable to other materials. For example, cementitious materials exhibit spatial variability in their mechanical properties, which could be represented by random fields to see their effects on mechanical or flow related processes. Similarly, geometric variability could be easily expressed in terms of random fields. Whilst this has not been touched upon in the current study, random fields could be used to represent local variation in material geometries, such as rough surfaces. The effects of roughness on flow could then be quantified.

Finally, the model could be readily extended to related research domains in soil mechanics, such as wildfire and slope stability. As seen in the literature, slope stability problems benefit from the consideration of material heterogeneity. Coupling the moisture transfer and mechanical response would allow for these processes to be represented. A nice extension would be a FE and material point method coupled model, such that the large deformation behaviour, which the finite element method struggles to deal with, can be modelled accurately. Similarly, extending the model to couple heat and moisture transport with the ability to account for severe water repellency makes it well suited to deal with the material response observed during and post fire. Mechanisms for hysteretic water repellency would need to be developed, as well as complex boundary conditions to account for runoff and erosion. With the increase in severe wildfire events due to an ever-changing climate, it is becoming ever more important to represent its associated complex phenomena.

Appendix A

Additional tracer plots

The following contains additional tracer plots to supplement those shown in Chapter 6.

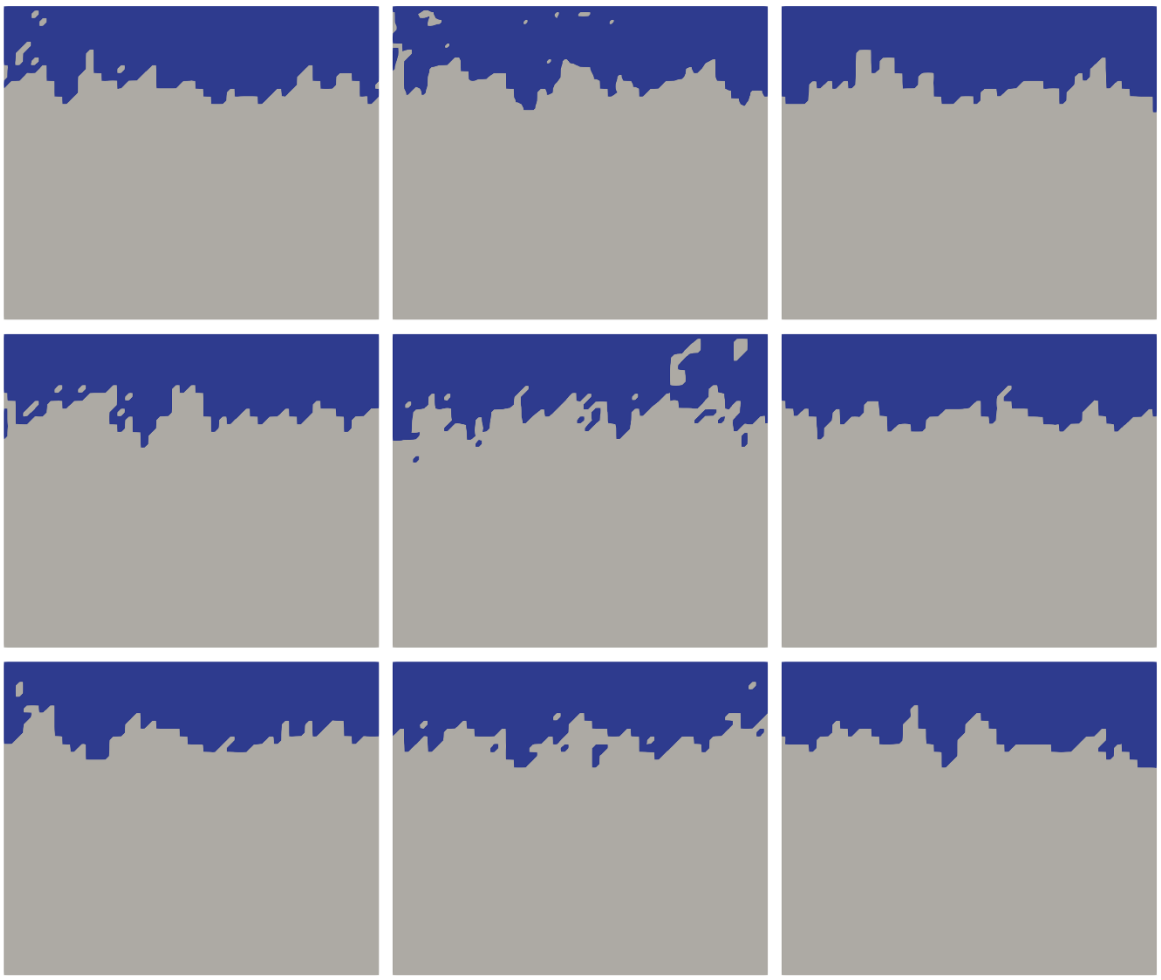

Figure A1: Slices of the domain to highlight the tracer activation region at 85% degree of saturation

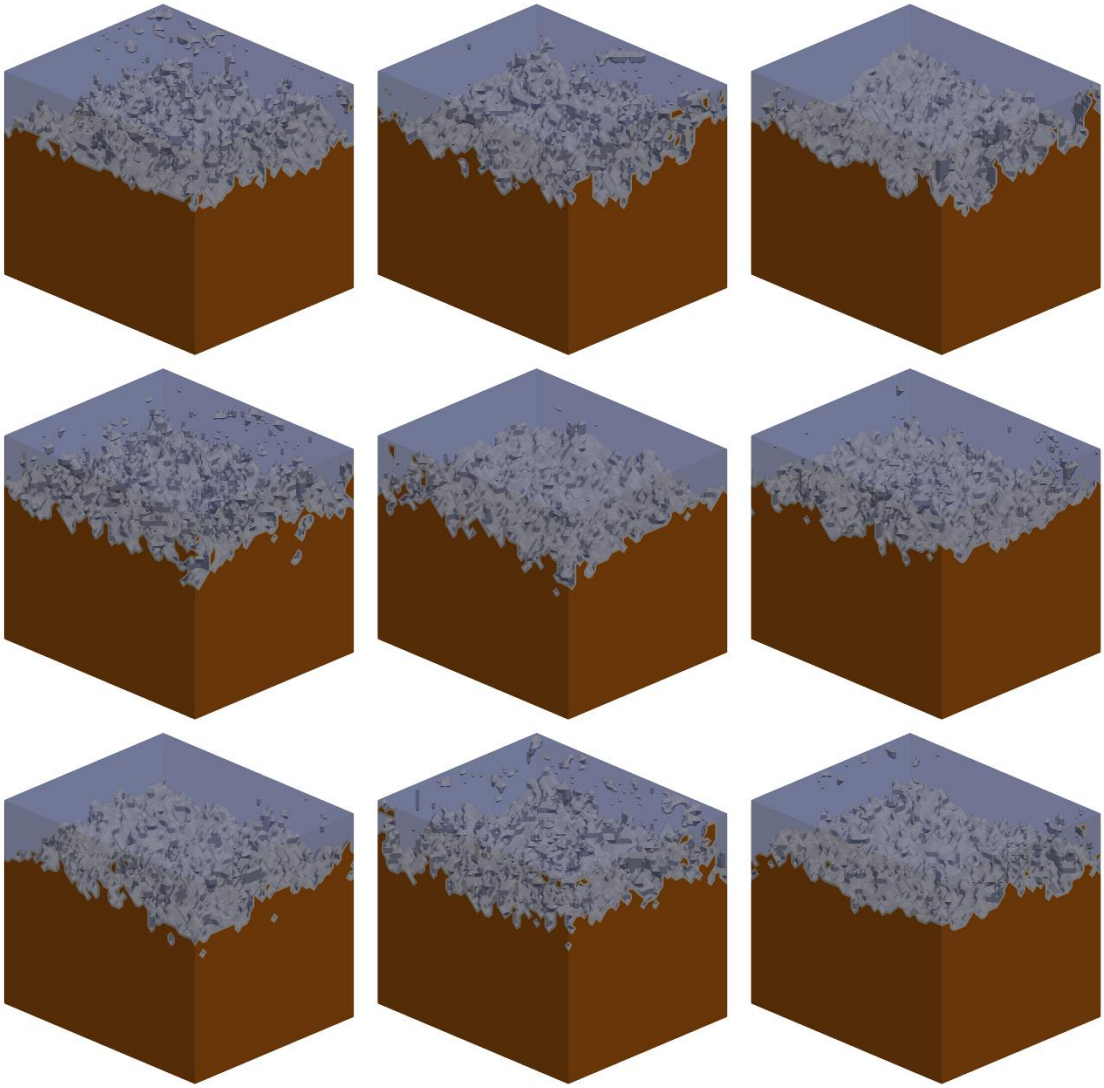

Figure A2: Tracer activation regions at 85% degree of saturation

Appendix B

Additional hydrophobic simulation results

The following contains additional results from the analyses conducted in Chapter 7. For the full range of 800 slices, see: https://github.com/EJRicketts/Thesis-HydrophobicSlices

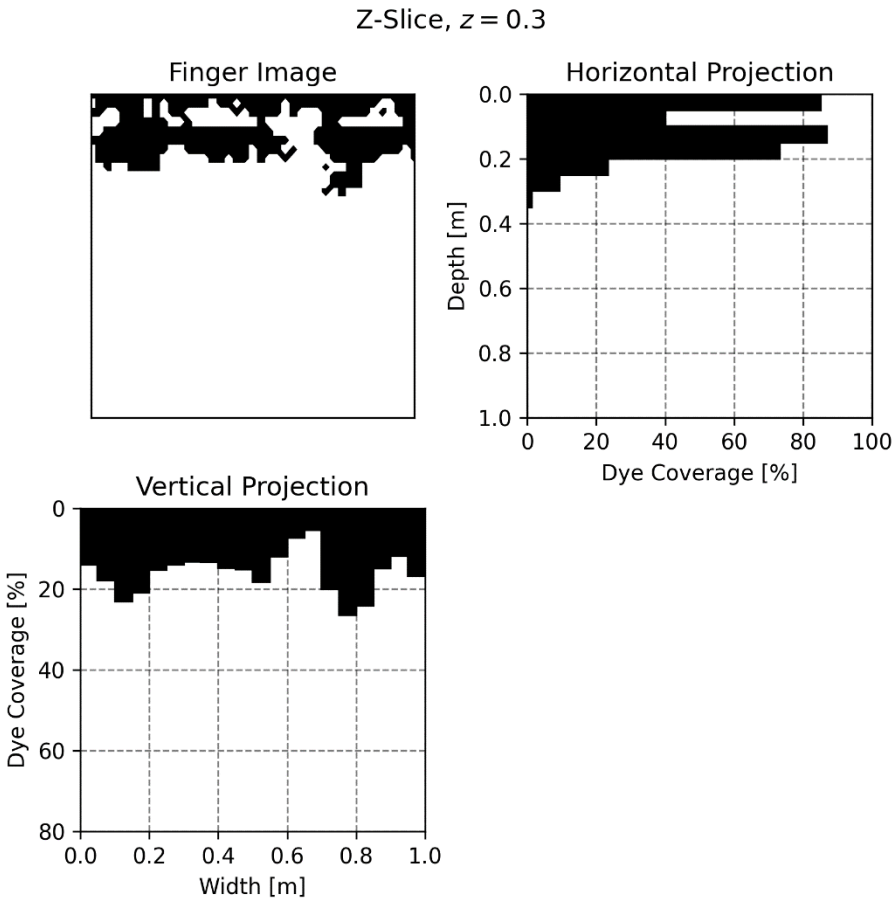

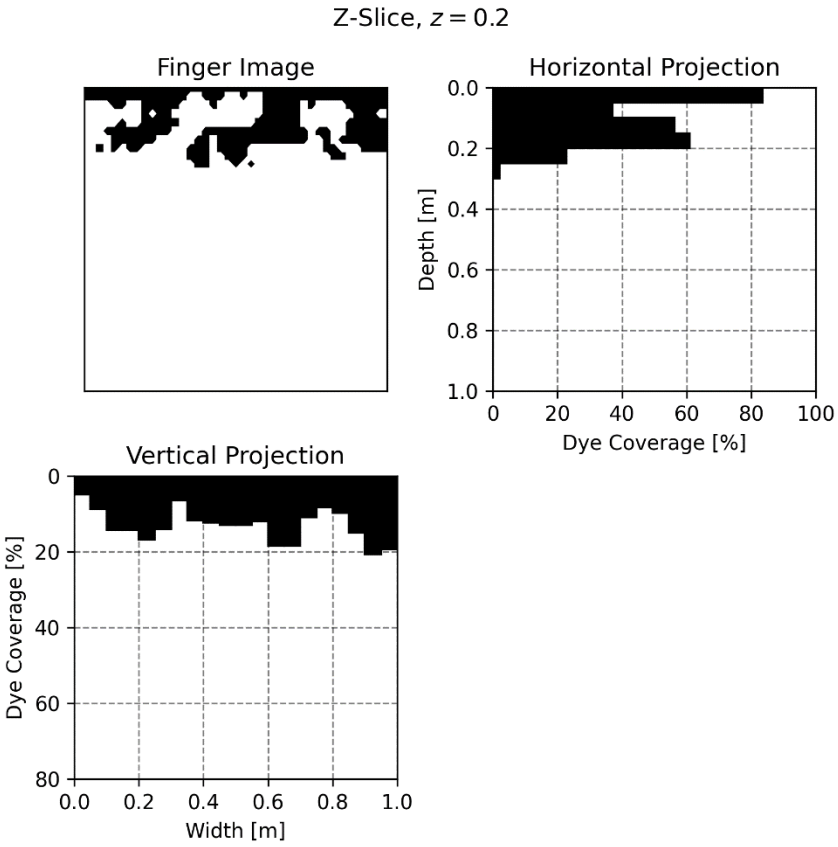
Z-Slice, $z = 0.2$
Finger Image
Horizontal Projection
Depth [m]
0.0
0.2
0.4
0.6
0.8
1.0
0
20
40
60
80
100
Dye Coverage [%]
Vertical Projection
Dye Coverage [%]
0
20
40
60
80
0.0
0.2
0.4
0.6
0.8
1.0
Width [m]

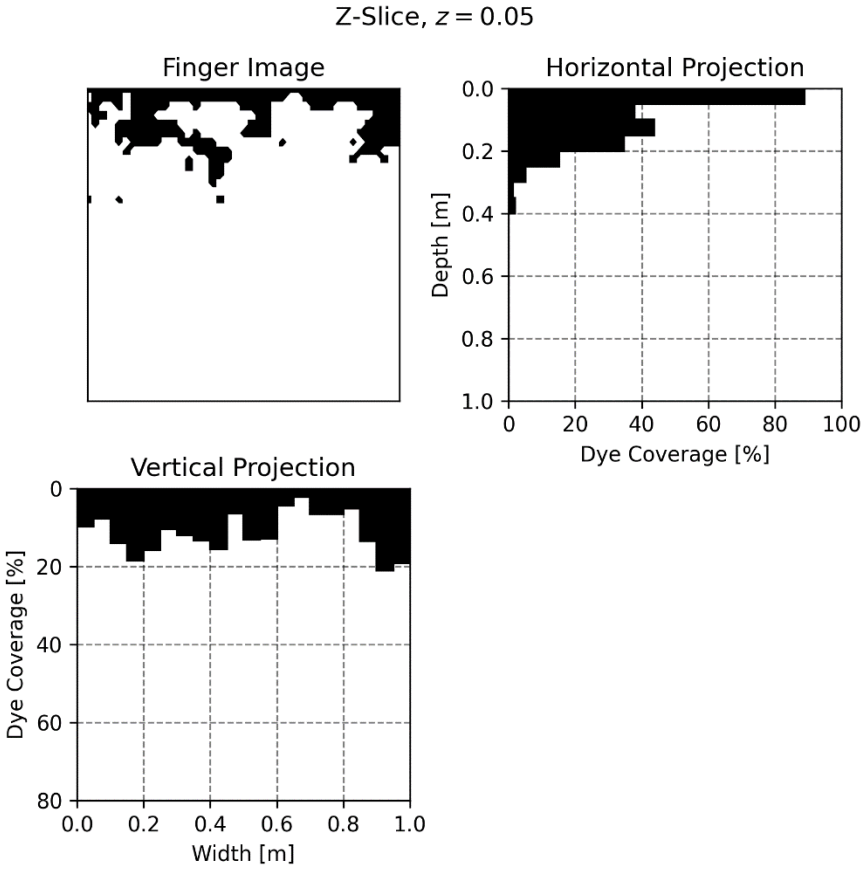
Z-Slice, $z = 0.05$
Finger Image
Horizontal Projection
Depth [m]
0.0
0.2
0.4
0.6
0.8
1.0
0
20
40
60
80
100
Dye Coverage [%]
Vertical Projection
Dye Coverage [%]
0
20
40
60
80
0.0
0.2
0.4
0.6
0.8
1.0
Width [m]

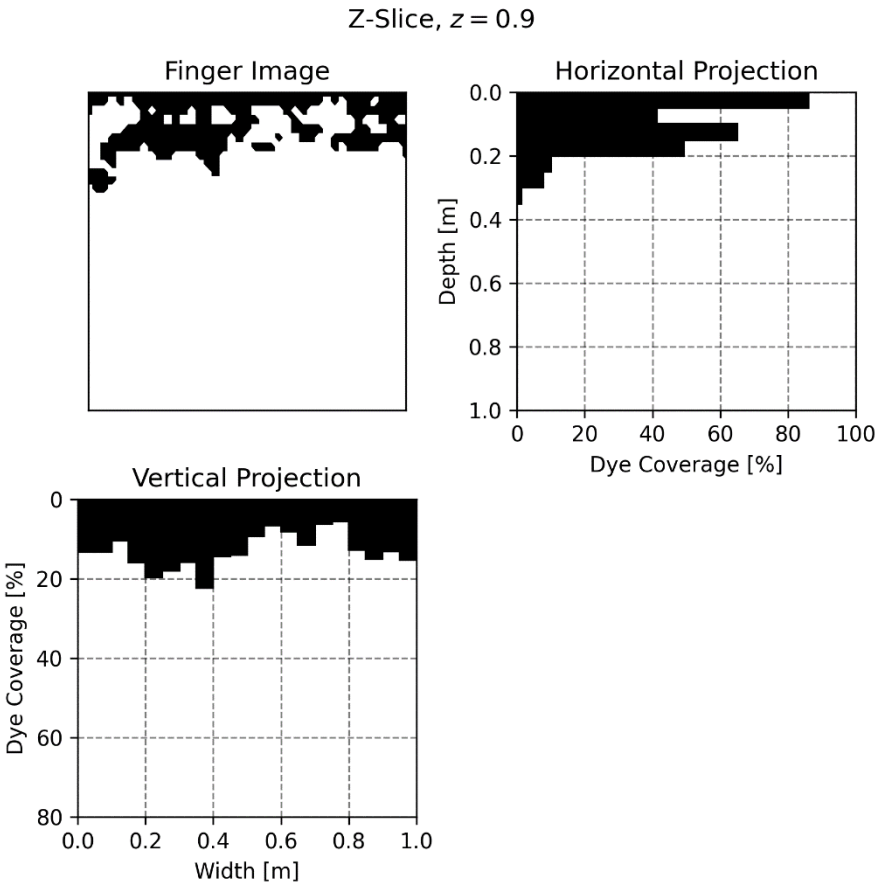
Z-Slice, $z = 0.9$
Finger Image
Horizontal Projection
Depth [m]
Dye Coverage [%]
Vertical Projection
Dye Coverage [%]
Width [m]

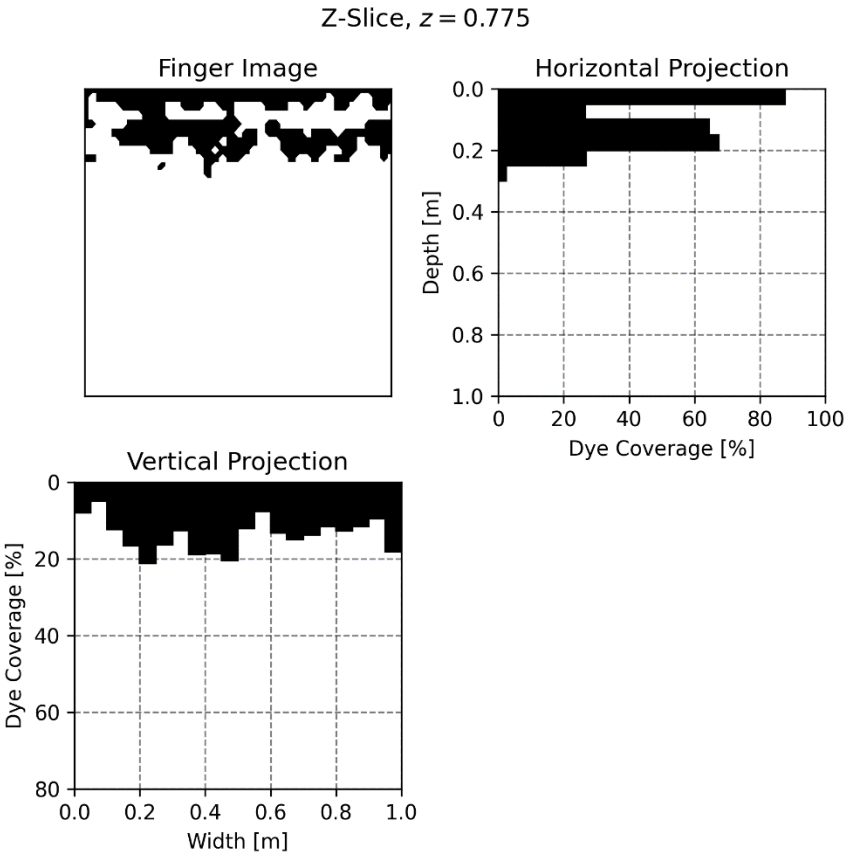
Z-Slice, $z = 0.775$
Finger Image
Horizontal Projection
Depth [m]
Dye Coverage [%]
Vertical Projection
Dye Coverage [%]
Width [m]

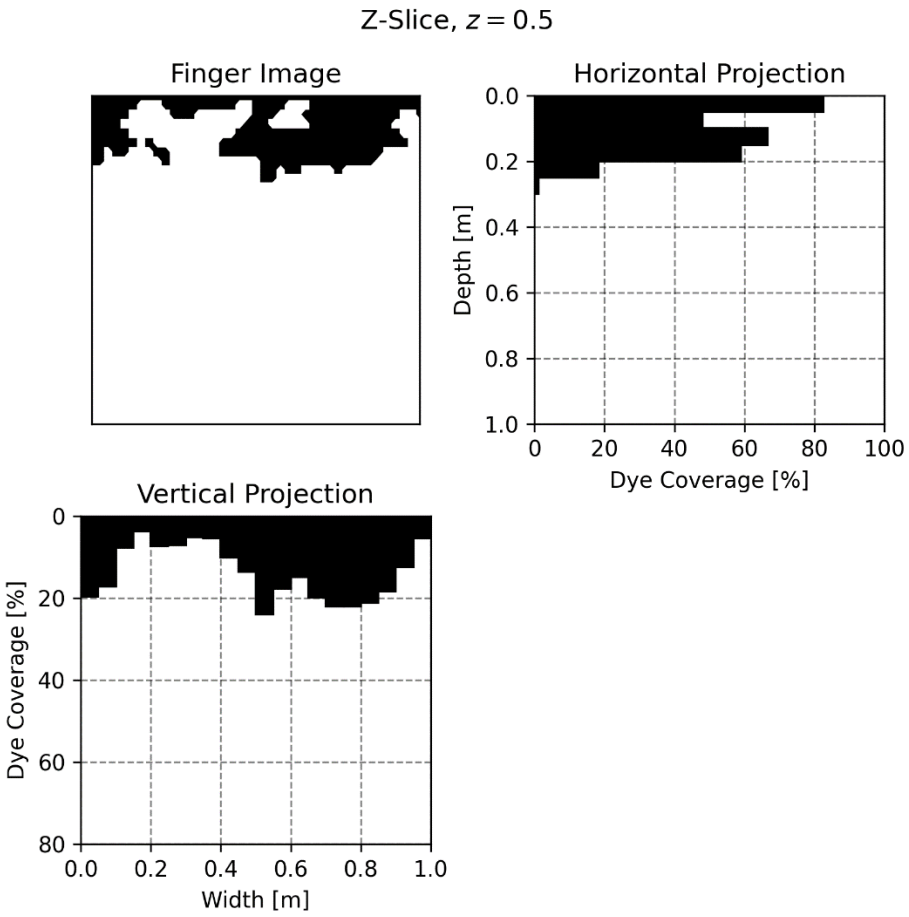

Figure B1: Slices of the domain and their respective dye coverages to highlight the tracer activation region at 35% degree of saturation